



저작자표시-비영리-변경금지 2.0 대한민국

이용자는 아래의 조건을 따르는 경우에 한하여 자유롭게

- 이 저작물을 복제, 배포, 전송, 전시, 공연 및 방송할 수 있습니다.

다음과 같은 조건을 따라야 합니다:



저작자표시. 귀하는 원저작자를 표시하여야 합니다.



비영리. 귀하는 이 저작물을 영리 목적으로 이용할 수 없습니다.



변경금지. 귀하는 이 저작물을 개작, 변형 또는 가공할 수 없습니다.

- 귀하는, 이 저작물의 재이용이나 배포의 경우, 이 저작물에 적용된 이용허락조건을 명확하게 나타내어야 합니다.
- 저작권자로부터 별도의 허가를 받으면 이러한 조건들은 적용되지 않습니다.

저작권법에 따른 이용자의 권리는 위의 내용에 의하여 영향을 받지 않습니다.

이것은 [이용허락규약\(Legal Code\)](#)을 이해하기 쉽게 요약한 것입니다.

[Disclaimer](#)

공학박사학위논문

**Simultaneous CubeSat attitude and orbit control
using interaction between
magnetic actuator and space environment**

자기구동기-우주환경 상호작용을 이용한
큐브위성 자세 및 궤도 동시 제어

2018 년 8 월

서울대학교 대학원
기계항공공학부
박 지 현

This page left intentionally blank

Simultaneous CubeSat attitude and orbit control using interaction between magnetic actuator and space environment

by

Ji Hyun Park

A dissertation submitted in partial fulfillment
of the requirements for the degree of
Doctor of Philosophy
at Seoul National University
August 2018

Doctoral Committee:

Professor Chang Don Kee, Chair
Professor Jai-Ick Yoh
Professor Chan Gook Park
Professor In-Seuck Jeung
Senior Assistant Professor Takaya Inamori

This page left intentionally blank

Simultaneous CubeSat attitude and orbit control using interaction between magnetic actuator and space environment

자기구동기-우주환경 상호작용을 이용한
큐브위성 자세 및 궤도 동시 제어

지도교수 여 재 익

이 논문을 공학박사학위논문으로 제출함

2018 년 6 월

서울대학교 대학원

기계항공공학부

박 지 현

박지현의 공학박사학위논문을 인준함

2018 년 8 월

위 원 장 : _____
부위원장 : _____
위 원 : _____
위 원 : _____
위 원 : _____

This page left intentionally blank

Abstract

Simultaneous CubeSat attitude and orbit control
using interaction between
magnetic actuator and space environment

by

Ji Hyun Park

Recent advances in CubeSat technology has shown CubeSat a promising platform not only for space education, but also in its potential in the use for valuable space missions. The value of CubeSat is added when utilizing the low-cost and fast-delivery advantage in operating multiple CubeSats together as a distributed satellite system (DSS) to perform multi-point observation or measurement missions. Depending on how the DSS is configured, valuable missions that conventional monolithic spacecraft could not perform can be realized. In order to take DSS advantage, orbit maneuver capability of CubeSats is required. Various conventional orbit maneuver methods for CubeSat exists, however the methods have its advantages and disadvantages.

In this dissertation, a novel plasma drag interaction using onboard magnetic torquer with space plasma for CubeSat is proposed. Plasma drag constellation takes all the conventional advantages while providing accurate orbit deployment capability to CubeSats.

An elementary analysis is presented as proof-of-concept. Numerical analysis on plasma drag constellation is performed for parametric study and elementary analysis validation. The results show the feasibility of the proposed method and the

relationship between magnetic moment, desired phase angle, and satellite mass with deployment time.

Practical aspects of plasma drag constellation are further analyzed as part of feasibility study. Feasibility diagram is derived based on CubeSat resource limitations and orbit plane perturbation. An example case of plasma drag constellation proves the feasibility of CubeSat using plasma drag constellation. Attitude disturbance problem is considered as another practical issue. The effect of magnetic torquer actuation that drives the satellite attitude unstable is examined. As a mitigation, high frequency polarity switching controller for torque cancellation is proposed. Numerical simulation results show that angular velocity was significantly decreased, however attitude remained unstable. As a solution, a high-frequency switching PD controller is proposed. The PD controller is designed to dump out the residual torque during polarity switching. Simulations show that the proposed high-frequency switching PD controller successfully stabilizes satellite attitude during the magnetic actuation while using magnetic plasma drag for orbit control.

Table of Contents

Abstract	I
List of Tables.....	VII
List of Figures	IX
Chapter 1 Introduction	1
1.1. Background.....	2
1.2. Motivation.....	7
1.2.1. SNUSAT-1/1b	7
1.2.2. SNUSAT-2	9
1.3. Literature Review	9
1.3.1. Differential drag	9
1.3.2. High specific impulse thruster.....	13
1.3.3. High-thrust thruster	15
1.3.4. Requirements for novel CubeSat orbit maneuver.....	17
1.4. Contribution.....	19
1.5. Dissertation outline.....	21
Chapter 2 Interaction between Magnetic Actuator and Space Environment ..	22
2.1. Magnetic Plasma Drag.....	22
2.1.1. Literature Review	22
2.1.2. Space Plasma Environment	23
2.1.3. Magnetic Field Surrounding a Satellite.....	28
2.1.4. Charged Particle Motion in Electric and Magnetic Fields.....	30

2.1.5. Particle-In-Cell Simulation.....	32
2.2. Geomagnetic Torque	38
Chapter 3 Methodology	41
3.1. Plasma Drag Constellation Concept	41
3.2. Analytical Method	44
3.3. Numerical Method.....	49
3.3.1. Constellation Deployment Simulator	50
3.3.2. Attitude Simulator	60
Chapter 4 Plasma Drag Constellation	65
4.1. General Aspects of Plasma Drag Constellation Time.....	65
4.2. Parametric Study of Plasma Drag Constellation.....	65
Chapter 5 Plasma Drag Constellation Feasibility Analysis	72
5.1. Magnetic Moment of a Magnetic Actuator on a CubeSat	72
5.2. Perturbation of Right Ascension of the Ascending Node	74
5.3. Example of a four-CubeSat plasma drag constellation.....	78
Chapter 6 Geomagnetic Torque Mitigation	81
6.1. Transition Characteristics of Magnetic Plasma Drag due to Polarity Switching.....	81
6.2. Effect of High-Frequency Polarity Switching	83
6.3. Practical Consideration on High-Frequency Switching.....	93
Chapter 7 Conclusions	95
4.1. Summary	95
4.2. Future work	100

4.2.1. In-depth study of disturbance torque cancellation.....	100
4.2.2. Advanced simple-IRI model development.....	101
4.2.3. Large MTQ interface development	101
Appendix Analytical solution of magnetic plasma drag	102
Bibliography	105
초 록	114

This page left intentionally blank

List of Tables

Table 1 Emergent capabilities of distributed satellite systems (Corbin, 2015)	5
Table 2 Categorization of Distributed Satellite Systems (Poghosyan et al., 2016) ...	6
Table 3 Feature comparison of conventional constellation deployment technologies	18
Table 4 Simplified IRI model coefficients ($\rho_{\text{plasma},0}, h_0, G_0$) for $A_0=1.435$ (Matsuzawa, 2017).....	26
Table 5 Conditions for example magnetic field data generation around a satellite for a line dipole model without external magnetic field.....	30
Table 6 Reference magnetic plasma drag PIC simulation parameters	32
Table 7 Example values of ρ, V and corresponding plasma drag force for $M_d = 10$ Am^2 . Ion number density and plasma drag force is averaged about a single orbit.....	49
Table 8 Overview of the in-house orbit simulator.....	52
Table 9 Investigated parameters on plasma drag constellation	67
Table 10 Parameters of the reference magnetic torquer (Lee et al., 2005).....	73
Table 11 Parameters used in power margin estimation for 1 U CubeSat	73
Table 12 Magnetic moment limitations due to mass and power requirements for a CubeSat.....	74
Table 13 Constellation orbit plane lifetime and allowable deployment time	76
Table 14 Plasma drag constellation configuration example.....	78
Table 15 Parameters used in attitude disturbance analysis due to primary magnetic torquer in plasma drag constellation	84
Table 16 Recommended TRL definitions by NASA TRA Study Team (Hirshorn and Jefferies, 2016).....	98

This page left intentionally blank

List of Figures

Figure 1 An example of a 1U CubeSat XI-V (left), a 2U CubeSat SNUSAT-1/1b (center), and a 3U CubeSat SNUSAT-2 (right).	3
Figure 2 A 6U deployer from NanoRacks used for deploying CubeSats from ISS ..	3
Figure 3 Total CubeSat launch count and categorization by mission type (Swartwout, 2018). Exponential increase in CubeSat launches and the role of commercial sector in CubeSat development can be seen.....	4
Figure 4 Distribution of 36 CubeSats of the QB50 project. The CubeSats are distributed irregularly as the CubeSats do not have orbit maneuver capabilities. [Courtesy QB50 DPAC].....	8
Figure 5 Actual Flock 1-C constellation deployment results achieved using differential drag. The bold lines indicate the differential drag command on each of the satellites. The figure shows that the CubeSats have been adequately equally spaced (Foster et al., 2015).....	10
Figure 6 Various cross-sectional area configuration for differential drag using physical properties of a Dove satellite (Foster et al., 2015). The deployable solar panels produce larger differential drag between the satellites.....	11
Figure 7 Conceptual art of spacecraft formation flying using drag plates (Varma and Kumar 2012). Drag plates are rotated in order to change differential drag between the satellites.....	12
Figure 8 A conceptual drawing of a CubeSat with foldable sail (Guglielmo et al., 2014).	13
Figure 9 Prototype model of NanoFEEP compared to a 1 Euro coin (Bock and Tajmar, 2018).	14

Figure 10 NanoFEEP assembly level integration requirements due to thruster head, neutralizer, PPU, and high voltage lines occupy relatively large volume.	15
Figure 11 Micro-propulsion payload developed for DELFI-NEXT mission. Solid propellant cold gas generators provided pressure for the cold gas thruster (Bouwmeester et al., 2010).	16
Figure 12 Constituents of the atmosphere with respect to altitude. Solid line shows the daytime and dashed line shows the nighttime ion constituents. The figure shows the dominance of atomic oxygen (O^+) (greater than 90%) at altitudes above 250 km during both daytime and nighttime.	24
Figure 13 Constituents of the atmosphere with respect to diurnal variations at 500 km altitude. The density increases during the day due to the ionization due to interaction of solar extreme ultraviolet (EUV) radiation with atomic oxygen.	25
Figure 14 Simplified IRI modeling the plasma number density depending on longitude and altitude. The solid lines show the simplified IRI model and the dotted lines show the retrieved data from IRI2012. The simplified IRI model is shifted by 60 degrees (\emptyset) for shape matching.	27
Figure 15 Magnetic field generation due to on-board magnetic torquer of the satellite.	29
Figure 16 Magnetic field near a satellite due to the magnetic torquer. Parameters for the magnetic field is given in Table 2.	30
Figure 17 Magnetic plasma drag force from PIC simulation for given conditions in Table 6.	33
Figure 18 Ion number density field (left) and space potential (right) from PIC simulation for given conditions in Table 6.	34

Figure 19 Effect of M_d (top) and ρ_{plasma} (bottom) on plasma drag force. Results show linear relationship of both parameters against plasma drag force.	36
Figure 20 Effect of plasma velocity on plasma drag force. Results show linear relationship.	37
Figure 21 Dependence of the plasma drag force on the magnetic moment angle (Kawashima et al., 2018).	38
Figure 22 Geomagnetic torque depending on magnetic moment due to the interaction between magnetic actuator and geomagnetic field.	39
Figure 23 Disturbance torque of a 575 km sun synchronous orbit due to the interaction between magnetic actuator and geomagnetic field. The magnetic actuator is assumed to be aligned to the ram direction.	40
Figure 24 Conceptual drawing of plasma drag constellation. a) Satellite 1 uses plasma drag to lower the semi-major, increasing the mean motion. b) Satellite 2 uses plasma drag to match the mean motion as the desired phase angle is achieved. c) Satellite 1 and satellite 2 have achieved the desired phase angle with the same mean motion.	42
Figure 25 Comparison between atmospheric drag and magnetic plasma drag in low Earth orbit. Simplified Jacchia77 model with exospheric temperature of 1000 K is used for the atmospheric drag, and simplified IRI2012 model is used for the magnetic plasma drag.	44
Figure 26 Comparison of simplified atmosphere model with the Jacchia 1977 model. The exospheric temperature of the Jacchia 1977 model is set to 1000 K.	51
Figure 27 Damping characteristics of plasma drag constellation depending on ρ_R . $M_d = 10$, $m = 1$, and a) $\rho_R = 1 \times 10^{-1}$, b) $\rho_R = 8 \times 10^{-2}$, and c) $\rho_R = 5 \times 10^{-2}$ showing overdamped, near-critically damped, and underdamped system	

characteristics. The subgraph on the top shows the states (phase angle and phase angle rate), subgraph on the middle shows the orbit altitude, and the subgraph on the bottom shows the control input.....59

Figure 28 Polynomial fit of the magnetic plasma drag loss misalignment of magnetic moment with ram vector given in Figure 21.63

Figure 29 Analytical solution of plasma drag constellation time on magnetic moment for various orbit altitudes and desired phase angles ($m = 1$).66

Figure 30 Comparison between analytical solution (A) and numerical simulation results (N) of plasma drag constellation, depending on phase angle, altitude and magnetic moment on deployment time ($m = 1$).68

Figure 31 Plasma drag constellation numerical simulation results of deployment time depending on the mass of the satellites.70

Figure 32 Plasma drag constellation numerical simulation results of deployment time depending on the orbit altitude of the satellites ($M_d = 10 \text{ Am}^2$ and $m = 1$).71

Figure 33 Satellite mission will be limited as the RAAN (right ascension of the ascending node) changes over time. Example shows the RAAN misalignment effect for SNUSAT-1 and SNUSAT-1b as it passes Central America.75

Figure 34 Plasma drag constellation feasibility diagram showing feasible configurations for 1~3 U CubeSats at 500 km orbit. Green curve shows 1 U feasible limit, yellow curve shows 2 U feasible limit, and blue curve shows 3 U feasible limit along a specific condition.77

Figure 35 Plasma drag constellation example of four 1 U CubeSats at height of 500 km, magnetic moment of 6.2 Am^2 and 90 degree phase angle with $\rho_R =$

9×10⁻². Figure 35a) shows the state, altitude, and control input from top to bottom and Figure 35b) shows the CubeSats on the orbital plane. ...80

Figure 36 Two simulated magnetic field surrounding a spacecraft. Magnetic field surrounding a spacecraft when the magnetic torquer with a magnetic moment of 15 Am² angle is 0 degrees (left) and when the magnetic torquer with a magnetic moment of 15 Am² angle is 180 degrees (right).82

Figure 37 Plasma drag force transition characteristics of a single polarity switching. The polarity of the magnetic torquer was switched at 3 ms after the PIC simulation had converged from its initial conditions.83

Figure 38 Angular velocity and attitude simulation results for constant magnetic moment initially aligned with the ram vector. The attitude becomes unstable due to accumulated disturbance torque.85

Figure 39 High frequency magnetic torquer polarity switching simulation at 100 Hz. Angular velocity decreased significantly, however the attitude is unstable due to the residual torque.86

Figure 40 Hybrid switching PD controller simulation results at 100 Hz. The hybrid controller is able to stabilize both angular velocity and attitude.88

Figure 41 Hybrid switching PD controller simulation results at 200 Hz. The hybrid controller shows better attitude control performance than switching frequency at 100 Hz.89

Figure 42 Hybrid switching PD controller simulation results at 50 Hz. The hybrid controller fails in stabilizing attitude due to large residual torque.90

Figure 43 Dot product value of primary magnetic torquer vector and ram vector for hybrid switching PD controller.91

Figure 44 Evaluation of the loss function at different switching frequencies. An optimal switching frequency considering the overall loss can be seen at 100 Hz92

Figure 45 Modal survey result of a 2U CubeSat, SNUSAT-1/1b. Peaks at high frequency region can be spotted.....93

Chapter 1

Introduction

This dissertation focuses on the simultaneous spacecraft attitude and orbit control using the interaction between magnetic actuators and space plasma, especially on the application to a CubeSat. Previous CubeSats did not have a strong need in orbit maneuver capability due to the mission simplicity. However, as the CubeSat technology evolved, CubeSats are being used in complex missions demanding orbit control. Orbit maneuver mechanisms for CubeSats has been proposed, however the use of such mechanisms are limited due to either mass, volume, power, attitude control requirements.

Magnetic plasma drag has a potential in being used as orbit control by differential drag, as the drag force is generated using onboard magnetic torquers boarded on a CubeSat. Furthermore, as the magnetic torquer produces torque as a result of interaction of the magnetic field of the CubeSat with the geomagnetic field, both attitude and orbit control can be achieved using the same actuator. CubeSat attitude and orbit control using the same actuator is the key advantage as the resource requirements can be minimized. This dissertation presents a novel simultaneous attitude and orbit control mechanism using the same actuator. Orbit maneuver capability and its feasibility using magnetic plasma drag is investigated for a CubeSat, and a simultaneous attitude and orbit control method is developed.

1.1. Background

CubeSat is a standard nanosatellite ranging from 1 – 12 kg in mass (The CubeSat Program, 2015; The CubeSat Program, 2016), which was first proposed in the early 2000s by a group of research teams (Heidt et al., 2000; Puig-Suari et al., 2001). The key features of a CubeSat over a conventional satellite are low cost and fast delivery, coming from the use of commercial-off-the-shelf (COTS) components and small-mass piggy back launch. Conventional space systems used space qualified components, which are expensive compared to COTS components. Furthermore, launch cost became affordable due to the small-mass piggy back launch and finding a launch opportunity became easy due to the standard platform as the CubeSat deployer is shared together. Figure 1 shows an example of most widely used CubeSat platform and Figure 2 shows an example of CubeSats sharing a deployer.

In June 2003, the first batch of six CubeSats [XI-IV (The University of Tokyo), CanX-1 (University of Toronto), AAU-CubeSat (Aalborg University), DTUSat (Technical University of Denmark), CUTE-1 (Tokyo Institute of Technology), QuakeSat-1 (Stanford University)] were launched as a piggy back ride on Rokot (Eishima et al., 2004; Pranajaya et al., 2003). Since the success of the first launch, about 800 CubeSats has been launched proving the use CubeSat for space education and also the space mission capabilities of CubeSats (Poghosyan and Golkar, 2017; Polat et al., 2016; Swartwout, 2013, 2018). According to recent statistics (Swartwout, 2018), the CubeSat boom is due to the increasing number of Distributed Satellite Systems (DSS) of CubeSats, such as QB50, Flock, or Lemur-2 (Bandyopadhyay et al., 2016; Poghosyan and Golkar, 2017).



Figure 1 An example of a 1U CubeSat XI-V [Courtesy The University of Tokyo] (left), a 2U CubeSat SNUSAT-1/1b (center), and a 3U CubeSat SNUSAT-2 (right).

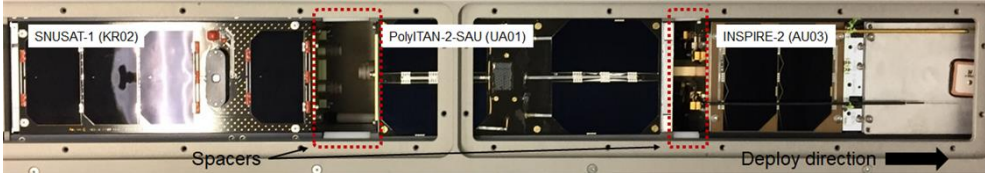


Figure 2 A 6U deployer from NanoRacks used for deploying CubeSats from ISS

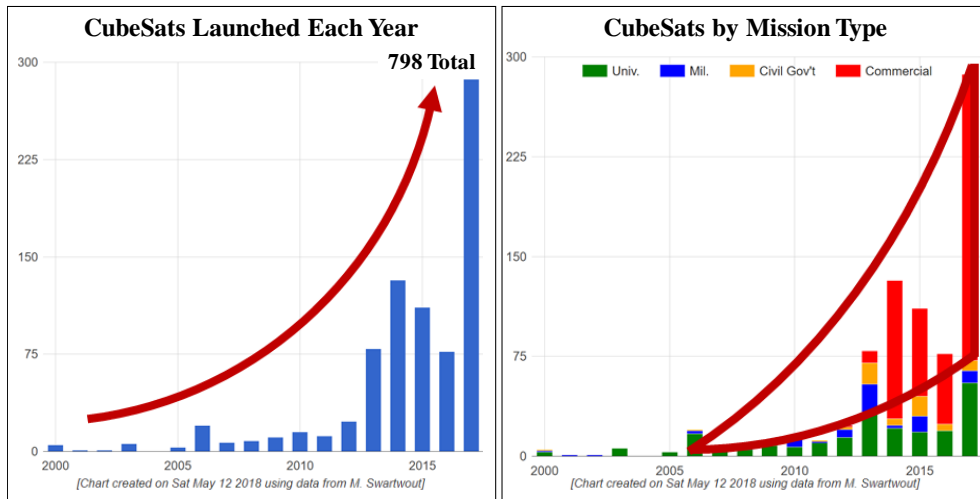


Figure 3 Total CubeSat launch count and categorization by mission type (Swartwout, 2018). Exponential increase in CubeSat launches and the role of commercial sector in CubeSat development can be seen

DSS is a concert of multiple satellites, which enhances the mission capability of the system over a monolithic systems (Corbin, 2015; Poghosyan et al., 2016). The mission capability enhancement includes decentralization of resources, spatial distribution of payloads, more satellites, and redundancy so-called “The Big Four” (Corbin, 2015). The benefits of DSS can be categorized based on unique emergent capabilities, which consists of one or more advantages from “The Big Four,” as “Fundamentally Unique Emergent Capabilities,” “Analytically Unique Emergent Capabilities,” and “Operationally Unique Emergent Capabilities,” as shown in Table 1 (Corbin, 2015).

Table 1 Emergent capabilities of distributed satellite systems (Corbin, 2015)

Capability category	Emergent capabilities	Description
Fundamentally unique	Shared sampling	“When multiple assets trade responsibilities for making the same measurement at different times, particularly when it is impossible for any single asset to make the measurement over the time period required for satisfaction.”
	Simultaneous sampling	“When multiple assets conduct a measurement of a common target at the same time from different locations such that the combination of the resultant data sets provides more detailed information that could not have been gathered by a single asset moving between locations and taking measurements at different times.”
	Self-sampling	“When multiple assets measure signals generated by each other, or the precise position and velocity of each other, to infer information about a target or phenomenon indirectly rather than measuring the phenomenon directly.”
Analytically unique	Census sampling	“When multiple assets conduct multiple measurements of a subset (or the full set) of a collection of similar targets in order to have greater certainty in the variance of the desired properties or characteristics of the whole target population.”
	Stacked sampling	“When heterogeneous assets are deployed into different environments or locations to make measurements of the same phenomenon using different instruments such that the combination of data sets is more valuable than any individual data set.”
Operationally unique	Staged sampling	“When additional assets are deployed after knowledge gained by the first asset’s or wave of assets’ data has been received and analyzed such that the location or orbit of deployment can be re-evaluated and altered to seize opportunity that was previously unknown or provide similar measurements for more confidence in results.”
	Sacrifice sampling	“When assets are knowingly deployed to an unsafe operating environment, such that most if not all of the deployed assets will be destroyed, but the scientific returns can justify the development and launch of the entire mission.”

Table 2 Categorization of Distributed Satellite Systems (Poghosyan et al., 2016)

DSS architectures	Mission goals	Cooperation	Homogeneity	Inter-satellite distance	Autonomy
Constellation	Mission goals shared	Cooperation required to support mission goals	Homogeneous components, some difference possible	Regional	Autonomous
Train	Independent, but could be shared	Cooperation from optional to required	Heterogeneous components	Local	Autonomous
Cluster	Mission goals shared	Cooperation required to support mission goals	Homogeneous components	Local	Autonomous to completely co-dependent
Swarm	Mission goals shared	Cooperation required to support mission goals	From homogeneous to heterogeneous components	From local to regional	Autonomous to completely co-dependent
Fractionated satellite	Mission goals shared	From optional (service areas) to required (distributed critical functions)	Heterogeneous components	Local	Autonomous to completely co-dependent
Federated satellite	Independent mission goals	Ad-hoc, optional	Heterogeneous components	From local to regional	Autonomous

Note: Adapted from Unified Classification for Distributed Satellite Systems, Poghosyan et al., 2016

The variations of DSS architectures are categorized into constellations, trains, clusters, swarms, fractionated satellites, or federated satellites, which are characterized by its mission goals, cooperation, homogeneity, inter-satellite distance, and autonomy as shown in Table 2 (Poghosyan et al., 2016). Regardless of the architecture variations, as DSS involves multiple space segments, fast delivery and low cost features of the CubeSat makes CubeSat a suitable platform in realizing the DSS as long as technical capabilities are met.

1.2. Motivation

The motivation in performing research on a novel constellation deployment method came from CubeSat project experiences, from SNUSAT-1/1b and SNUSAT-2. During the development of CubeSat systems, it was possible to learn the advantage of distributed satellite systems, while experiencing the limitations of the current CubeSat technology. The experiences became the key motivating factor in performing this research.

1.2.1. SNUSAT-1/1b

SNUSAT-1/1b is a 2U CubeSat project part of the QB50 mission (Park et al., 2014). The QB50 project is an international collaboration for lower thermosphere exploration (Gill et al., 2013). It utilizes 36 (originally 50) CubeSats to measure lower thermosphere constituents with high temporal and spatial resolution. The CubeSats did not have onboard orbit maneuver mechanisms, which limited the constellation to be deployed naturally due to variations in ballistic coefficient and

deployment velocity (Kılıc et al., 2013). The irregularly distributed QB50 CubeSats can be seen in Figure 4. A strong motivation in the development of CubeSat orbit maneuver capability came along with the experience of distributed satellite systems using CubeSats with the QB50 project, while urging for the need of orbit maneuver capability in able to fully utilize the advantage of CubeSats as a distributed satellite system.



Figure 4 Distribution of 36 CubeSats of the QB50 project. The CubeSats are distributed irregularly as the CubeSats do not have orbit maneuver capabilities. [Courtesy QB50 DPAC]

1.2.2. SNUSAT-2

SNUSAT-2 is a 3U CubeSat developed for technology demonstration (Park et al., 2015). From the experience of SNUSAT-1/1b, SNUSAT-2 boarded a high specific impulse thruster. However, despite the small thruster head, power processing unit, high voltage lines, and neutralizer made the actual volume margin tight. Adding additional components, especially high voltage was challenging on a CubeSat. From the experience of SNUSAT-2, using onboard magnetic actuators as constellation deployment mechanism worked as a strong motivating factor.

1.3. Literature Review

A literature review has been performed in order to identify the issues of on the current CubeSat orbit maneuver technology. Various orbit maneuver technologies have either been proposed or demonstrated using differential drag, high-thrust thruster, or high specific impulse thruster. Each of the technologies are reviewed in this section.

1.3.1. Differential drag

Differential drag is in fact one of the most promising orbit maneuver method for CubeSats up until now. Successful mission was reported using differential drag for Earth observation CubeSat constellation (Boshuizen et al., 2014; Foster et al., 2015). Figure 5 shows an actual Flock 1-C constellation deployment result achieved

using differential drag (Foster et al., 2015). The figure shows that adequate orbit deployment is possible using differential drag.

Differential drag can be categorized into three variations as differential drag using drag plate, differential drag using physical properties, and differential drag using foldable sails. Differential drag using physical property utilizes the area ratio of the different cross-sectional areas of the CubeSat (Boshuizen et al, 2014; Foster et al., 2015). Therefore, differential drag using physical property is more effective on larger CubeSat platforms or CubeSats with deployable panels. The deployable panels produce larger differential drag between the satellites.

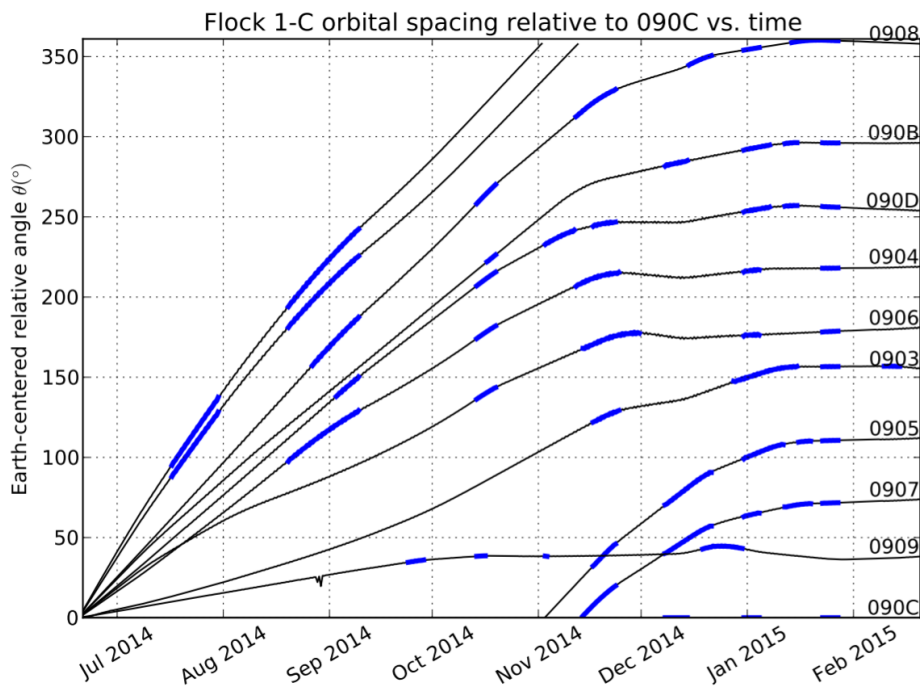


Figure 5 Actual Flock 1-C constellation deployment results achieved using differential drag. The bold lines indicate the differential drag command on each of the satellites. The figure shows that the CubeSats have been adequately equally spaced (Foster et al., 2015).

Figure 6 shows the different configurations of differential drag using physical property of a Dove satellite (Foster et al., 2015). Whereas area ratio variation is only 1.5 for 1 U CubeSat, Dove satellite achieved an area ratio of 9.75 using the large panels. According to Figure 5, it can be seen it took 7 months for the Flock 1-C to deploy to its constellation.

If the spacecraft has deployable panels and has three-axis control ability, differential drag using physical property is a promising method. However, the discrete configuration options limit precise deployment, as high frequency control maneuver is physically impossible.

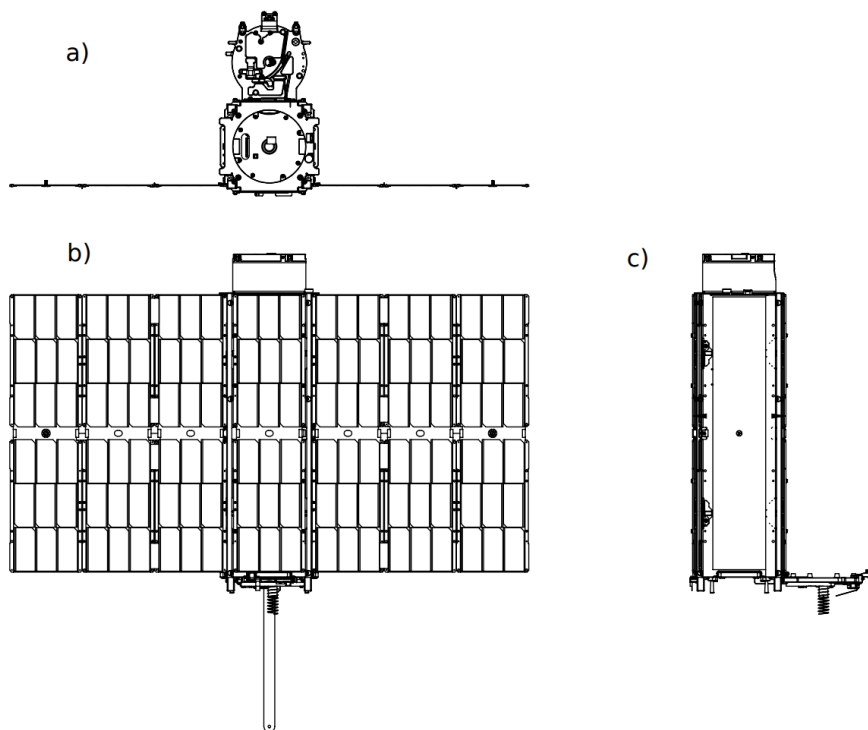


Figure 6 Various cross-sectional area configuration for differential drag using physical properties of a Dove satellite (Foster et al., 2015). The deployable solar panels produce larger differential drag between the satellites.

Differential drag using a drag plate utilizes drag plates that can be rotated for varying atmospheric drag (Bevilacqua and Romano, 2008; Varma and Kumar, 2012). The advantage of differential drag using drag plates over differential drag using physical property is that aero-ratio or the differential drag can be controlled using a continuous profile. However, the drawback due to the requirement of additional drag plates is a trade-off to volume and mass. Figure 7 shows a conceptual art of spacecraft formation flight using drag plates (Varma and Kumar 2012).

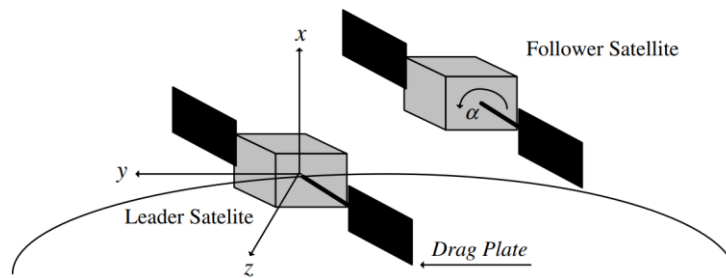


Figure 7 Conceptual art of spacecraft formation flying using drag plates (Varma and Kumar 2012). Drag plates are rotated in order to change differential drag between the satellites.

Lastly, differential drag using foldable sail is a new concept that uses foldable sail to control the cross-sectional area (Guglielmo et al., 2014; Mason et al., 2013; Pastorelli et al., 2015). The foldable sail however requires an additional folding and unfolding mechanism, and also requires attitude three-axis control if continuous profile differential drag is required. A conceptual drawing of foldable sail is shown in Figure 8 (Guglielmo et al., 2014).

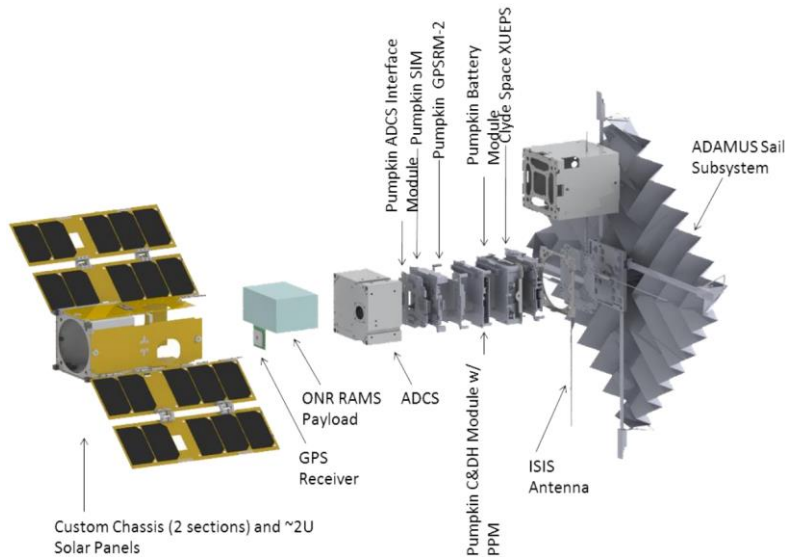


Figure 8 A conceptual drawing of a CubeSat with foldable sail (Guglielmo et al., 2014).

1.3.2. High specific impulse thruster

The characteristics of high specific impulse thrusters is generally low thrust. As definition, high specific impulse thrusters have higher propellant efficiency, thus could sound ideal to small spacecraft platforms such as CubeSats. Many high specific impulse thrusters have been developed that could be board on to CubeSats including pulsed plasma thrusters (PPT), vacuum arc thrusters (VAT), ion/hall thrusters, or electrospray thrusters (Mueller et al., 2010). In this section, some of the most recent development in ion thruster, PPT, and field emission electrical thruster (FEET) are reviewed.

Ion thrusters fundamentally accelerate ions up to high speed, which increases the specific impulse. A recent study featured a CubeSat sized neutralizer-free ion thruster, which benefits from that fact that neutralizer is not required (Rafalskyi and

Aanesland, 2017). Traditionally, neutralizer was required to balance out the exhaust beam, in order to prevent the spacecraft from attracting the ions. Despite the neutralizer-free feature, ion thrusters require propellant tank, feedline, and power processing unit (PPU) while three-axis attitude control is required for thrust vectoring.

PPTs unlike ion thrusters use solid Teflon as propellant, and thus does not require a propellant tank or complex feedline systems. Recent studies on PPT featured geometry and propellant optimization in order increase the overall performance of PPT (Northway et al., 2017). Despite the features, PPT requires large volume due to its PPU and capacitor bank for energy storage. A 2U CubeSat is planned to be launched boarding PPT for technology demonstration for future lunar missions (Örger et al., 2016).



Figure 9 Prototype model of NanoFEEP compared to a 1 Euro coin (Bock and Tajmar, 2018).

FEEP provides high specific impulse features due to extremely high ion acceleration. Miniaturization is possible as propellant evaporation, ionization, and acceleration takes place in the same electric field. Recent development featured miniaturization of FEEP to a size, which fits in the edge of CubeSat rails (Bock and

Tajmar, 2018). A manufactured prototype of the NanoFEEP thruster is shown in Figure 9 (Bock and Tajmar, 2018). NanoFEEP ready boards gallium, which is phase changed to liquid using electric heater.

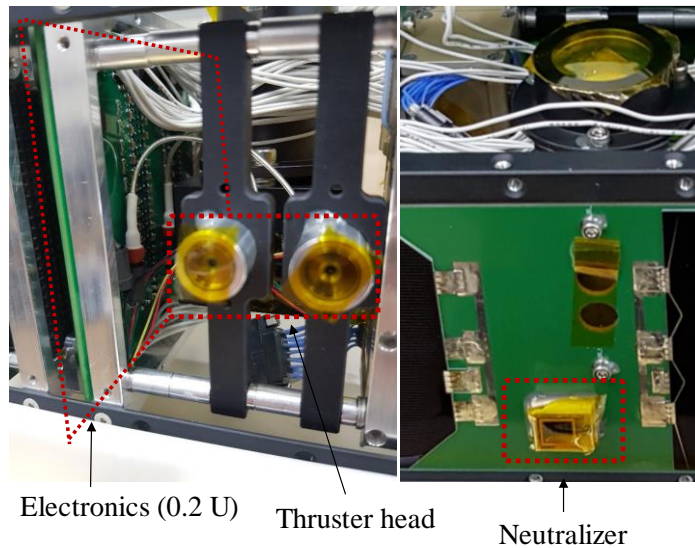


Figure 10 NanoFEEP assembly level integration requirements due to thruster head, neutralizer, PPU, and high voltage lines occupy relatively large volume.

Although the thruster itself is small in mass and volume, additional components such as PPU, neutralizer, and high voltage line assembly requirements occupy relatively large volume as seen in Figure 10.

1.3.3. High-thrust thruster

High-thrust thrusters are used in order to produce large delta-V over a short period of time. Recent developments include resistojet, cold gas thruster, and hydrazine for CubeSat platforms, especially for use in high delta-V missions such as

lunar missions or formation flying (Asakawa et al., 2017; Bouwmeester et al., 2010; Schmuland et al., 2011).

A 6U CubeSat, EQUULEUS, is being developed for deep space exploration as it flies to the Earth-moon L2 (Asakawa et al., 2017). In order to perform such missions, a resistojet that uses water as propellant, named AQUARIUS is being developed. Water was used as a safe, non-toxic, and low-cost propellant, which is promising for university development.

Although the cold gas thruster is low efficiency, it is the simplest and no feedlines are required as it uses solid propellant in generating the required gas. As part of the DELFI-NEXT mission, a micro-propulsion payload was developed for CubeSat orbit control mission (Bouwmeester et al., 2010). Multiple cold gas generators were clustered together assembled with a MEMS based valve and a plenum, as shown in Figure 11.

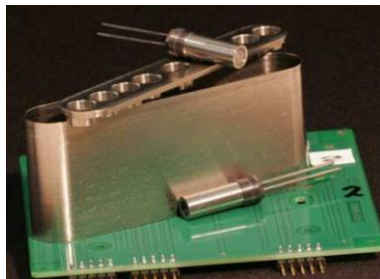


Figure 11 Micro-propulsion payload developed for DELFI-NEXT mission. Solid propellant cold gas generators provided pressure for the cold gas thruster (Bouwmeester et al., 2010).

In order to provide a solution that overcomes the performance limitations of cold gas thrusters, hydrazine propulsion module for CubeSat has been studied

(Schmuland, 2011). However, it must be kept in mind that hydrazine is highly toxic and thus act as a limiting factor in CubeSats being developed in universities.

1.3.4. Requirements for novel CubeSat orbit maneuver

In the previous section, literature review on orbit maneuver technology applicable on CubeSat was performed. The technologies in the literature review were then assessed under five different criteria, which was considered to be an important factor when integrating to a CubeSat: Additional component requirements, deployment requirements, propellant requirements, attitude maneuver requirements, and resource feasibility.

Table 3 shows the criteria assessment results of the orbit maneuver technologies that were introduced previously. It can be seen that differential drag using physical properties is a promising method, especially if the CubeSat has deployable solar panels and has three-axis control capabilities. However, a critical limitation of differential drag using physical properties that the satellite attitude must be maneuvered in order to vary differential drag and the discrete cross-sectional area configuration remains. Especially due to the discrete cross-sectional area configuration, precise phase and phase rate control is impossible, which will require the CubeSats to perform frequency station keeping maneuvers.

Table 3 Feature comparison of conventional constellation deployment technologies

Constellation deployment mechanism	Additional component requirements	Deployment requirements	Propellant-less (De-orbit after mission lifetime possible?)	Attitude maneuver requirements	Mass, volume, and power feasibility
Differential drag using drag plate	Drag plate rotating mechanism required	Drag plate deployment required	Feasible	Three axis control required	Feasible
Differential drag using physical properties	Feasible	Optional (panel deployment)	Feasible	Three axis control required	Feasible
Differential drag using foldable sails	Folding mechanism required	Sail deployment required	Feasible	Feasible (ram direction alignment)	Volume required for folding mechanism
High-thrust thruster	Thruster assembly required	Feasible	Propellant required	Thrust vector control required	Mass, volume required for tank and feedlines
High specific impulse thruster	Thruster assembly required	Feasible	Propellant required	Thrust vector control required	Mass, volume required for tank and feedlines

1.4. Contribution

The main contribution in the thesis is proposition of a novel method for simultaneous CubeSat attitude and orbit control using an onboard actuator. Conventional actuators were solely used either for attitude maneuver or orbit maneuver. In case of thrusters, multiple thruster heads are required in order to achieve both attitude and orbit maneuver. The proposed method uses onboard magnetic actuators, therefore no additional components are required, no deployments are required, no propellant is required, no attitude maneuver is required, while providing continuous acceleration profile. The proposed work especially contributes to small platforms such as CubeSats, where the previously mentioned advantages are necessary. The specific contributions are listed:

- Plasma drag constellation, a novel method using magnetic plasma drag as differential drag is proposed. The interaction between onboard magnetic actuator and space plasma is used in order to produce magnetic plasma drag. The advantages of plasma drag constellation over conventional methods are: (1) no additional components are required; (2) no deployments are required; (3) no propellant is required; (4) no attitude control is required in changing the differential drag; and (5) continuous profile drag can be generated.
- Plasma drag constellation is evaluated using analytical and numerical methods. A 1-D analytical solution is derived showing the relation between various parameters against the constellation deployment time. The numerical method uses phase and its rate in order to derive the relative motion of long distance satellites in a constellation. The numerical results on plasma drag constellation validates the analytical solution.

- Feasibility of plasma drag constellation is analyzed for CubeSat platforms. The upper bound of the constellation deployment time is derived from the perturbation of right ascension of the ascending node. The lower bound of the constellation deployment time is derived from the physical limitations of CubeSat platforms. A feasibility diagram regarding various CubeSat platforms is presented, which can be used in preliminary design of a system using plasma drag constellation.
- A four-CubeSat plasma drag constellation example is formulated. The results successfully show the feasibility of plasma drag constellation on CubeSat systems.
- Mitigation solution to geomagnetic torque is presented. A high-frequency polarity switching PD controller is proposed in order to cancel the geomagnetic torque while aligning the magnetic moment with the ram vector. Effect of the polarity switching frequency is examined.
- The overall loss of magnetic plasma drag due to magnetic moment misalignment against ram vector and magnetic plasma drag transition due to polarity switching is examined. Numerical simulations on different switching frequencies are performed, which an optimal switching frequency for the proposed high-frequency polarity switching PD controller was found.
- Future work in order to increase the technology readiness level of plasma drag constellation is discussed.

1.5. Dissertation outline

This thesis presents the study on simultaneous CubeSat attitude and orbit control using interaction between magnetic actuator and space environment, especially on the application of constellation deployment. Chapter 2 presents the background on magnetic plasma drag and geomagnetic torque. Chapter 3 presents the methodology including analytical and numerical methods and mathematical models used throughout the thesis. The analytical and numerical results of plasma drag constellation analysis are presented in Chapter 4, and the feasibility analysis on the plasma drag constellation is presented in Chapter 5. Chapter 6 deals the geomagnetic torque mitigation due to the interaction between magnetic actuator and geomagnetic field. The high-frequency switching PD controller proposed for geomagnetic torque mitigation solution is evaluated. Lastly, Chapter 7 summarizes the thesis and discusses on the future work in order to increase the technology readiness level (TRL) of the novel technology.

Chapter 2

Interaction between Magnetic Actuator and Space Environment

This chapter introduces the background of the interaction between magnetic actuator and space environment. The interaction between magnetic actuator and space plasma results a drag force so-called ‘magnetic plasma drag force,’ which is used as the means of orbit maneuver in the magnetic plasma drag constellation deployment. Another interaction between magnetic actuator and geomagnetic field results an external torque on the satellite so-called ‘geomagnetic torque.’

2.1. Magnetic Plasma Drag

Magnetic plasma drag is a drag force as a result of the interaction between the magnetic field surrounding a satellite and space plasma. This section explains the background and introduces the fundamentals of magnetic plasma drag required in using magnetic plasma drag as orbit maneuver mechanism.

2.1.1. Literature Review

The idea of using the interaction between magnetic field and space plasma to generate force for interplanetary/interstellar travel was proposed as a magnetic sail, or a MagSail (Andrews and Zubrin, 1990; Zubrin and Andrews, 1991). The plasma source of MagSail is solar wind, which at a large distance the plasma wind density decreases. In order to overcome this issue, the MagSail requires a large

superconducting loop ranging from few tens of kilometers up to few hundreds of kilometers. A modified concept of MagSail was proposed in order to reduce the size of the sail utilizing electromagnetic field with plasma injection to reduce the required sail size and to provide a constant force regardless of the distance (Winglee, 2000). Feasibility studies on the MagSail were performed through magnetohydrodynamic (MHD) simulations (Funaki et al., 2003; Nishida et al., 2005, 2006), Particle-in-Cell (PIC) simulations (Ashida et al., 2014), and experimental studies (Funaki et al., 2007a, 2007b).

However, the size of previously proposed MagSail is large as it has to capture the plasma from the solar wind. In order to further decrease the size of the system, magnetic plasma drag using ionospheric plasma instead of solar wind has been proposed (Inamori et al., 2015a, 2015b). Analytical analysis on the magnetic plasma drag (Matsuzawa, 2017) and PIC simulations using fully kinetic model (Kawashima et al., 2015, 2018) were performed. The study results showed that magnetic plasma drag can be utilized in deorbiting a CubeSat.

The proposed method utilizes the results from magnetic plasma deorbit, in order to control the mean motion of the orbit of a nanosatellite for constellation deployment (Park et al., 2018). The rest of the chapter describes the background on the plasma drag force generated due to the interaction between magnetic actuator and the space plasma.

2.1.2. Space Plasma Environment

Satellites orbiting in the upper atmosphere of the Earth, typically at altitudes of high up to 800~1,000 km is exposed to space plasma (Barth, 2003; Belehaki et al., 2009; Pisacane, 2008). At the higher altitudes of the atmosphere, known as

ionosphere, the exospheric temperature can rise as high up to 2,000 K due to excess of energy carried by Extreme Ultraviolet (EUV/XUV) during the daytime, and due to proton and electron precipitation during the nighttime (Belehaki et al., 2009, p. 273; Pisacane, 2008). This causes ionization, dissociation, excitation and heating, resulting the ionosphere to be composed of various molecular ions (N_2^+ , NO^+ , O_2^+), atomic ions (H^+ , N^+ , and O^+), and electrons.

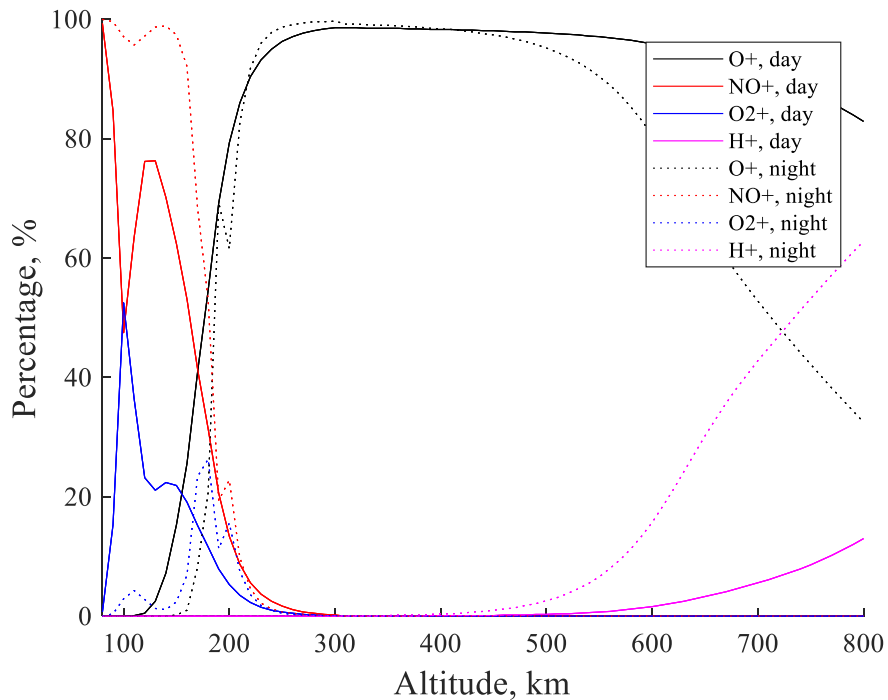


Figure 12 Constituents of the atmosphere with respect to altitude. Solid line shows the daytime and dashed line shows the nighttime ion constituents. The figure shows the dominance of atomic oxygen (O^+) (greater than 90%) at altitudes above 250 km during both daytime and nighttime.

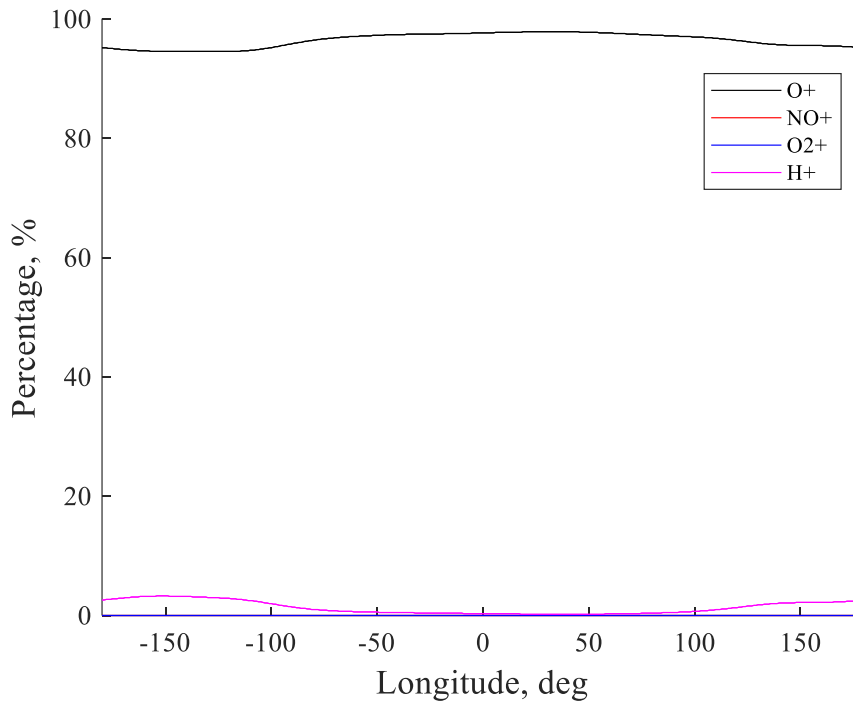


Figure 13 Constituents of the atmosphere with respect to diurnal variations at 500 km altitude. The density increases during the day due to the ionization due to interaction of solar extreme ultraviolet (EUV) radiation with atomic oxygen.

In order to simulate the interaction between space plasma and the magnetic field of the spacecraft, space plasma environment must be modeled accordingly. The International Reference Ionosphere (IRI) is one of the models, which model the plasma environment (Belehaki et al., 2009; Bilitza et al., 2014). The ion and electron densities at the ionosphere can be acquired using the IRI with relative to the altitude and geolocation (latitude and longitude), as shown in Figure 12 and Figure 13.

According to Figure 12 and Figure 13, it can be seen that atomic oxygen (O^+) is dominant at orbit altitudes above 250 km to 800 km, which corresponds to general low Earth orbiting satellite orbit altitudes. Using this characteristics of LEO space

plasma environment, the space plasma environment is simplified by only considering atomic oxygen (O^+) species throughout the study.

Since the IRI requires heavy computation, it is difficult to use IRI for long term numerical analyses in the sensitivity analysis. In this research, the details of plasma number density at the local microscopic level is not of great interest, as the plasma model can be later improved. However, the macroscopic characteristics must be considered as the plasma number density distribution differs according to orbit altitude and condition of sun exposure, which may affect the constellation deployment characteristics. Therefore, a simplified IRI model is used in this study, which characterizes the macroscopic characteristics of IRI for faster computation.

The simplified IRI model is given as Equation (1). ρ_{plasma} , $\rho_{\text{plasma},0}$, A_0 , u , h , h_0 , and G_0 denotes plasma number density, reference plasma number density, longitudinal scale factor, longitude, height, reference height, and height scale factor respectively. The values of ρ_{plasma} , $\rho_{\text{plasma},0}$, A_0 , u , h , h_0 , and G_0 are given in Table 4.

Table 4 Simplified IRI model coefficients ($\rho_{\text{plasma},0}$, h_0 , G_0) for $A_0=1.435$ (Matsuzawa, 2017)

Orbit altitude h, [km]	Reference height, h_0, [km]	Height scale factor, G_0, [km]	Reference density, $\rho_{\text{plasma},0}$, [m^{-3}]
400 – 500	400	138.86	2.740×10^{11}
500 – 600	500	150.52	1.333×10^{11}
600 – 700	600	183.85	0.686×10^{11}
700 – 800	700	225.45	0.398×10^{11}
800 – 900	800	272.91	0.256×10^{11}
900 – 1000	900	325.23	0.177×10^{11}
1000 –	1000	381.86	0.130×10^{11}

$$\rho_{\text{plasma}} = \rho_{\text{plasma},0} \exp\{A_0 \cos(u + \phi)\} \exp\left(-\frac{h - h_0}{G_0}\right) \quad (1)$$

The plasma number density is modeled by sectoring orbit altitude with reference plasma density and exponential terms in order to characterize the plasma number density distribution due to orbit altitude and the condition of sun exposure. The first exponential term describes the distribution due to condition of the sun by introducing the longitudinal term u with a shifting factor ϕ for shape matching, and the second exponential term describes the distribution due to orbit altitude.

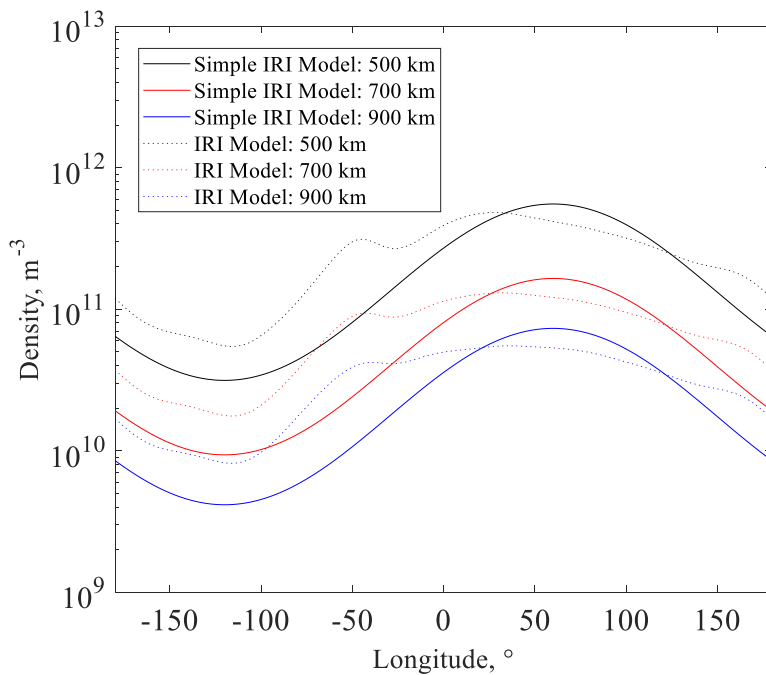


Figure 14 Simplified IRI modeling the plasma number density depending on longitude and altitude. The solid lines show the simplified IRI model and the dotted lines show the retrieved data from IRI2012. The simplified IRI model is shifted by 60 degrees (ϕ) for shape matching.

The simplified IRI model depending on longitude and orbit altitude is compared with the data retrieved from IRI2012 model, which is shown in Figure 14. The effect of orbit altitude and longitude (daylight) can be seen from the figure, with lower plasma number densities at lower orbit altitudes. Throughout the rest of the work presented in the thesis, the simplified IRI model is used in order to reduce computational cost during the numerical simulations.

2.1.3. Magnetic Field Surrounding a Satellite

Magnetic field surrounding a satellite is one of the key factors in magnetic plasma drag, as the magnetic field magnetizes the electrons with small Larmor radius (Kawashima et al., 2018). The details in the charged particle motion in electric and magnetic fields are described in the following section, while this section describes the magnetic field model surrounding a satellite used throughout the thesis.

The magnetic field surrounding a satellite can be controlled using an onboard magnetic actuator such as a large coil. Motor drivers such as H-bridge, which allows current to flow in either direction, typically drive the coils. Using H-bridge, current flow can be controlled while maintaining the required polarity. From the voltage level and coil properties, the current flow in the coil is decided. Coil characteristics such as number of turns, cross sectional area, core with current flow makes up the strength of the magnetic field that the magnetic actuator can generate.

In this study, the magnetic actuator is modeled as a line dipole with the vector potential as shown in Equation (2). θ is the angle of the dipole with respect to the relative plasma flow as shown in Figure 15.

$$A_z = \frac{\mu_0}{2\pi} M_d (-x \cos \theta + y \sin \theta) (x^2 + y^2)^{-1} \quad (2)$$

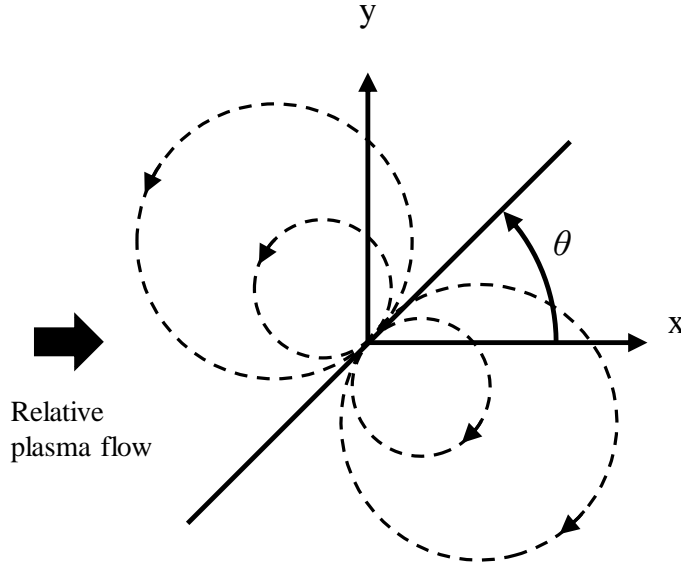


Figure 15 Magnetic field generation due to on-board magnetic torquer of the satellite.

Then, the two-dimensional magnetic field is calculated by using Equation (3).

$$B = \nabla \times A_z \quad (3)$$

The magnetic field data around the satellite is generated based on Equation (3), which is then used for solving the electrostatic and electromagnetic forces. An example of the magnetic field around the satellite is shown in Figure 16. The parameters of the generated magnetic field is given in Table 5.

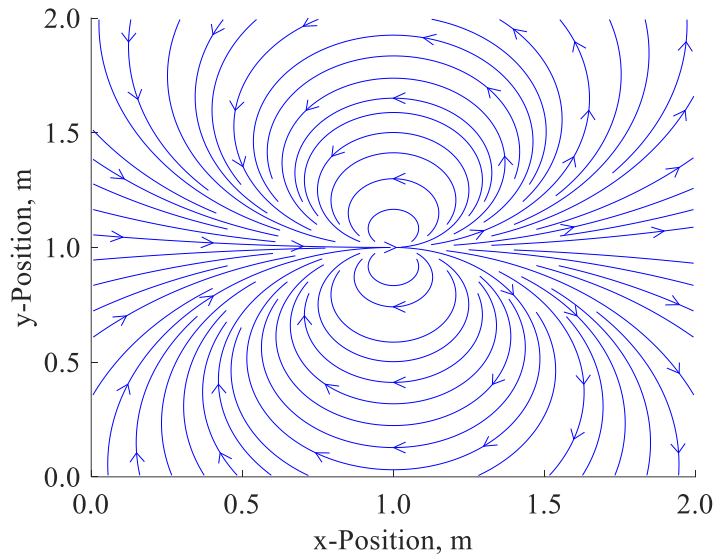


Figure 16 Magnetic field near a satellite due to the magnetic torquer. Parameters for the magnetic field is given in Table 2.

Table 5 Conditions for example magnetic field data generation around a satellite for a line dipole model without external magnetic field.

Magnetic field size	2 m x 2 m
Number of grids	200 x 200
Magnetic moment	15 Am ²
Angle of magnetic pole	0°
External magnetic field	0 T
Angle of external magnetic field	0°

2.1.4. Charged Particle Motion in Electric and Magnetic Fields

The electric and magnetic fields affecting charged particle motion in space plasma generate magnetic plasma drag as a result of momentum change in the charged particles.

The charged particle motion in electric and magnetic fields is described by the Lorentz force given in Equation (4).

$$m_s \frac{d\vec{v}_s}{dt} = q(\vec{E} + \vec{v}_s \times \vec{B}) \quad (4)$$

According to Equation (4), the charged particles are accelerated along the electric field. On the other hand the charged particles are accelerated along the cross product of the velocity of the charged particle and the magnetic field. This implies that if the perpendicular component of the magnetic field with respect to the velocity is large, charged particles with small Larmor radius can be temporarily captured, while the trajectory of charged particles with a significantly large Larmor radius will not be affected much. Under the same magnetic field and initial velocity, the Larmor radius, or the gyroradius, r_g , given in Equation (5), is larger depending on the electric charge and the mass of the charged particle.

$$r_g = \frac{mv_{\perp}}{|q|B} \quad (5)$$

As previously discussed in Section 2.1.2, only the O^+ ions are considered, therefore under same conditions, the Larmor radius is affected only by the mass of the ions and the electrons.

2.1.5. Particle-In-Cell Simulation

In order to acquire the magnetic plasma drag force due to the interaction between space plasma and magnetic field, the Particle-In-Cell (PIC) method (Kawashima et al., 2015, 2018) is used. The PIC method simulates by solving the full kinetic model of the ion and electron motions, which are accelerated by the electrostatic and magnetostatic forces. In the PIC method, multiple particles are bundled into a single macroparticle in order to reduce the computational cost in performing the full kinetic model calculation. For a given magnetic field surrounding the satellite, electrostatic field calculation, ion motion calculation, and electron motion calculation is performed until convergence in the magnetic plasma drag PIC simulation.

Table 6 Reference magnetic plasma drag PIC simulation parameters

Magnetic moment of MTQ	15 Am ² , 0 degrees
Ion number density	1×10 ¹¹ m ⁻³
Ion species	O ⁺
Ion temperature	1500 K
Electron temperature	2500 K
Relative plasma velocity	8 kms ⁻¹
Satellite dimension	10 cm
Physical grid size	2 m x 2 m
Number of grids	200 x 200 (1 cm resolution)

An in-house developed PIC simulator by Kawashima (Kawashima et al., 2015, 2018) is used in calculating the magnetic plasma drag. A reference magnetic plasma drag is calculated using the PIC simulator, and the reference magnetic plasma drag force is used in order to yield plasma drag force at other conditions using parametric relations. The reference magnetic plasma drag is simulated using the parameters

given in Table 6, and the simulation results are given in Figure 17 and Figure 18. Figure 17 shows the history of plasma drag force calculation profile, which shows that the plasma drag force converges around 3 ms. Figure 18 shows the density field and the space potential of the PIC simulation respectively. The momentum exchange of the ions due to the space potential built up in front of the spacecraft can be seen in the figure.

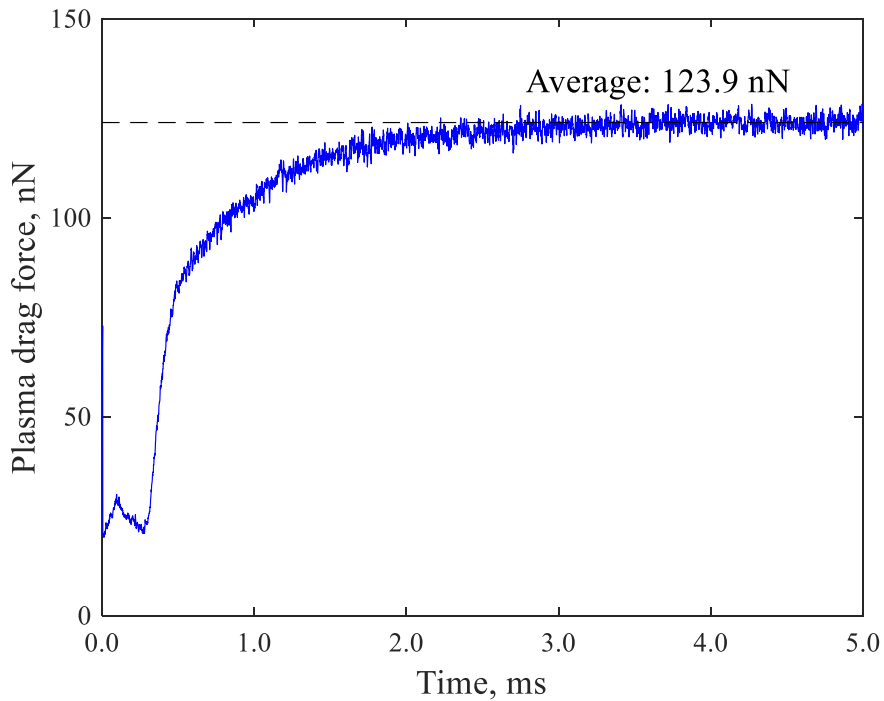


Figure 17 Magnetic plasma drag force from PIC simulation for given conditions in Table 6.

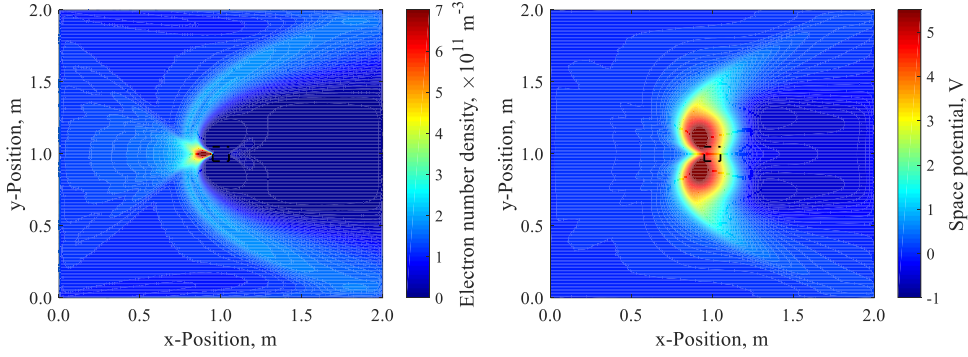


Figure 18 Ion number density field (left) and space potential (right) from PIC simulation for given conditions in Table 6.

The parametric relations are expressed in relation with magnetic moment of the magnetic torquer, M_d , plasma number density, ρ_{plasma} , and relative plasma velocity, V , as given in Equation (6) (Matsuzawa, 2017).

$$F_{\text{plasma}} = \frac{M_d}{M_{ds}} \frac{\rho_{\text{plasma}}}{\rho_s} \frac{V^2}{V_s^2} F_s \quad (6)$$

The reference magnetic plasma drag parameters are given as, $M_{ds} = 15 \text{ Am}^2$, $\rho_s = 10^{11} \text{ m}^{-3}$, $V_s = 8000 \text{ ms}^{-1}$, and $F_s = 136.7 \times 10^{-9} \text{ N}$ representing the reference magnetic moment, reference plasma number density, reference plasma velocity and corresponding reference plasma drag force respectively.

PIC simulations are performed in order to evaluate the parametric relations of Equation (6). The PIC simulation results are shown in Figure 19 and Figure 20. According to PIC simulations on M_d and ρ_{plasma} it has been confirmed that

plasma drag force follows Equation (6) as shown in Figure 19. In case of relative plasma velocity, linear relation was seen in the PIC simulations as shown in Figure 20, which does not match Equation (6). In another study on MagSail, MagSail force had a relationship of $F_{\text{Magsail}} \propto u_{sw}^{4/3}$ where u_{sw} is solar wind velocity (Funaki et al., 2007a). In case of the MagSail, solar wind was considered to be 400 km/s, which is outside the plasma velocity boundaries in low Earth orbit. Furthermore in a low Earth orbit, considering the reference plasma velocity of 8000 ms^{-1} , the difference due to the plasma velocity term is about 6 % at 500 km and 1000 km.

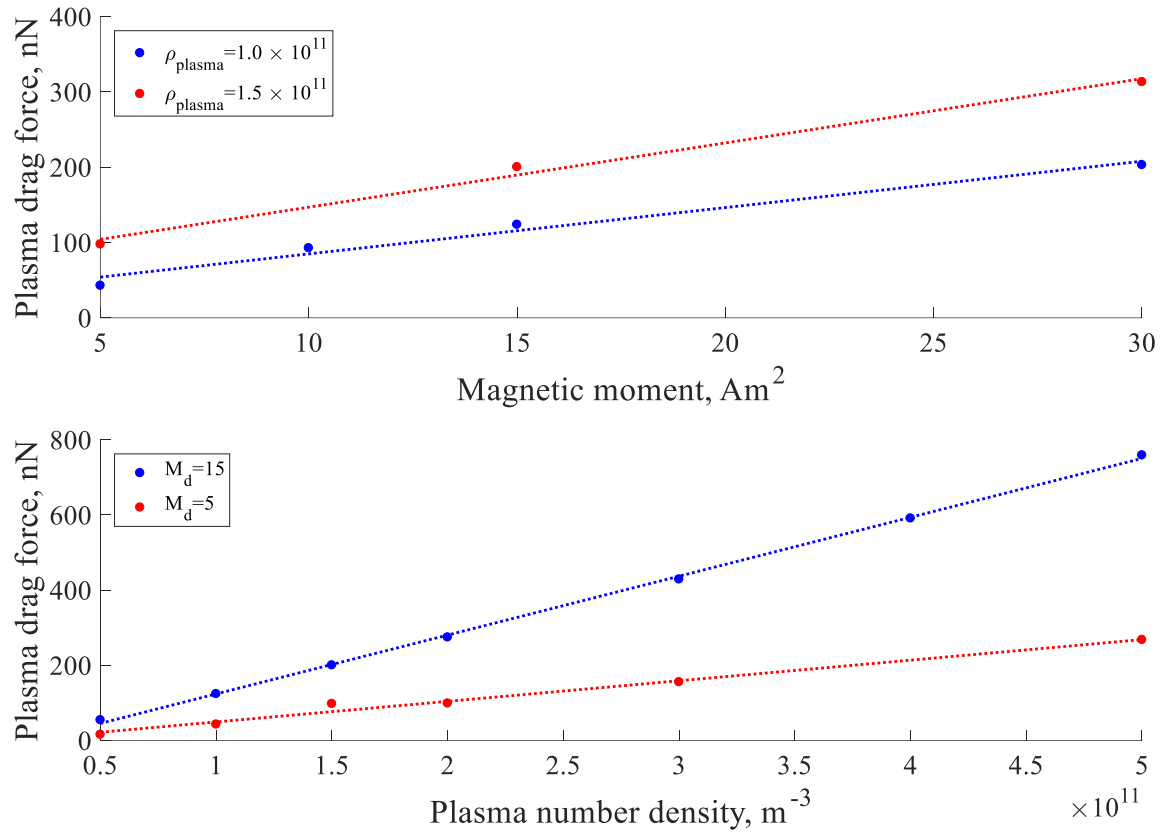


Figure 19 Effect of M_d (top) and ρ_{plasma} (bottom) on plasma drag force. Results show linear relationship of both parameters against plasma drag force.

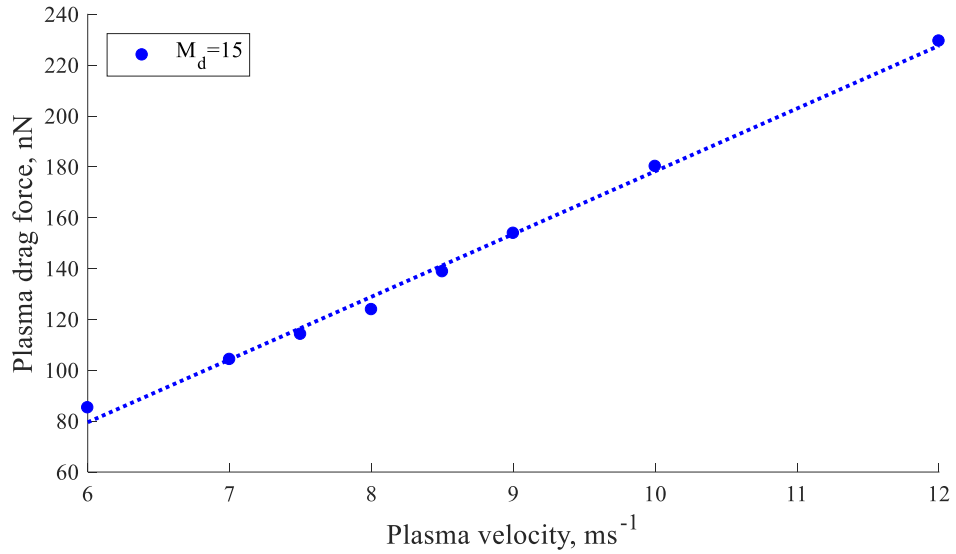


Figure 20 Effect of plasma velocity on plasma drag force. Results show linear relationship.

Considering the fact that the absolute variation is small and that the change rate of the velocity term is small compared to change rate in plasma number density as Equation (7), the velocity term is neglected.

$$\frac{1}{\rho_{\text{plasma}}} \frac{\partial \rho_{\text{plasma}}}{\partial a} \gg \frac{1}{V^2} \frac{\partial V^2}{\partial a} \quad (7)$$

2.2. Geomagnetic Torque

In the previous sections, only orbital elements were considered throughout plasma drag constellation. However, the alignment of magnetic torquer is important in plasma drag force. According to a study on the parameters of magnetic torquer on plasma drag force (Kawashima et al., 2018), plasma drag force decreased from magnetic torquer misalignment as shown in Figure 21.

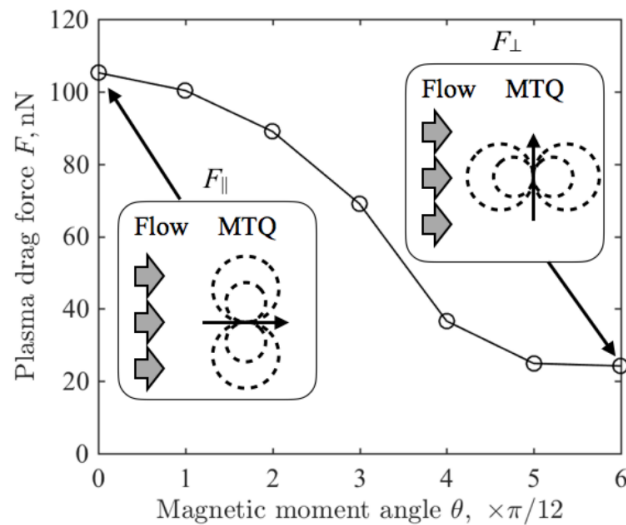


Figure 21 Dependence of the plasma drag force on the magnetic moment angle (Kawashima et al., 2018).

Therefore, in order to accomplish plasma drag constellation with the constellation deployment time as analyzed in the previous sections, it is important to keep the magnetic torquer aligned with the velocity vector of the satellite, or so-called the ram direction.

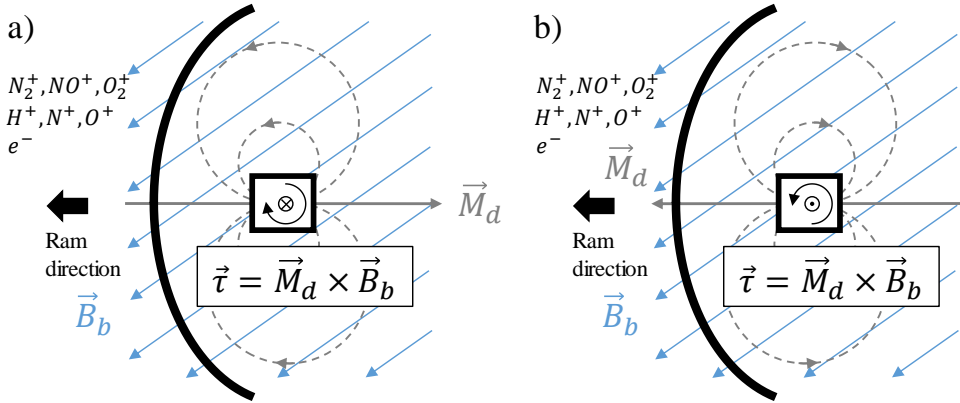


Figure 22 Geomagnetic torque depending on magnetic moment due to the interaction between magnetic actuator and geomagnetic field.

However, in low Earth orbit, disturbance torque acts on satellite body due to the interaction between the magnetic torquer and geomagnetic field, as shown in Figure 22. Actually, satellites used this interaction in order to dump out momentum for stabilizing a satellite since the early 1960s (White et al., 1961). However, if a magnetic field surrounding a satellite is uncontrolled, it will interact with the geomagnetic field, producing disturbance torque. This torque produced by the interaction between the magnetic torquer and geomagnetic field is described as Equation (8).

$$\vec{\tau}_{\text{mtq}} = \vec{M}_d \times \vec{B} \quad (8)$$

\vec{M}_d is the magnetic moment of the magnetic torquer and \vec{B} is the geomagnetic field. The unit of magnetic moment is $[A \cdot m^2]$ and the unit of magnetic field is $[Wb \cdot m^{-2}]$ or equally $[kg \cdot s^{-2} \cdot A^{-1}]$.

According to the IGRF (International Geomagnetic Reference Field) model, the ram vector and the geomagnetic field is unaligned, which will produce disturbance torque (Thébault et al., 2015). The disturbance torque is larger as the two vectors are misaligned and as the magnetic moment of the magnetic torquer is larger. Considering the large magnetic moment used in plasma drag constellation, the magnetic torquer will produce large disturbance torque not only resulting a misalignment in the ram vector, but could result unstable satellite attitude.

Figure 23 shows the disturbance torque for a magnetic torquer with 1 Am^2 magnetic moment in a 575 km sun synchronous orbit aligned with the ram vector. It can be seen that the disturbance torque is irregular and must be always expected throughout the orbit.

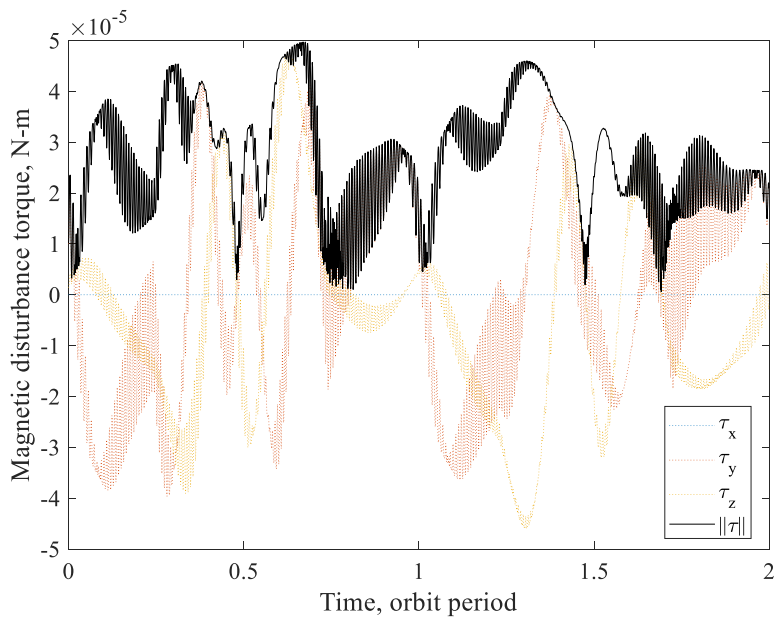


Figure 23 Disturbance torque of a 575 km sun synchronous orbit due to the interaction between magnetic actuator and geomagnetic field. The magnetic actuator is assumed to be aligned to the ram direction.

Chapter 3

Methodology

The principles of proposed plasma drag constellation deployment method and tools used in analyzing plasma drag constellation is introduced in this section. Two different tools are used in the study, one to investigate the plasma drag constellation deployment of relative spacecraft motion and another to investigate the combined dynamics of a spacecraft between attitude and orbit. The first part of the section discusses the plasma drag constellation concept. The second part of the section describes the analytical and numerical methods used in analyzing the orbit dynamics plasma drag constellation deployment. The last part of the section is dedicated in describing the numerical methods used in analyzing the combined attitude and orbit dynamics of a single spacecraft.

3.1. Plasma Drag Constellation Concept

Although many terminologies exist in describing a distributed satellite system (Poghosyan et al., 2016), this study focuses on regional inter-satellite distances, thus the proposed method is named ‘plasma drag constellation.’ The principle of plasma drag constellation deployment is similar to that of differential drag. Magnetic plasma drag force can be controlled by changing the magnetic dipole moment when using a magnetic torquer. In this case, the relative spacecraft motion can be controlled similar to the differential drag, however the magnetic moment of the magnetic actuator is varied instead of performing attitude maneuver. The specific orbital

energy decreases as the spacecraft is exposed to magnetic plasma drag, which as a result increases the mean motion of the orbit.

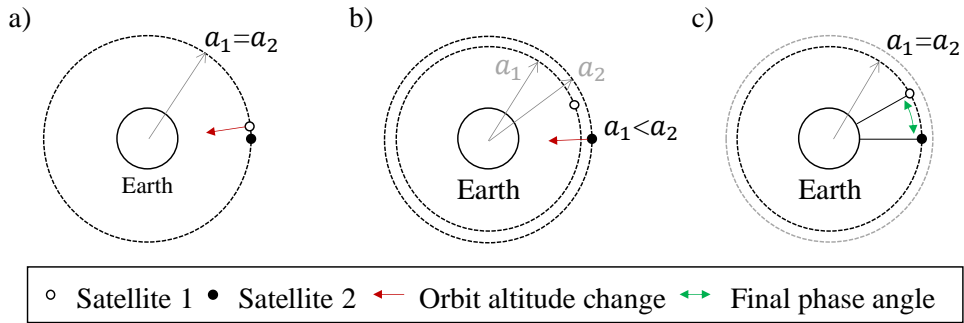


Figure 24 Conceptual drawing of plasma drag constellation. a) Satellite 1 uses plasma drag to lower the semi-major, increasing the mean motion. b) Satellite 2 uses plasma drag to match the mean motion as the desired phase angle is achieved. c) Satellite 1 and satellite 2 have achieved the desired phase angle with the same mean motion.

Consider two satellites, satellite 1 and satellite 2, at the same state, which must depart to deploy to a constellation. Neglecting external force other than magnetic plasma drag, as the mean motion of the two satellites are equal, the relative motion between the two satellites will stay constant. Actuation of magnetic actuator by satellite 1 will result an increase in the mean motion, resulting departure of satellite 1 respect to satellite 2. As the mean motion of satellite 1 is larger than satellite 2, the phase angle will increase as time passes. Actuation of magnetic actuator by satellite 2 as the desired phase angle is achieved will result the mean motion of the satellites to match, achieving the desired constellation. The conceptual drawing of plasma drag constellation is shown in Figure 24.

The advantages of plasma drag constellation over previous methods includes the following features: No additional components are required, no deployment is required, no propellant is required, no intense attitude maneuver is required, and continuous acceleration profile can be generated. Additional components in a CubeSat is burdensome as CubeSats are limited in resources such as mass, volume, and power. Any additional component is most likely to take up these resources. However, magnetic plasma drag uses a magnetic actuator, which is already board in a CubeSat, therefore no additional components are required. As the magnetic actuator is a fixed actuator, no deployment required, which decreases risk of deployment failure. Magnetic plasma constellation uses the interaction between magnetic actuator and space plasma, which the magnetic actuator uses electrical power generated from the solar panels and the space plasma is present in the Earth's ionosphere. Therefore, satellites do not require to board any propellant, reducing mass and increasing mission lifetime. The differential drag force can be generated by controlling the magnetic moment of the magnetic actuators, therefore attitude maneuver is not required for varying the differential drag, and furthermore the differential drag profile is continuous.

A comparison between atmospheric drag and magnetic plasma drag is shown in Figure 25. It can be seen that magnetic plasma drag is within an order range of atmospheric drag, which has successfully flown in CubeSat missions (Foster et al., 2016). Comparing differential drag using atmospheric drag and magnetic plasma drag, no attitude variations are required in changing the differential drag and furthermore continuous differential drag profile can be achieved. These sets of advantages make plasma drag constellation a promising method for CubeSats. The following sections introduce the methods and tools used in performing analyses on plasma drag constellation.

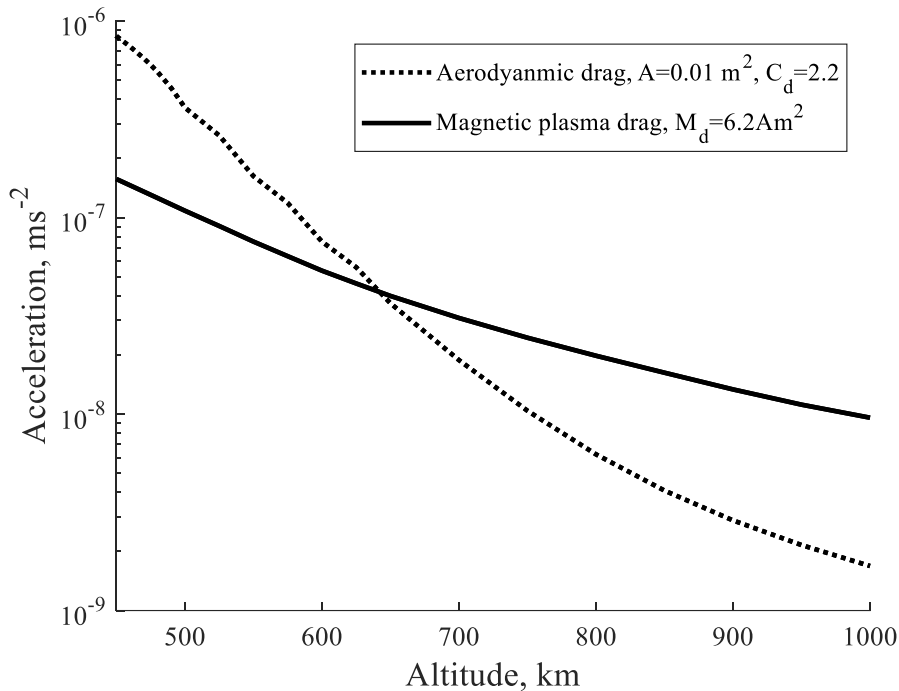


Figure 25 Comparison between atmospheric drag and magnetic plasma drag in low Earth orbit. Simplified Jacchia77 model with exospheric temperature of 1000 K is used for the atmospheric drag, and simplified IRI2012 model is used for the magnetic plasma drag.

3.2. Analytical Method

In order to perform an elementary analysis on plasma drag constellation time, a one-dimensional problem is formulated. The elementary analysis simplified the general orbit in order to obtain an analytical solution for preliminary constellation design analysis.

In the elementary analysis, we consider a two-satellite circular orbit plasma drag constellation as shown in Figure 24.

The two satellites in a constellation can be modeled by using relative phase angle and its rate.

Considering only the tangential specific force, F_T , the rate of change of semi-major axis over time due to external force (Bate et al., 1971) is given as Equation (9), where a , e , n , and r represent semi-major, eccentricity, mean motion, and radial distance respectively.

$$\frac{da}{dt} = \frac{2a\sqrt{1-e^2}}{nr} F_T \quad (9)$$

If we assume that the orbit remains circular ($e = 0, r = a$), Equation (9) becomes simplified to Equation (10).

$$\begin{aligned} \frac{da}{dt} &= 2 \sqrt{\frac{a^3}{\mu}} F_T \\ n &= \sqrt{\frac{\mu}{a^3}} \end{aligned} \quad (10)$$

Taking the time derivative of the orbit angular speed and applying the chain rule, the relationship between angular acceleration and tangential specific force is retrieved as shown in Equation (11).

$$\begin{aligned} \frac{d\omega}{dt} &= \frac{d\omega}{da} \frac{da}{dt} = \frac{d\left(\sqrt{\frac{\mu}{a^3}}\right)}{da} \left(2 \sqrt{\frac{a^3}{\mu}} F_T\right) = -3 \frac{F_T}{a} \\ \omega &= \sqrt{\frac{\mu}{a^3}} \end{aligned} \quad (11)$$

For the analytical study, if we assume that the initial and final semi-major is the same during the plasma drag actuation, the phase angle and its rate at an arbitrary time can be acquired by integrating Equation (11). Equation (12) shows the phase angle and its rate at an arbitrary time, τ , with the subscripts denoting time.

$$\begin{aligned}\omega_\tau &= \omega_0 - 3 \frac{F_T}{a} \tau \\ \theta_\tau &= \theta_0 + \omega_0 \tau - \frac{3 F_T}{2 a} \tau^2\end{aligned}\tag{12}$$

Defining the transition time up to when Satellite 1 accelerates as t_t , then the phase angle and phase angle rate can be obtained by integrating Equation (13). The subscripts in the equation describes the state of the satellite and the time.

$$\begin{aligned}\omega_{1,t_t} &= \omega_{1,0} - 3 \frac{F_T}{a} t_t \\ \omega_{2,t_t} &= \omega_{2,0} \\ \theta_{1,t_t} &= \theta_{1,0} + \omega_{1,0} t_t - \frac{3 F_T}{2 a} t_t^2 \\ \theta_{2,t_t} &= \theta_{2,0} + \omega_{2,0} t_t\end{aligned}\tag{13}$$

The acceleration term is included only in the states related to Satellite 1, because only Satellite 1 is accelerating up until t_t as shown in Figure 24a.

Now defining the deployment time when the constellation is fully deployed as t_d , Satellite 2 accelerates between t_t and t_d whereas Satellite 1 is coasting. Then, the satellite states can be expressed as Equation (14).

$$\begin{aligned}
\omega_{1,t_d} &= \omega_{1,t_t} \\
\omega_{2,t_d} &= \omega_{2,t_t} - 3 \frac{F_T}{a} (t_d - t_t) \\
\theta_{1,t_d} &= \theta_{1,t_t} + \omega_{1,t_t} (t_d - t_t) \\
\theta_{2,t_d} &= \theta_{2,t_t} + \omega_{2,t_t} (t_d - t_t) - \frac{3 F_T}{2 a} (t_d - t_t)^2
\end{aligned} \tag{14}$$

The acceleration term is present only in the states of Satellite 2, as Satellite 1 is coasting, as shown in Figure 24b.

Considering the constellation deployment sequence as shown in Figure 24, the boundary conditions at the initial and final state of the satellites are given as Equation (15).

$$\begin{aligned}
\theta_{1,0} &= \theta_{2,0} \\
\omega_{1,0} &= \omega_{2,0} \\
\omega_{1,t_d} &= \omega_{2,t_d}
\end{aligned} \tag{15}$$

Substituting Equation (15) to Equation (13) and (14), the relationship between t_d and t_t can be obtained as Equation (16).

$$t_d = 2t_t \tag{16}$$

Defining the phase angle difference between two satellites as $\delta\theta = \theta_1 - \theta_2$, the phase angle difference, the phase angle difference at deployment time can be obtained as Equation (17).

$$\delta\theta_d = \theta_{1,t_d} - \theta_{2,t_d} = -3\frac{F_T}{a}t_d^2 \quad (17)$$

Substituting Equation (16) to Equation (17) and rearranging for t_d , the deployment time for a desired phase angle difference can be obtained as Equation (18). The sign inside the square root of the equation is due to the negative F_T , as F_T acts counter ram direction for plasma drag force.

$$t_d = 2\sqrt{-\frac{a}{3F_T}\delta\theta_d} \quad (18)$$

For satellites with same physical properties, Equation (18) can be expressed in terms of magnetic moment, M_d , as shown in Equation (19). C is an orbit averaged constant, which is obtained by substituting Equation (6) for F_T .

$$t_d = 2\sqrt{-\frac{a}{3CM_d}\delta\theta_d} \quad (19)$$

$$C = \frac{F_T}{M_d} = \frac{F_{\text{plasma}}}{mM_d} = \frac{1}{m} \frac{1}{M_{ds}} \frac{\rho_{\text{plasma}}}{\rho_s} \frac{V^2}{V_s^2} F_s$$

Example values of orbit averaged plasma drag force required for obtaining C is given in Table 7.

Ion number density, ρ_{plasma} , can be acquired using the simplified IRI model introduced in the previous section and the relative plasma speed can be obtained using the circular orbital speed of the satellite given in Equation (20).

$$V = \sqrt{\frac{\mu}{r}} \quad (20)$$

Table 7 Example values of ρ , V and corresponding plasma drag force for $M_d = 10 \text{ Am}^2$. Ion number density and plasma drag force is averaged about a single orbit.

Orbit altitude	Ion number density, ρ_{plasma}	Relative plasma speed, V	Plasma drag force
500 km	$2.0887 \times 10^{11} \text{ m}^{-3}$	7612.6 ms^{-1}	$172.4 \times 10^{-9} \text{ N}$
600 km	$1.0733 \times 10^{11} \text{ m}^{-3}$	7557.9 ms^{-1}	$87.3 \times 10^{-9} \text{ N}$
700 km	$0.6221 \times 10^{11} \text{ m}^{-3}$	7504.3 ms^{-1}	$49.9 \times 10^{-9} \text{ N}$
800 km	$0.3988 \times 10^{11} \text{ m}^{-3}$	7451.8 ms^{-1}	$31.5 \times 10^{-9} \text{ N}$
900 km	$0.2762 \times 10^{11} \text{ m}^{-3}$	7400.5 ms^{-1}	$21.5 \times 10^{-9} \text{ N}$
1000 km	$0.2030 \times 10^{11} \text{ m}^{-3}$	7350.1 ms^{-1}	$15.6 \times 10^{-9} \text{ N}$

3.3. Numerical Method

In the previous section, an analytical solution was derived from circular and non-decaying orbit assumptions. Due to the assumptions, only a coarse estimation of the plasma drag constellation deployment time is possible and thus it is difficult to assess the detailed feasibility of plasma drag constellation on nanosatellites. Therefore, numerical simulations of plasma drag constellation are carried out in order to perform parametric studies on the parameters. This section describes the in-house simulator and the plasma drag constellation control algorithm used during the numerical analysis.

3.3.1. Constellation Deployment Simulator

The constellation deployment simulator is developed in order to simulate the plasma drag constellation deployment of the satellites in a constellation. The orbit dynamics of the satellites are solved numerically together with an embedded plasma drag controller for each of the satellites in order to achieve plasma drag constellation. The orbit dynamics, relative motion of the satellites, and the controller used in the constellation deployment simulator is described in detail.

3.3.1.1. Orbit Dynamics

An in-house simulator is used in order to perform a detailed assessment of various parameters on the feasibility of plasma drag constellation. Numerical model of the orbit is implemented, which is propagated using the fourth order Runge-Kutta integrator. Cowell's method is used with plasma drag and atmospheric drag considered as external force acting on the satellite orbit dynamics. Other perturbations such as geopotential, solar radiation pressure, or third body is neglected as we are interested on assessing the tangential specific force. The dynamic model of the orbit is expressed in Equation (21).

$$\ddot{\vec{r}} = -\frac{\mu}{|\vec{r}|^3}\vec{r} + \ddot{\vec{r}}_{\text{plasma}} + \ddot{\vec{r}}_{\text{atmosphere}} \quad (21)$$

In the dynamics model of Equation (21), plasma drag can be acquired using Equation (6) and atmosphere drag can be acquired using Equation (22).

$$\ddot{\vec{r}}_{\text{atmosphere}} = -\frac{1}{2} C_D \frac{A_{\text{cross}}}{m} \rho_{\text{atmosphere}} \|\vec{v}_r\|^2 \frac{\vec{v}_r}{\|\vec{v}_r\|} \quad (22)$$

C_D is a non-dimensional drag coefficient of the nanosatellite set to 2.2, A_{cross} is the cross-sectional area of the satellite set to 0.01 m^2 , \vec{v}_r is the satellite velocity vector, and $\rho_{\text{atmosphere}}$ is the atmospheric density. Similar to the IRI model, using an atmospheric model either requires a large table for atmospheric data or iterative calculation above the standard atmosphere.

In order to reduce the computational burden, the atmosphere density is sampled as a small table, which is then linearly interpolated. Jacchia 1977 model with exospheric temperature of 1000 K is used as the reference density model. A comparison between the Jacchia 1977 model and the simplified atmosphere model is shown in Figure 26.

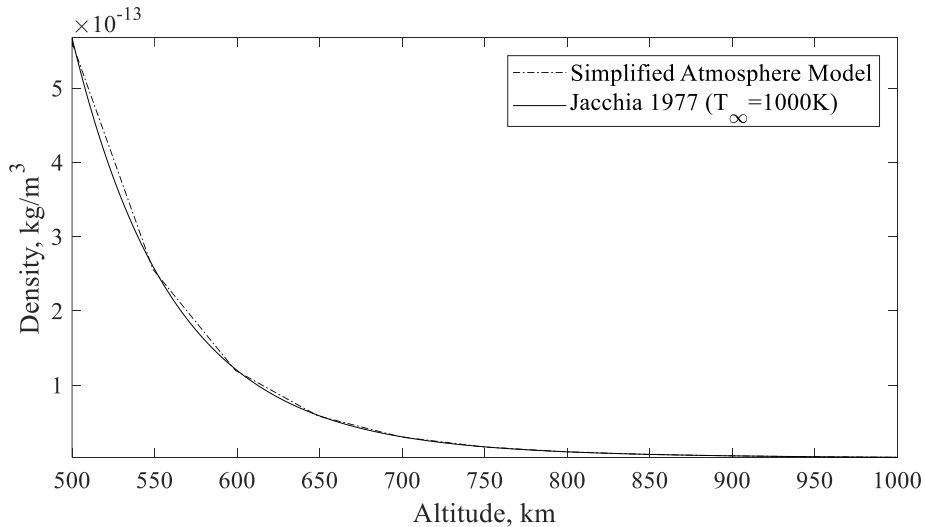


Figure 26 Comparison of simplified atmosphere model with the Jacchia 1977 model. The exospheric temperature of the Jacchia 1977 model is set to 1000 K.

Throughout the numerical analysis, the satellite attitude is assumed such that the long axis is aligned with the ram direction, thus the cross-sectional area, plasma velocity, and magnetic moment remains as a constant. An overview of the in-house orbit simulator used in Table 8.

Table 8 Overview of the in-house orbit simulator

Parameter	Method/model
Simulation method	Cowell's method
External force	Plasma drag, atmospheric drag
Integration scheme	Fourth order Runge-Kutta (dt = 20 s)
Atmospheric model	Simplified atmosphere model
Plasma model	Simplified IRI model
Satellite attitude	Long axis aligned with ram direction

3.3.1.2. Dynamic Model of Satellite Relative Motion

In previous studies on distributed satellite systems, system was modeled through linearization derived from close-range assumptions (Bae and Kim, 2013; Capó-Lugo and Bainum, 2009). However, the system non-linearity error of the model will increase as the inter-satellite distance of the distributed satellite system increases, therefore Hill-Clohessy-Wiltshire equations cannot be used. In order to overcome such problem, the distributed satellite system state is modeled based on phase difference, θ , and its rate, $\dot{\theta}$, instead of distance, as given in Equation (23).

$$\begin{aligned}\theta_{ij} &= \theta_i - \theta_j \\ \dot{\theta}_{ij} &= \dot{\theta}_i - \dot{\theta}_j\end{aligned}\tag{23}$$

The subscripts i and j in the phase and its rate indicate the state of each of the specific satellite, whereas ij indicate the relative state between the two satellites.

Then, assuming a non-perturbed circular orbit, the phase rate, which is equal to the angular velocity of the orbit, ω , is described using the mean motion, given as Equation (24).

$$\dot{\theta} = \omega = \sqrt{\frac{\mu}{a^3}} \quad (24)$$

Then the phase acceleration, which is equal to the angular acceleration of the orbit can be obtained by taking the time derivative of the angular velocity of the orbit, given as Equation (25).

$$\ddot{\theta} = \dot{\omega} = \frac{\partial \omega}{\partial t} = -\frac{3}{2} \sqrt{\frac{\mu}{a^5}} \frac{\partial a}{\partial t} \quad (25)$$

In Equation (25), the time derivative term of the semi-major axis is required. As the interest is control of the magnetic torquer in the distributed satellite system deployment, change of semi-major due to the plasma drag is considered. In this study, an analytical solution of plasma drag is used (Matsuzawa, 2017), which takes orbit energy loss after a single revolution, introduced in the Appendix. Using the analytical solution, the change in the semi-major axis over an orbit is given as Equation (26).

$$\Delta a_{\text{plasma}} = -4\pi k a^2 \exp\left(-\frac{a}{G_0}\right) I_0(A_0) \quad (26)$$

$$k = \frac{M_d F_s}{m M_{as} \rho_s V_s^2} \rho_0 \exp\left(\frac{r_0}{G_0}\right)$$

In Equation (26), a , G_0 , and $I_n(x)$ represents semi-major axis, height scale factor, and modified Bessel function of the first kind of n respectively.

Then, the averaged change rate of semi-major axis over orbit period T can be obtained as in Equation (27).

$$\frac{\partial a}{\partial t} \cong \frac{\Delta a_{\text{plasma}}}{T} = \frac{\Delta a_{\text{plasma}}}{2\pi} \sqrt{\frac{\mu}{a^3}} \quad (27)$$

$$T = \frac{2\pi}{\sqrt{\mu}} a^{\frac{3}{2}}$$

Substituting Equation (27) in to Equation (25), the phase acceleration can be expressed in terms of the change in semi-major axis due to plasma drag, as in Equation (28).

$$\ddot{\theta} = -\frac{3}{2} \sqrt{\frac{\mu}{a^5}} \frac{\partial a}{\partial t} = -\frac{3}{2} \sqrt{\frac{\mu}{a^5}} \left(\frac{\Delta a_{\text{plasma}}}{2\pi} \sqrt{\frac{\mu}{a^3}} \right) = -\frac{3}{4\pi} \frac{\mu}{a^4} \Delta a_{\text{plasma}} \quad (28)$$

Regarding the magnetic moment of a magnetic torquer, if the magnetic torquer is assumed to be an electromagnetic coil, which the magnetic moment is linear to the input current. Then the magnetic moment can be expressed by the control input, u , and the maximum magnetic moment of the magnetic torquer, \bar{M}_d , as in Equation (29). In an actual satellite system, the magnetic torquer is controlled by duty-cycling the PWM (Pulse-Width Modulation) signal in to the H-bridge driver, which results in current control.

$$M_d = \bar{M}_d u \quad (|u| \leq 1) \quad (29)$$

Substituting \bar{M}_d for M_d in Equation (26), the control is given as Equation (30) and Equation (31).

$$\Delta\bar{a}_{\text{plasma}} = -4\pi\bar{k}a^2 \exp\left(-\frac{a}{G_0}\right) I_0(A_0) \quad (30)$$

$$\bar{k} = \frac{\bar{M}_d F_s}{mM_{ds}\rho_s V_s^2} \rho_0 \exp\left(\frac{r_0}{G_0}\right)$$

$$\Delta a_{\text{plasma}} = \Delta\bar{a}_{\text{plasma}} u \quad (|u| \leq 1) \quad (31)$$

Then, using the phase and phase rate as the state of the distributed satellite system, the linear state-space of the dynamic model can be expressed as Equation (32). The subscripts i and j represent the

$$\begin{aligned} \dot{X}_{ij} &= A_{ij}X_{ij} + B_{ij}U_{ij} \\ X_{ij} &= \begin{bmatrix} \theta_{ij} \\ \dot{\theta}_{ij} \end{bmatrix}, U_{ij} = \begin{bmatrix} \Delta\bar{a}_{\text{plasma},i}u_i \\ \Delta\bar{a}_{\text{plasma},j}u_j \end{bmatrix} \\ A_{ij} &= \begin{bmatrix} 0 & 1 \\ 0 & 0 \end{bmatrix}, B_{ij} = \begin{bmatrix} 0 & 0 \\ B_i & -B_j \end{bmatrix} \\ B_i &= -\frac{3}{4\pi} \frac{\mu}{a_i^4}, B_j = -\frac{3}{4\pi} \frac{\mu}{a_j^4} \end{aligned} \quad (32)$$

The system described in Equation (32) is controllable as the controllability matrix is full rank as shown in Equation (33).

$$\text{rank}(R) = \text{rank}[B \quad AB] = \text{rank} \begin{bmatrix} 0 & 0 & B_i & -B_j \\ B_i & -B_j & 0 & 0 \end{bmatrix} = 2 \quad (33)$$

3.3.1.3. Constellation deployment controller

In this study, the objective is to examine the feasibility of the plasma drag constellation deployment, thus the critical deployment time is the interest. Depending on the control, the phase could overshoot, which does not show the deployment characteristics described in Figure 24 or the elementary analysis in Section 2.3.1. Thus the critically damped control case is considered as deployment time, which the deployment characteristics describe Figure 24 or the elementary analysis. In the numerical analysis, LQR (Linear Quadratic Regulator) is used, as the critical deployment time can be acquired easily by tuning the cost function matrix.

Defining the state X , and the control input U , the quadratic cost function, J , of an LQR is defined as Equation (34).

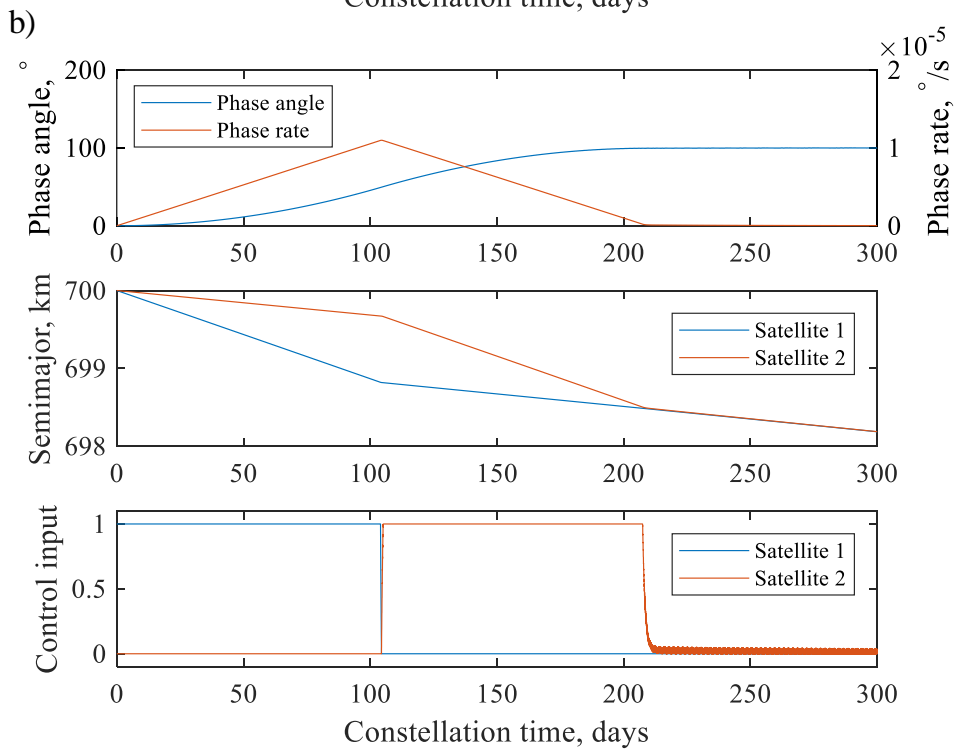
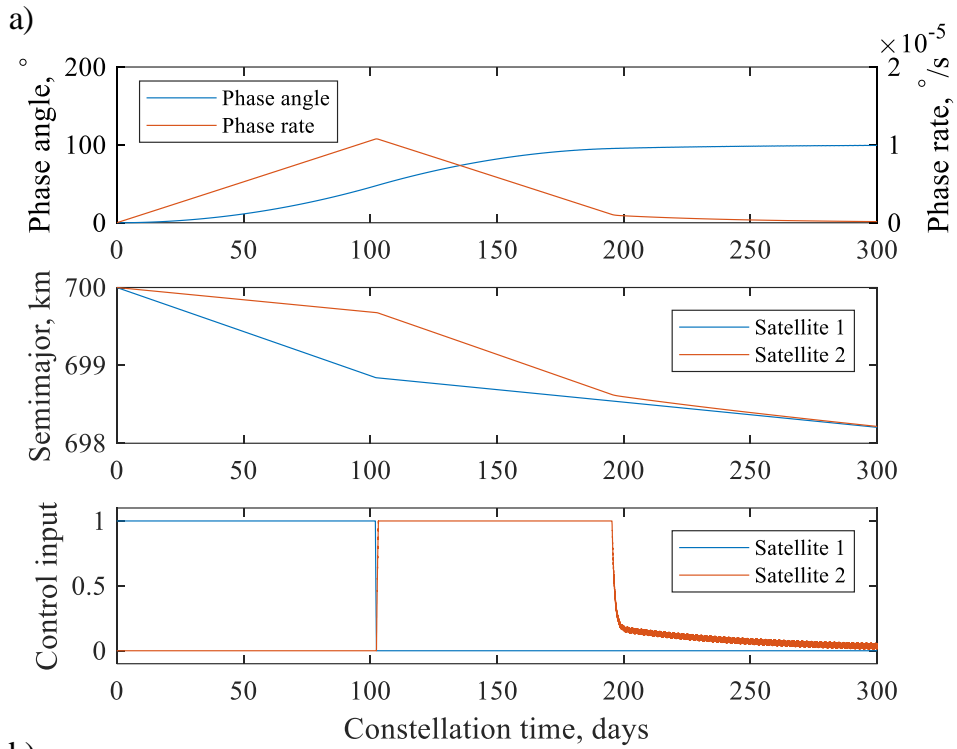
$$J = \frac{1}{2} \int_0^{\infty} (X^T Q X + U^T R U) dt \quad (34)$$

The objective of LQR is to minimize the cost function J over infinite time horizon with Q and R each being weighing matrices for the state deviation and the control effort respectively. Examining Equation (34), for a same cost, if Q is large compared to R the control effort will be larger, whereas if Q is small compared to R the control effort will be smaller. In this study, the default values of Q and R are defined as Equation (35), where θ_d is the desired phase angle, and ρ_R is a scaling factor for R matrix.

$$Q = \begin{bmatrix} (0.02 \times \theta_d)^{-2} & 0 \\ 0 & 1^{10} \end{bmatrix}, R = \rho_R \begin{bmatrix} 1 & 0 \\ 0 & 1 \end{bmatrix} \quad (35)$$

The diagonal values of Q matrix is set such that the corresponding diagonal terms of $X^T Q X$ becomes similar at its regulated value. In this study, the settling time is considered to be when 98% of the desired phase angle has been achieved, while the phase rate converges to zero. In case of the diagonal values of R matrix, there are no preferences in the actuation of the two satellites, therefore R is set as an identity matrix.

Before performing parametric study on plasma drag constellation, the effect and importance of R matrix must be first considered. Depending on the R matrix, the damping characteristics will change, which must be carefully selected for the plasma drag constellation to be described by the numerical analysis results. As discussed earlier, ρ_R value in the R matrix is varied in changing the gain while the Q matrix is fixed. Larger ρ_R value will penalize control effort, which implies that large ρ_R will result an overdamped system property whereas small ρ_R will result an underdamped system property. In the LQR, the states are defined as phase angle and phase rate, thus an underdamped system property will result an overshoot in the states, meaning the excess control. Therefore, in order to acquire constellation time as described in the elementary analysis in Section 2.1.2, critically damped case must be considered. Figure 27 shows the overdamped, critically damped, and underdamped system characteristics depending on ρ_R .



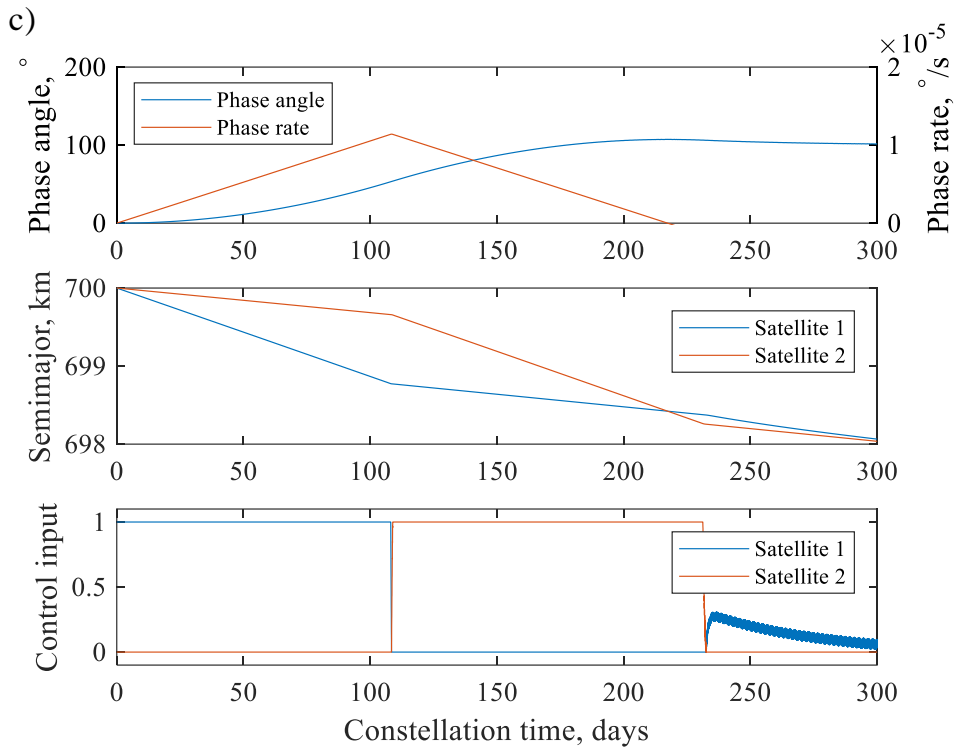


Figure 27 Damping characteristics of plasma drag constellation depending on ρ_R . $M_d = 10$, $m = 1$, and a) $\rho_R = 1 \times 10^{-1}$, b) $\rho_R = 8 \times 10^{-2}$, and c) $\rho_R = 5 \times 10^{-2}$ showing overdamped, near-critically damped, and underdamped system characteristics. The subgraph on the top shows the states (phase angle and phase angle rate), subgraph on the middle shows the orbit altitude, and the subgraph on the bottom shows the control input.

It can be seen in Figure 27b that satellite 1 accelerates until the transition time, and satellite 2 accelerated from transition time until the deployment time as in the elementary analysis.

3.3.2. Attitude Simulator

The previously introduced plasma drag constellation simulator neglects the attitude dynamics as its purpose is to perform parametric study on the plasma drag constellation. However, external torque will be applied on a spacecraft using magnetic plasma drag, resulting change in the satellite attitude. The change in satellite attitude is critical in magnetic plasma drag, as magnetic moment misalignment with the ram vector results a loss in the drag force as previously explained in Section 2.2. The attitude and orbit dynamics, the controller, and calculation method of the loss in magnetic plasma drag is introduced in detail.

3.3.2.1. Attitude and Orbit Dynamics

In order to investigate the dynamics of satellite attitude due to disturbance torque when the magnetic torquer is actuated, a numerical simulation on attitude disturbance considering a large magnetic torquer is carried out. The attitude dynamics is expressed in Equation (36) and Equation (37), considering disturbance torque due to magnetic torquer.

$\vec{\omega}_{ib}^b$ is the angular velocity of the satellite with respect to the inertial frame expressed in body coordinates, J is the moment of inertia of the satellite, $\vec{\tau}_{mtq}^b$ is the disturbance torque due to the magnetic torquer, $\vec{M}_{d,p}^b$ is the magnetic moment of the primary magnetic torquer, and \vec{B}^b is the geomagnetic field expressed in body coordinates.

$$J\dot{\vec{\omega}}_{ib}^b = -\vec{\omega}_{ib}^b \times (J\vec{\omega}_{ib}^b) + \vec{\tau}_{mtq}^b \quad (36)$$

$$\begin{aligned}
\vec{\tau}_{\text{mtq}}^b &= \vec{M}_{d,p}^b \times \vec{B}^b \\
&= \begin{bmatrix} M_{d,px} & 0 & 0 \\ 0 & M_{d,py} & 0 \\ 0 & 0 & M_{d,pz} \end{bmatrix} \begin{bmatrix} u_x \\ u_y \\ u_z \end{bmatrix} \times \vec{B}^b \\
&= \begin{bmatrix} M_{d,px} u_x \\ 0 \\ 0 \end{bmatrix} \times \vec{B}^b \quad (u_x = 1)
\end{aligned} \tag{37}$$

All external forces including plasma drag force is neglected in the orbit dynamics, as the interest is in the attitude of the spacecraft. Nevertheless, basic orbit dynamic shown in Equation (38) is considered in order to implement the change in geomagnetic field as the satellite orbits around the Earth.

$$\ddot{\vec{r}} = -\frac{\mu}{|\vec{r}|^3} \vec{r} \tag{38}$$

3.3.2.2. High-Frequency Polarity Switching PD Controller

The geomagnetic torque due to magnetic actuator was introduced in Section 2.2. In order to maintain the magnetic moment aligned with the ram vector, geomagnetic torque must be regulated. Inspecting Figure 22, if the geomagnetic field is assumed to be frozen, instantaneously switching the polarity of the magnetic moment will produce equal but opposite torque cancelling out geomagnetic torque. The polarity switching of the magnetic actuator is described in Equation (39).

$$\begin{aligned}
\vec{\tau}_{\text{mtq},t} &= \vec{M}_d \times \vec{B} \\
\vec{\tau}_{\text{mtq},t+\Delta t} &= (-\vec{M}_d) \times (\vec{B} + \Delta\vec{B}) \\
&= (-\vec{M}_d \times \vec{B}) + (-\vec{M}_d \times \Delta\vec{B})
\end{aligned} \tag{39}$$

In Equation (39), the polarity switching is described by the negative sign of the magnetic moment, and the change in magnetic field during the switching is expressed by $\Delta\vec{B}$. For a very short switching period, $\Delta\vec{B}$ would approach to zero, which then the disturbance torque would approximately cancel out.

While the polarity switching minimizes the geomagnetic torque, an active controller is required in order to keep the magnetic torquer aligned with the ram vector. In this thesis, the high frequency polarity switching using the primary magnetic actuator is combined with the classical PD controller (Wie et al., 1989) using the auxiliary magnetic actuators to form a hybrid switching PD controller. The classical PD controller is given in Equation (40).

$$\begin{aligned}\vec{\tau}_{des} &= (-k_\omega J \omega_e - k_q J q_e) \\ \vec{M}_{des} &= -\frac{\vec{\tau}_{des} \times \vec{B}}{\|\vec{B}\|^2} \quad (|M_{des,i}| < M_{d,si})\end{aligned}\quad (40)$$

$\vec{\tau}_{des}$ is the desired torque, k_ω and k_q are PD gains, ω_e and q_e are state error, J is the moment of inertia of the spacecraft, \vec{M}_{des} is the desired magnetic moment, and \vec{B} is the geomagnetic field. Since the small magnetic torquers are used, $M_{d,si}$ is limited to 0.2 Am^2 . The hybrid switching PD controller is given in Equation (41).

$$\vec{M}_d = M_{d,px} [\sigma_{\text{freq}} \quad 0 \quad 0]^T + \vec{M}_{des} \quad (41)$$

σ_{freq} indicates a switching function, which the switching frequency is the frequency in the subscript.

3.3.2.3. Plasma Drag Force Loss Calculation

Using the high-frequency polarity switching PD controller, the pointing accuracy of the magnetic moment with the ram vector, and the transition in magnetic plasma drag due to polarity switching will affect the overall plasma drag force. A loss function is defined in this section, in order to compute the overall loss considering the two factors.

The magnetic plasma drag loss due to misalignment of magnetic moment with the ram vector, L_{align} , in Figure 21 is modeled using 6th order polynomial fit, as shown in Figure 28.

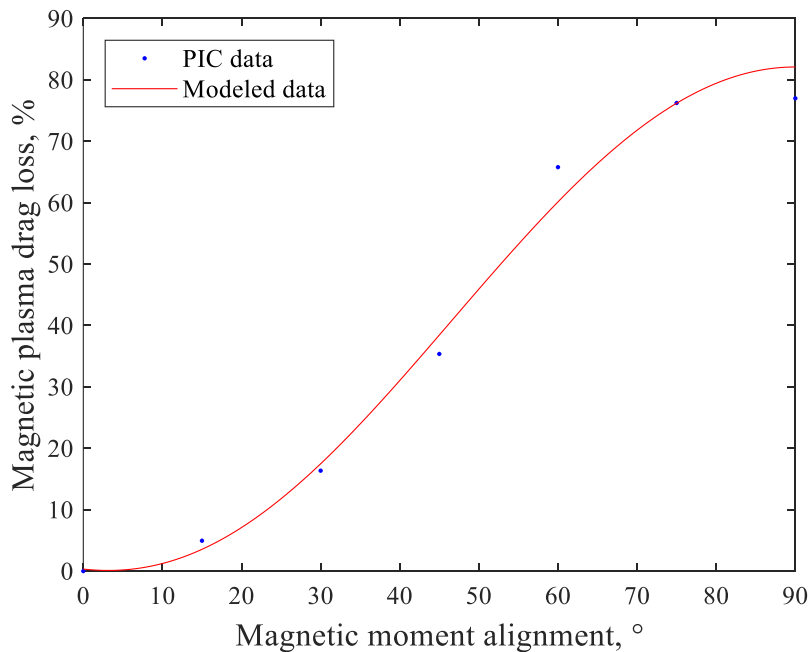


Figure 28 Polynomial fit of the magnetic plasma drag loss misalignment of magnetic moment with ram vector given in Figure 21.

The loss due to transition, L_{trans} , of magnetic plasma drag due to polarity switching is modeled as Equation (42).

$$L_{\text{trans}} = 1 - \frac{1}{P_{\text{switch}}} \int_0^{P_{\text{switch}}} \frac{F_{\text{plasma}}(\tau)}{\bar{F}_{\text{plasma}}} d\tau \quad (42)$$

Then, the overall loss of magnetic plasma drag, L_{total} , is given as Equation (43).

$$L_{\text{total}} = 1 - (1 - L_{\text{align}})(1 - L_{\text{trans}}) \quad (43)$$

Chapter 4

Plasma Drag Constellation

This chapter examines the plasma drag constellation introduced in Section 3.1. An analytical expression of plasma drag constellation was derived in Section 3.2.

4.1. General Aspects of Plasma Drag Constellation Time

According to the analytical solution of plasma drag constellation time given in Equation (19), the constellation deployment time is inversely proportional to the square root of the magnetic moment of the magnetic actuator, and proportional to square root of the desired phase angle and satellite mass. That is, in order to decrease the constellation deployment time, the magnetic actuator must be larger, or the desired phase angle must be limited to smaller angles or the satellite must be lighter. Figure 29 shows the relation between plasma drag constellation deployment time with the magnetic moment, desired phase angle, and the initial orbit altitude.

4.2. Parametric Study of Plasma Drag Constellation

The analytical solution was derived from circular and non-decaying orbit assumptions. Therefore, numerical simulations are carried out in order to validate the analytical solution.

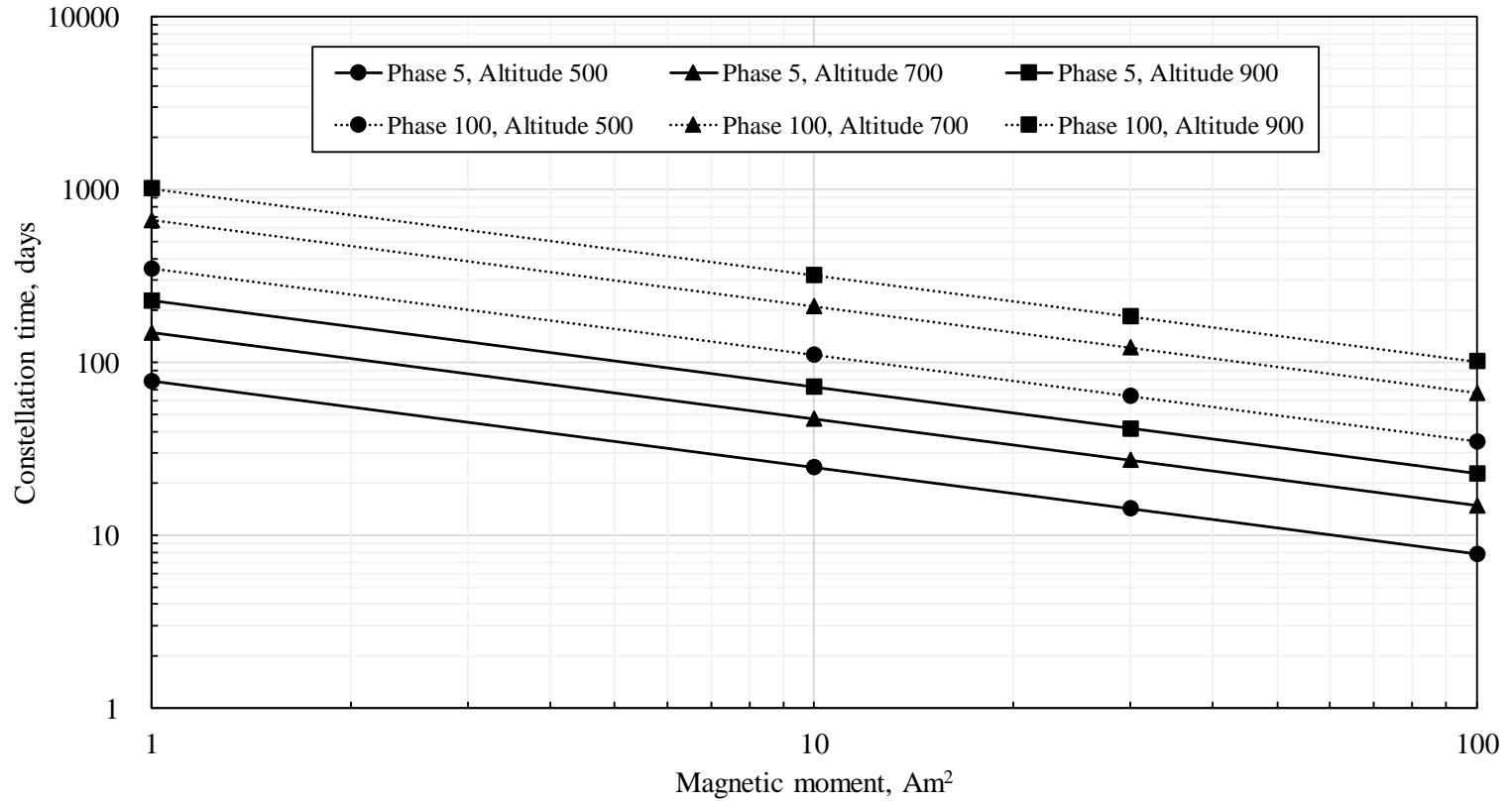


Figure 29 Analytical solution of plasma drag constellation time on magnetic moment for various orbit altitudes and desired phase angles ($m = 1$).

Furthermore, as part of the parametric study of plasma drag constellation, satellite mass, magnetic moment, desired phase angle, and initial orbit altitude were considered during the investigation. The parameters that were investigated are shown in Table 9.

Table 9 Investigated parameters on plasma drag constellation

Parameter	Value
Satellite mass	1, 3 kg
Magnetic moment	1, 10, 30, 100 Am ²
Desired phase angle	5, 100 degrees
Initial orbit altitude	500, 600, 700, 800, 900, 1000 km

The results of the numerical simulations are shown in Figure 30. The numerical results show the same tendency, which the deployment time is proportional to the square root of desired phase angle, and inversely proportional to the square root of magnetic moment. However, comparing the numerical results with the analytical solution, a small difference in deployment time can be seen. The difference is due to the non-decaying assumption in the elementary analysis, whereas the maximum plasma drag force increases as the orbit decays in the numerical simulation due to increasing plasma number density at lower altitudes. Furthermore, additional account of aerodynamic drag force in the numerical simulation plays a role as differential drag due to neutral density difference between the two satellites exist.

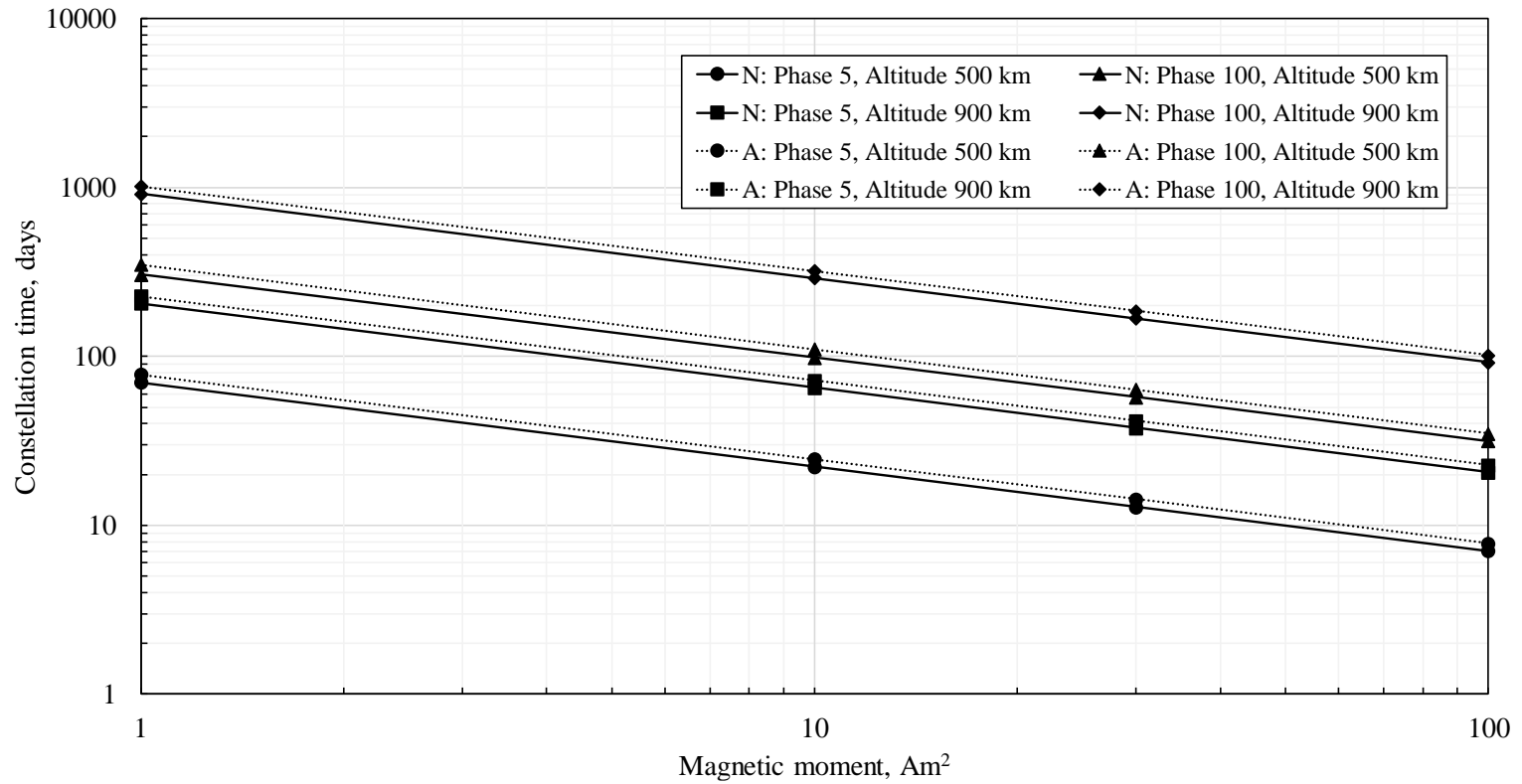


Figure 30 Comparison between analytical solution (A) and numerical simulation results (N) of plasma drag constellation, depending on phase angle, altitude and magnetic moment on deployment time ($m = 1$).

In order to validate the relation between satellite mass and deployment time, numerical simulations with satellite mass of 1 kg and 3 kg were performed. According to the numerical results, the deployment time ratio between 1 kg and 3 kg cases had a ratio of $\sqrt{3}$ as in Figure 31. The numerical results agree with the elementary analysis result, which the deployment time was proportional to the square root of satellite mass.

Lastly, numerical simulations were performed on different initial orbit altitudes. According to the elementary analysis, deployment time is related to the orbit altitude as both semi-major axis and plasma number density is related to orbit altitude. Figure 32 shows the numerical simulation results of deployment time depending on the orbit altitudes. It can be seen that the deployment time has an approximately linear relation with orbit altitude. The linear approximation of orbit altitude with deployment time shows a 5% error at low Earth orbit ranging from 500 km to 1000 km.

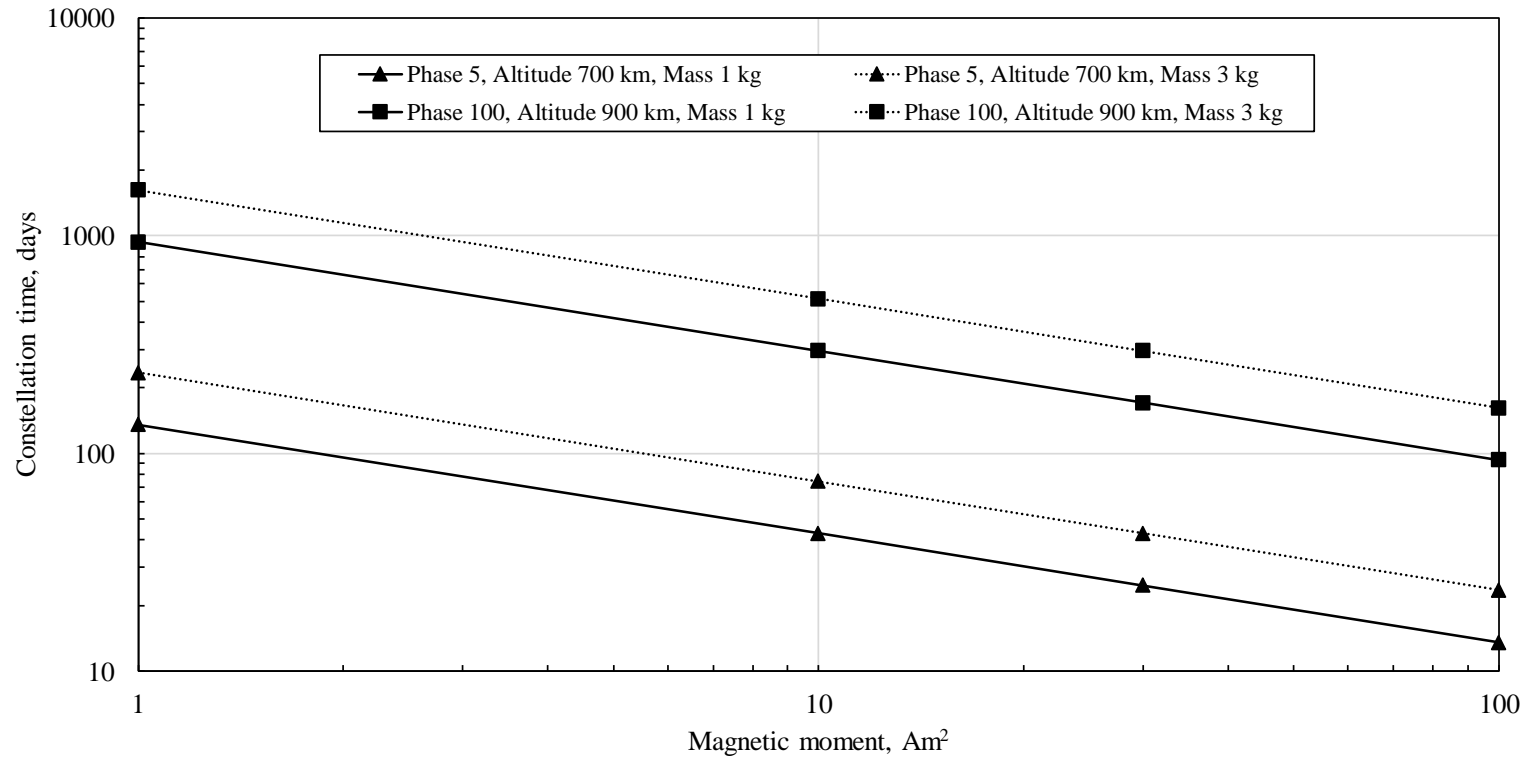


Figure 31 Plasma drag constellation numerical simulation results of deployment time depending on the mass of the satellites.

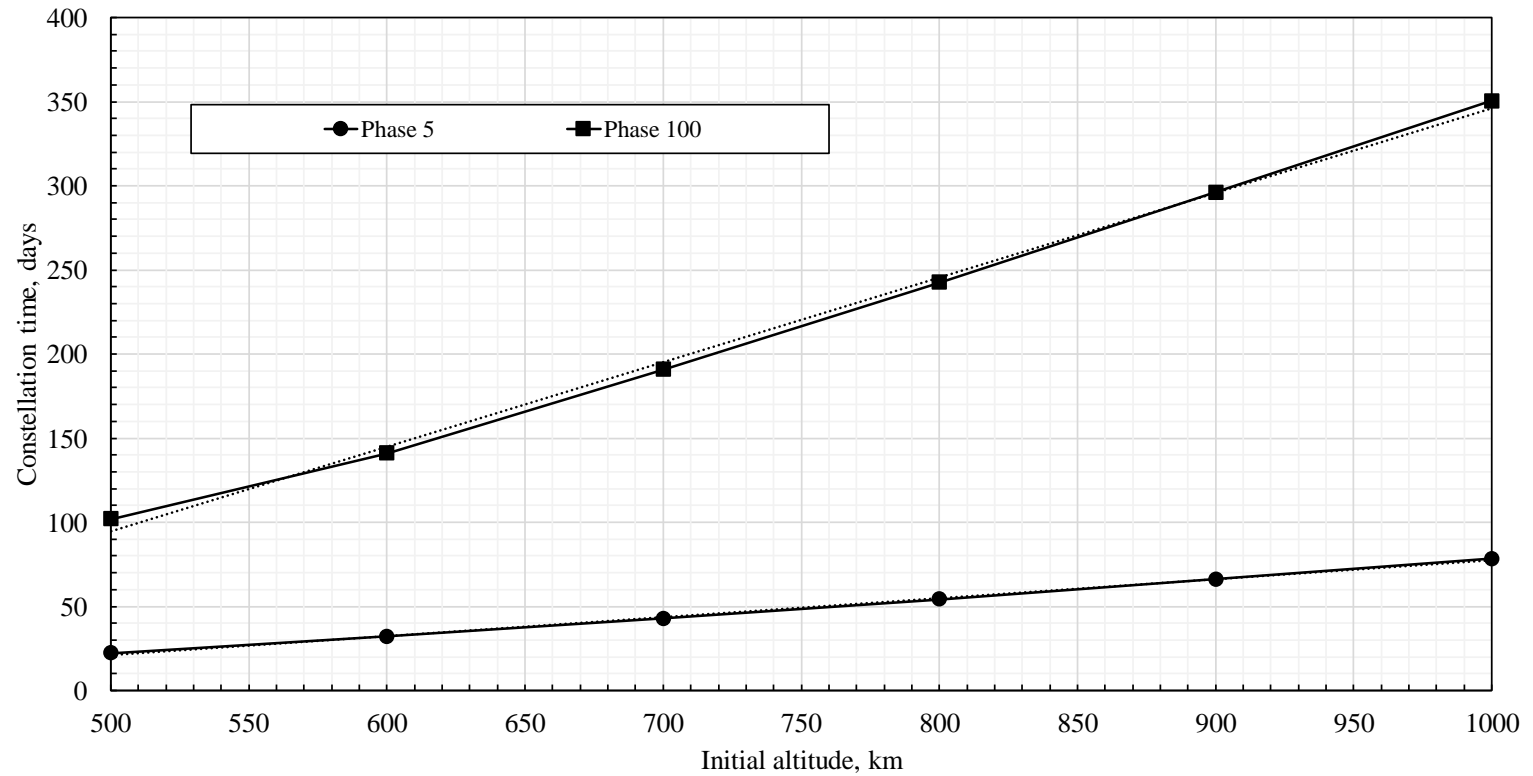


Figure 32 Plasma drag constellation numerical simulation results of deployment time depending on the orbit altitude of the satellites ($M_d = 10 \text{ Am}^2$ and $m = 1$).

Chapter 5

Plasma Drag Constellation Feasibility Analysis

In the previous chapter, analysis on the plasma drag constellation revealed important relationship between the design parameters and the constellation deployment time. Depending on the magnetic moment, satellite mass, desired phase angle and the orbit altitude, the constellation deployment time ranged from few tens of days up to few years. Ideally, a large magnetic actuator will reduce the constellation deployment time, however large magnetic moment requires large mass, volume, and power. Therefore, it is important to perform an analysis on the practical aspects of the system in order to assess the feasibility. This chapter is dedicated in finding the feasibility regarding the size of the magnetic actuator, and the constellation deployment time. In this study, nanosatellites ranging from 1 to 3 kg, which corresponds to CubeSats ranging from 1 to 3 U are considered as the target system.

5.1. Magnetic Moment of a Magnetic Actuator on a CubeSat

Limitation in the feasibility of plasma drag constellation on a CubeSat system is the large magnetic moment, which is related to mass and power. When considering an electrical-coil type magnetic torquer, the magnetic moment is proportional to current, number of windings, and cross-sectional area. Taking the basic properties and using the dimensional relations (Inamori et al., 2015a; Lee et al., 2005; Mehrjardi and Mirshams, 2010) given in Equation (44) the feasible maximum magnetic moment for a given mass and power can be calculated.

$$\begin{aligned}
 M &= \frac{r^3}{r_0^3} M_0 \\
 M_d &= \frac{r^{2.5}}{r_0^{2.5}} M_{d0} \\
 M_d &= \frac{I}{I_0} M_{d0} \\
 W &= \frac{I^2}{I_0^2} W_0
 \end{aligned}
 \tag{44}$$

$M_0, r_0, M_{d0}, I_0, W_0$ is the mass, core radius, magnetic moment, current, and power of the reference magnetic torquer respectively, and M, r, M_d, I, W is the mass, core radius, magnetic moment, current, and power of the target magnetic torquer respectively. The values of the reference magnetic torquer is given in Table 10.

Table 10 Parameters of the reference magnetic torquer (Lee et al., 2005).

Parameter	Value
Mass, M_0	5 kg
Magnetic moment, M_{d0}	186 Am ²
Power, W_0	< 3 W

Table 11 Parameters used in power margin estimation for 1 U CubeSat

Parameter	Value (per 1 U CubeSat)
Solar irradiance	1367 W/m ²
Solar cell area	60.36 cm ²
Solar cell efficiency	26.5% (EOL)
Total regulation efficiency	75%
Sunlight proportion in orbit	60%
Orbit average power margin	0.98 W

In the feasibility study, an arbitrary proportion of 50% of CubeSat resource is allocated for plasma drag constellation regarding mass and power. Available power is calculated based on 1U CubeSat as shown in Table 11.

Table 12 Magnetic moment limitations due to mass and power requirements for a CubeSat

Parameter	1U CubeSat	2U CubeSat	3U CubeSat
Mass	0.50 kg	1.00 kg	1.50 kg
Power	0.49 W	0.98 W	1.47 W
Magnetic moment	6.2 Am ²	15.9 Am ²	27.4 Am ²

Allocating 0.49 W and 0.5 kg per unit CubeSat as available resource, the maximum magnetic moment of the primary magnetic torquer can be acquired as in Table 12. Within 0.5 kg resource allocated for magnetic actuator, two small auxiliary magnetic actuators are considered, which are generally used for control along with the primary magnetic actuator. In this study, the magnetic moment of the two small magnetic actuators are fixed to 0.2 Am², which is a typical value of magnetic moment of commercially available CubeSat magnetic actuators.

The maximum magnetic moment of the magnetic torquer in Table 12 yields the lower bound of deployment time, which defines the minimum time required for the desired constellation deployment as a CubeSat cannot have a larger magnetic actuator.

5.2. Perturbation of Right Ascension of the Ascending Node

The upper bound of the deployment time is derived from along-track alignment between the satellites in a constellation, as the constellation will lose its mission

capability as a satellite drifts away, as shown in an example in Figure 33. The numerical simulations performed in the previous chapters does not take account of the variation of RAAN (right ascension of the ascending node) of the orbit, which affects the along-track misalignment, as only the tangential specific acceleration is considered. However, in reality, perturbation such as geopotential, solar radiation pressure, or third body effect has effect on RAAN.

According to variation of the classical orbital elements (Bate et al., 1971) in Equation (45), perpendicular force has effect on change in RAAN, which is the largest from the elements of geopotential.

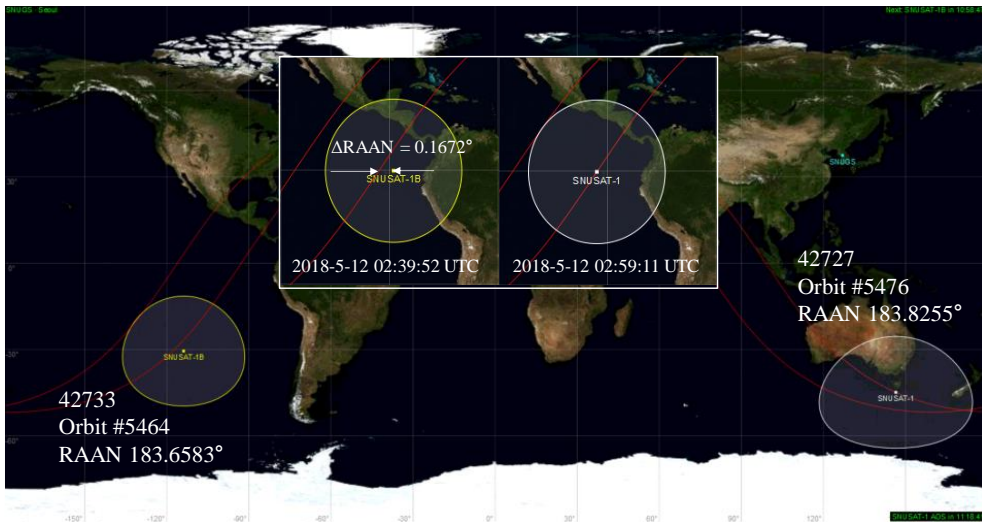


Figure 33 Satellite mission will be limited as the RAAN (right ascension of the ascending node) changes over time. Example shows the RAAN misalignment effect for SNUSAT-1 and SNUSAT-1b as it passes Central America.

In the equation, Ω is the RAAN, F_w is the perpendicular specific acceleration, r is the radial distance, u is the argument of latitude, n is the mean motion, a is the semi-major axis, e is eccentricity, and i is inclination.

$$\frac{d\Omega}{dt} = \frac{rF_w \sin u}{na^2\sqrt{1-e^2} \sin i} \quad (45)$$

In order to investigate the upper bound related to along-track alignment, a full numerical simulation on orbit dynamics were performed when two satellites have a 90-degree phase angle, to expose the satellites in different perturbing conditions. Additional perturbing forces that were considered are geopotential, third body due to moon and sun, and solar radiation pressure. In this study, the along-track alignment was considered to be in misalignment when the RAAN difference was larger than half the footprint angle of the satellite. Furthermore, a minimum 1-year mission lifetime after the constellation deployment was considered, therefore the allowable time for constellation deployment was set to be year shorter than the orbit plane collapse due to along-track misalignment. The constellation time upper bound results for low Earth orbits ranging 500 km to 1000 km are shown in Table 13.

Table 13 Constellation orbit plane lifetime and allowable deployment time

Initial orbit altitude	Half footprint angle	Time to orbit plane collapse	Allowable deployment time
500 km	20.3°	1.8 years (EOL)	292 days
600 km	21.8°	3.89 years	1055 days
700 km	23.1°	4.7 years	1351 days
800 km	24.2°	5.18 years	1526 days
900 km	25.2°	5.5 years	1643 days
1000 km	26.0°	5.79 years	1749 days

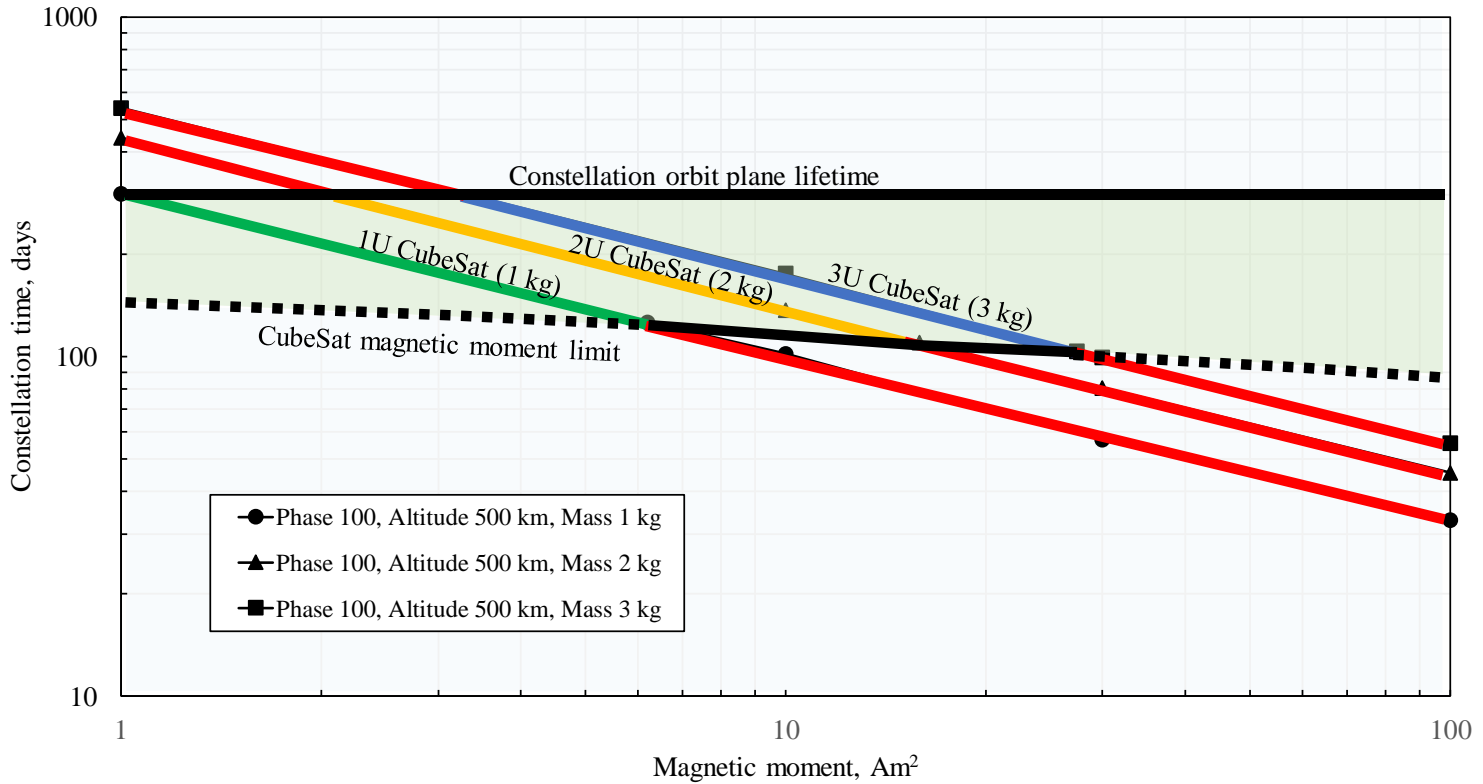


Figure 34 Plasma drag constellation feasibility diagram showing feasible configurations for 1~3 U CubeSats at 500 km orbit. Green curve shows 1 U feasible limit, yellow curve shows 2 U feasible limit, and blue curve shows 3 U feasible limit along a specific condition.

Combining the lower and upper bound of the feasibility study, a feasibility diagram of CubeSat plasma drag constellation can be presented as Figure 34. Figure 34 shows an example of plasma drag constellation at a 500 km orbit altitude, with lower bound set from magnetic moment limit and upper bound set from orbit plane lifetime. Magnetic moment requirement of the magnetic torquer can be selected regarding target deployment time, or available resources for the magnetic torquer.

5.3. Example of a four-CubeSat plasma drag constellation

As an example of plasma drag constellation CubeSat with four CubeSat equally distributed along-track, a numerical simulation is performed as the parameters given in Table 14.

Table 14 Plasma drag constellation configuration example

Constellation parameter	Value
Number of CubeSats in constellation	4
Desired phase angle between satellites	90 degrees
Orbit altitude	500 km
CubeSat platform	1 U (1 kg)
Magnetic moment	6.2/0.2/0.2 Am ²

As previously introduced, the large magnetic torquer is used as plasma drag constellation actuation, whereas the small magnetic actuators are used for momentum dumping. The linear state-space representation is modified to configure four CubeSats in the constellation, as shown in Equation (46).

$$X = \begin{bmatrix} \theta_{12} \\ \theta_{23} \\ \theta_{34} \\ \dot{\theta}_{12} \\ \dot{\theta}_{23} \\ \dot{\theta}_{34} \end{bmatrix}, U = \begin{bmatrix} u_1 \\ u_2 \\ u_3 \\ u_4 \end{bmatrix} \quad (46)$$

$$A = \begin{bmatrix} 0 & 0 & 0 & 1 & 0 & 0 \\ 0 & 0 & 0 & 0 & 1 & 0 \\ 0 & 0 & 0 & 0 & 0 & 1 \\ 0 & 0 & 0 & 0 & 0 & 0 \\ 0 & 0 & 0 & 0 & 0 & 0 \\ 0 & 0 & 0 & 0 & 0 & 0 \end{bmatrix}, B = \begin{bmatrix} 0 & 0 & 0 & 0 \\ 0 & 0 & 0 & 0 \\ 0 & 0 & 0 & 0 \\ B_1 & -B_2 & 0 & 0 \\ 0 & B_2 & -B_3 & 0 \\ 0 & 0 & B_3 & -B_4 \end{bmatrix}$$

The controllability matrix of Equation (46) given in Equation (47) is full rank, therefore the system is controllable.

$$\begin{aligned} \text{rank}(R) &= \text{rank}[B \quad AB \quad A^2B \quad A^3B \quad A^4B \quad A^5B] \\ &= \text{rank} \begin{bmatrix} 0 & 0 & 0 & 0 & B_1 & -B_2 & 0 & 0 \\ 0 & 0 & 0 & 0 & 0 & B_2 & -B_3 & 0 \\ 0 & 0 & 0 & 0 & 0 & 0 & B_3 & B_4 \\ B_1 & -B_2 & 0 & 0 & 0 & 0 & 0 & 0 \\ 0 & B_2 & -B_3 & 0 & 0 & 0 & 0 & 0 \\ 0 & 0 & B_3 & -B_4 & 0 & 0 & 0 & 0 \end{bmatrix} \mathbf{0}_{6 \times 16} = 6 \end{aligned} \quad (47)$$

The constellation deployment results of the example scenario is shown in Figure 35. The constellation deployment is achieved in approximately 220 days, which satisfies the criteria limited by the along-track deployment time requirements. Figure 35b shows that the four CubeSats were successfully deployed equally apart with a 90-degree phase angle between each other.

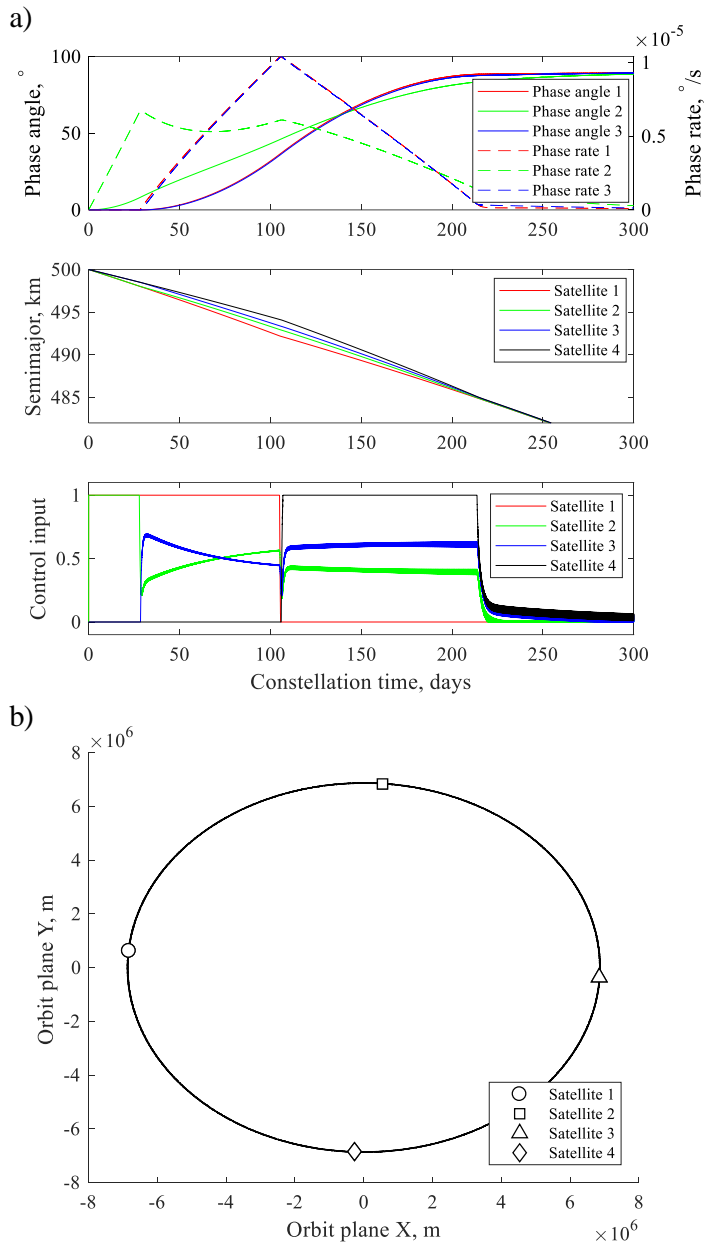


Figure 35 Plasma drag constellation example of four 1 U CubeSats at height of 500 km, magnetic moment of 6.2 Am^2 and 90 degree phase angle with $\rho_R = 9 \times 10^{-2}$. Figure 35a) shows the state, altitude, and control input from top to bottom and Figure 35b) shows the CubeSats on the orbital plane.

Chapter 6

Geomagnetic Torque Mitigation

Due to the interaction between the primary magnetic actuator and the geomagnetic field, external torque acts on the satellite, resulting change in the attitude. This chapter uses the attitude simulator in order to perform a parametric study on the performance of high-frequency polarity switching PD controller on magnetic plasma drag loss.

6.1. Transition Characteristics of Magnetic Plasma Drag due to Polarity Switching

A PIC simulation is performed in order to investigate the plasma drag force characteristics for polarity switching. Two pre-calculated spacecraft magnetic field is used for simulating the transition. Initial magnetic field surrounding the spacecraft calculated using the first magnetic moment is used for the PIC simulation, and at a known time when the PIC simulation converges, the magnetic field surrounding the spacecraft calculated using the second magnetic moment is used. Figure 36 shows the two simulated magnetic field surrounding a spacecraft, which the polarity of the magnetic torquer are opposite to each other. The magnetic torquer angle is 0 degrees and 180 degrees. In the PIC simulation, the change in magnetic field is assumed to be instantaneous.

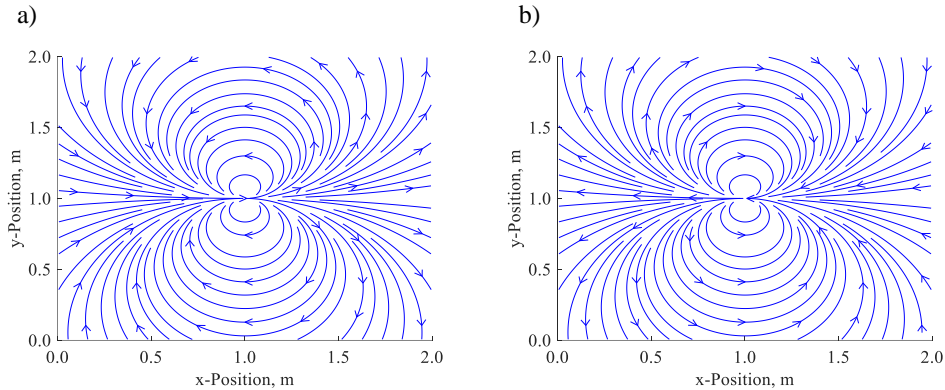


Figure 36 Two simulated magnetic field surrounding a spacecraft. Magnetic field surrounding a spacecraft when the magnetic torquer with a magnetic moment of 15 Am^2 angle is 0 degrees (left) and when the magnetic torquer with a magnetic moment of 15 Am^2 angle is 180 degrees (right).

From previous PIC simulations, the simulation case converged at 3 ms, therefore the polarity was switched at 3 ms. Figure 37 shows the magnetic plasma drag transition characteristics of a single polarity switching.

According to the simulation result, it can be seen that the charged particle motion converges to its steady state after another 3 ms, and an important characteristic is that the plasma drag force is the same even when the polarity is switched. From the plasma drag characteristics, it can be known that the polarity of the magnetic torquer can be switched in high frequency of up to 330 Hz.

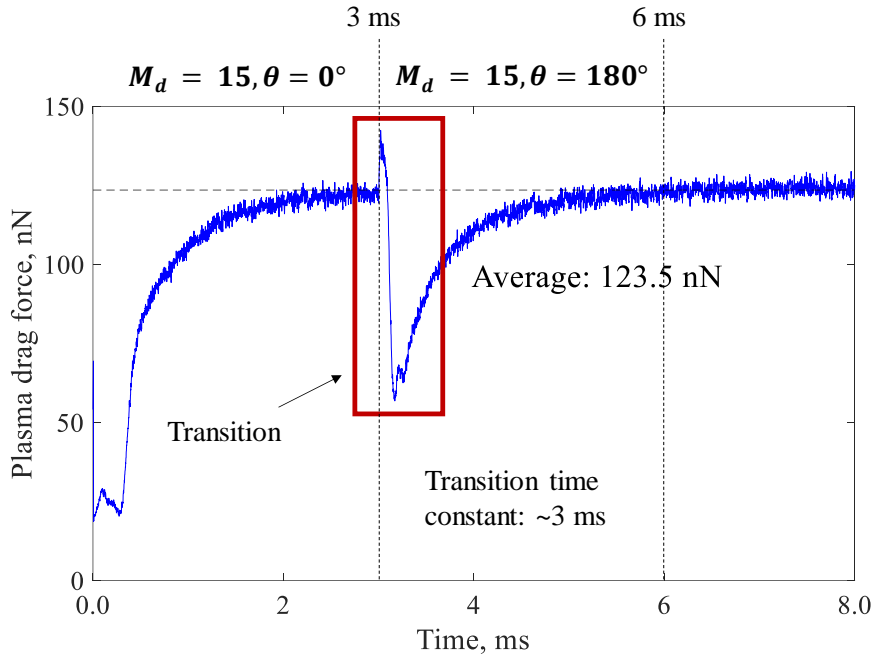


Figure 37 Plasma drag force transition characteristics of a single polarity switching. The polarity of the magnetic torquer was switched at 3 ms after the PIC simulation had converged from its initial conditions.

6.2. Effect of High-Frequency Polarity Switching

The numerical results for constant magnetic moment initially aligned with the ram vector is shown in Figure 38. The parameters used in the simulation is given in Table 15.

The angular velocity and attitude are represented against the navigation frame, which is defined by ram vector and the nadir vector. It can be seen that the accumulated disturbance torque eventually drives the satellite into an unstable state. Therefore, plasma drag constellation is not feasible when constant magnetic moment is applied to the magnetic torquer.

Table 15 Parameters used in attitude disturbance analysis due to primary magnetic torquer in plasma drag constellation

Parameter	Value
Moment of inertia, J	$\begin{bmatrix} 0.00167 & 0 & 0 \\ 0 & 0.00191 & 0 \\ 0 & 0 & 0.00191 \end{bmatrix} \text{ kg} \cdot \text{m}^2$
Initial attitude	Ram vector aligned
Orbit	575 km SSO
CubeSat platform	1 U (1 kg)
Magnetic moment	6.2 Am ²
Geomagnetic model	IGRF12 (6×6 order)
Simulation time	10 days
Integrator	Fourth order Runge-Kutta
Time step	Fixed time step (time step varies)

As a proof-of-concept of high frequency magnetic torquer switching a simulation is performed under same condition as Table 15, except the magnetic torquer is switched at 100 Hz. Consequently, the time step for the integrator is decreased to 0.01 s. As the change in magnetic characteristics of the magnetic torquer is assumed to be instantaneous, the time step is set equal to the magnetic torquer switching frequency. The simulation results of the high frequency polarity switching is shown in Figure 39.

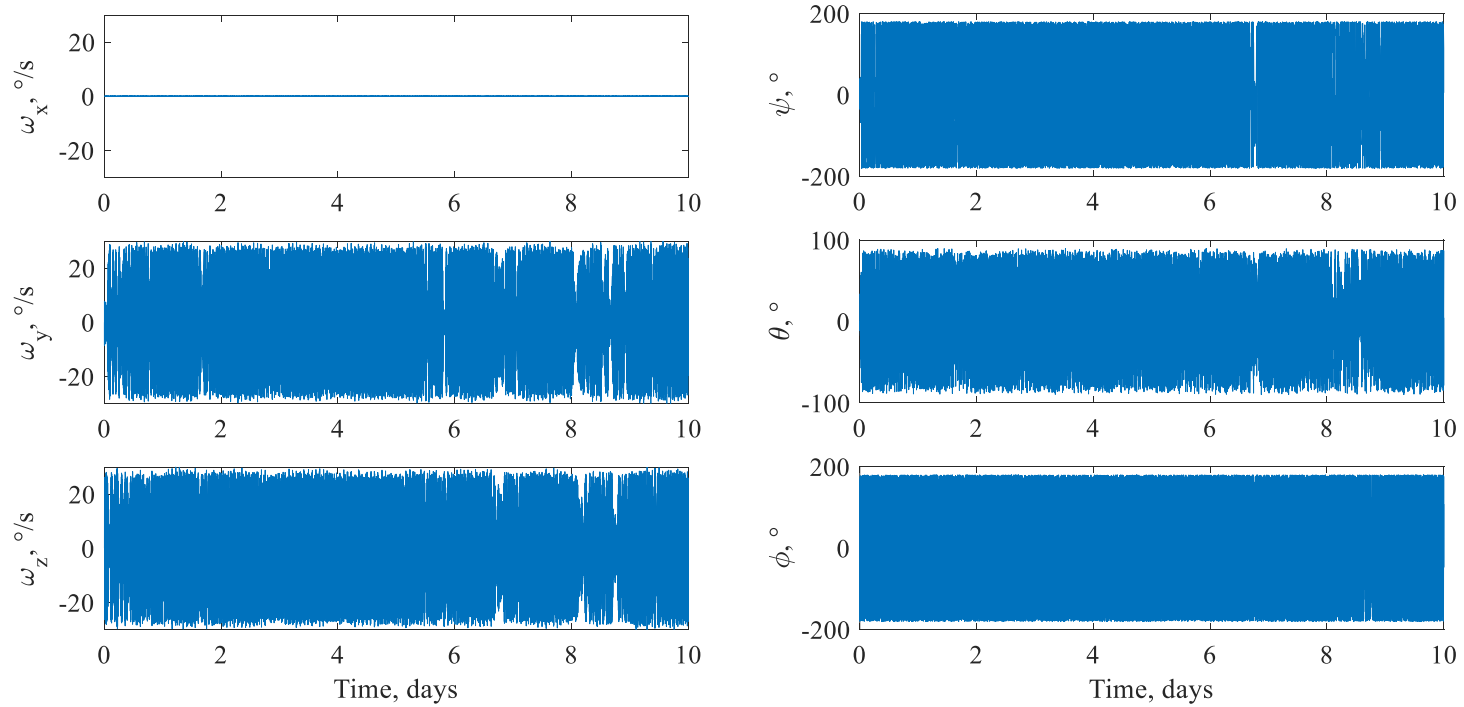


Figure 38 Angular velocity and attitude simulation results for constant magnetic moment initially aligned with the ram vector. The attitude becomes unstable due to accumulated disturbance torque.

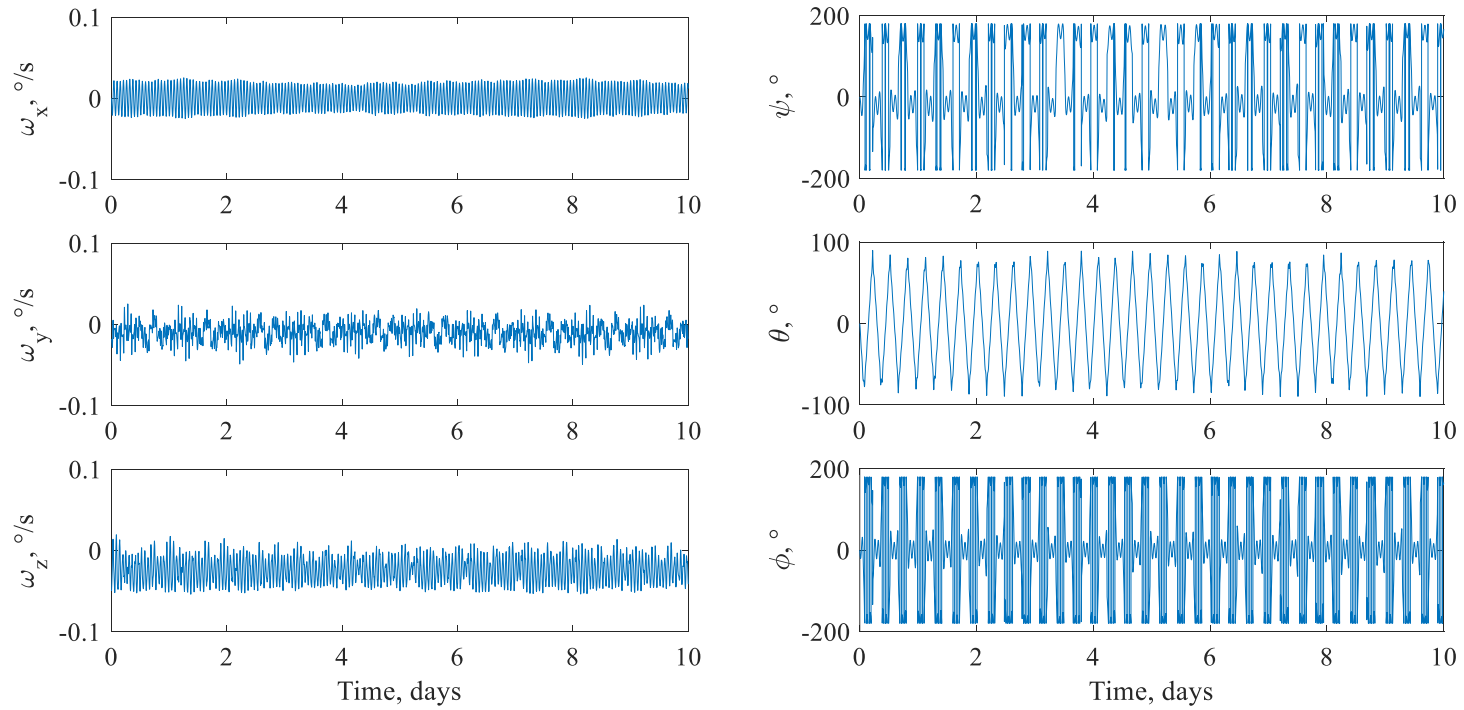


Figure 39 High frequency magnetic torquer polarity switching simulation at 100 Hz. Angular velocity decreased significantly, however the attitude is unstable due to the residual torque.

The results show that the angular velocity has decreased significantly, however the attitude remains unstable. This is due to the accumulated residual torque, which is not removed as a consequent of the $(-\vec{M}_d \times \Delta\vec{B})$ term in Equation (39).

The proposed high-frequency polarity switching PD controller is used in order to remove the residual torque. The simulation result for the hybrid switching PD controller is shown in Figure 40. It can be seen that both angular velocity and attitude are stabilized. As previously discussed in Section 3.3.2.3, performance degradation of magnetic plasma drag exists due to ram direction alignment accuracy and transition characteristics of plasma drag force during polarity switching. Figure 41 and Figure 42 shows the effect of switching frequency at 200 Hz and 50 Hz respectively. It can be seen that if the switching frequency is slow, the PD controller fails in stabilizing the attitude. On the other hand, the ram vector alignment accuracy is better when the switching frequency is 200 Hz. It can be seen that the ram direction alignment accuracy depends on the controller performance. According to the loss model in Section 3.3.2.3 the worst case of misalignment was around 8.5 degree at 100 Hz switching frequency as shown in Figure 43a corresponding to a 0.8% misalignment loss. Assuming the transition time 3 ms with linear recovery for worst case analysis in Figure 21, performance loss of 7.8 % is expected at 100 Hz switching frequency. Coupling the ram direction alignment accuracy and the polarity switching effect, 8.5 % performance loss is expected.

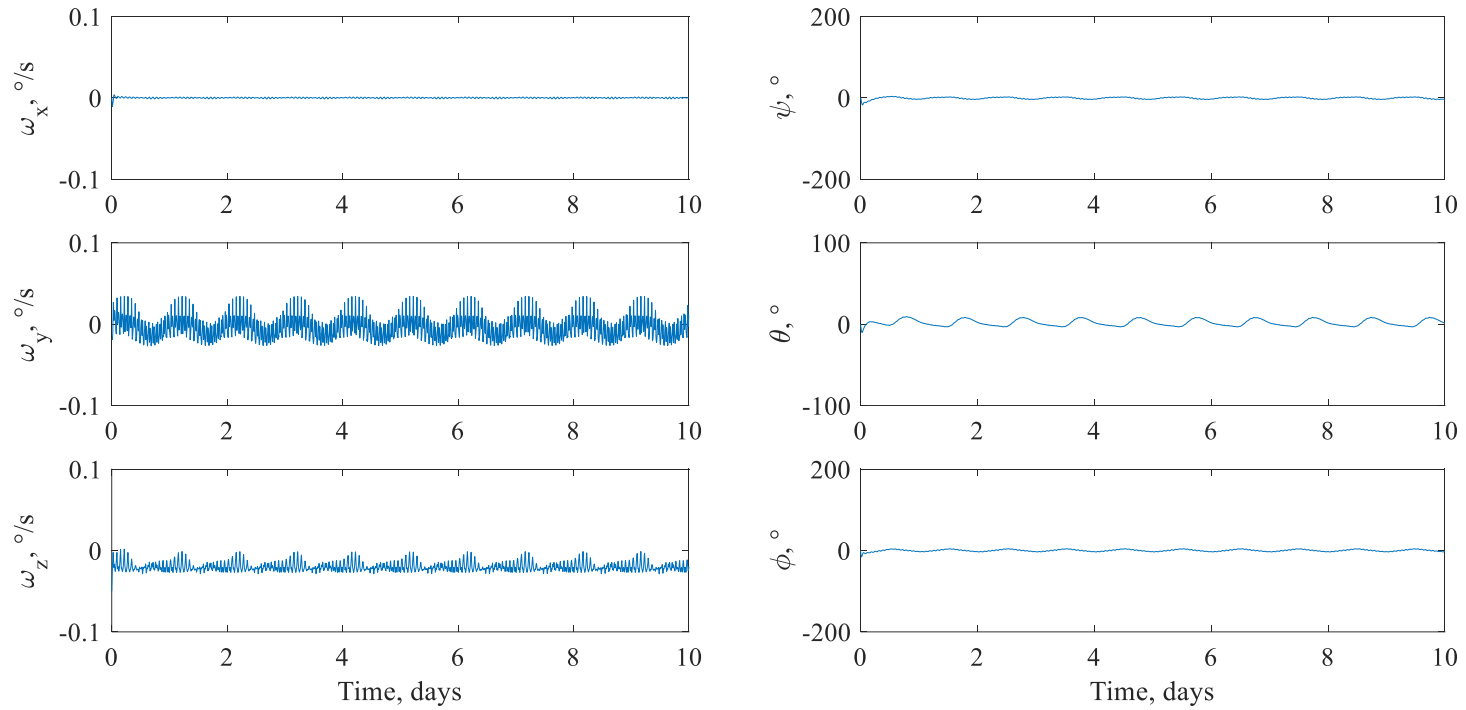


Figure 40 Hybrid switching PD controller simulation results at 100 Hz. The hybrid controller is able to stabilize both angular velocity and attitude.

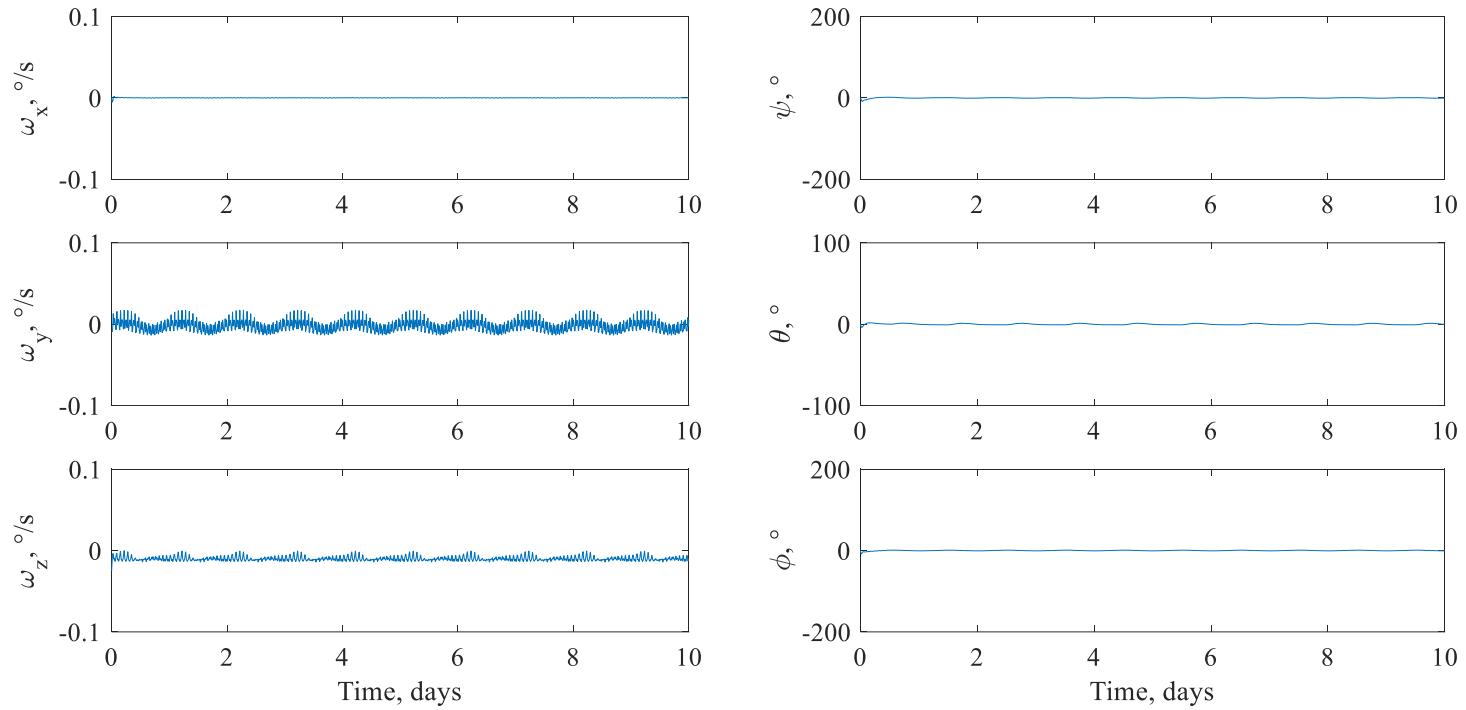


Figure 41 Hybrid switching PD controller simulation results at 200 Hz. The hybrid controller shows better attitude control performance than switching frequency at 100 Hz.

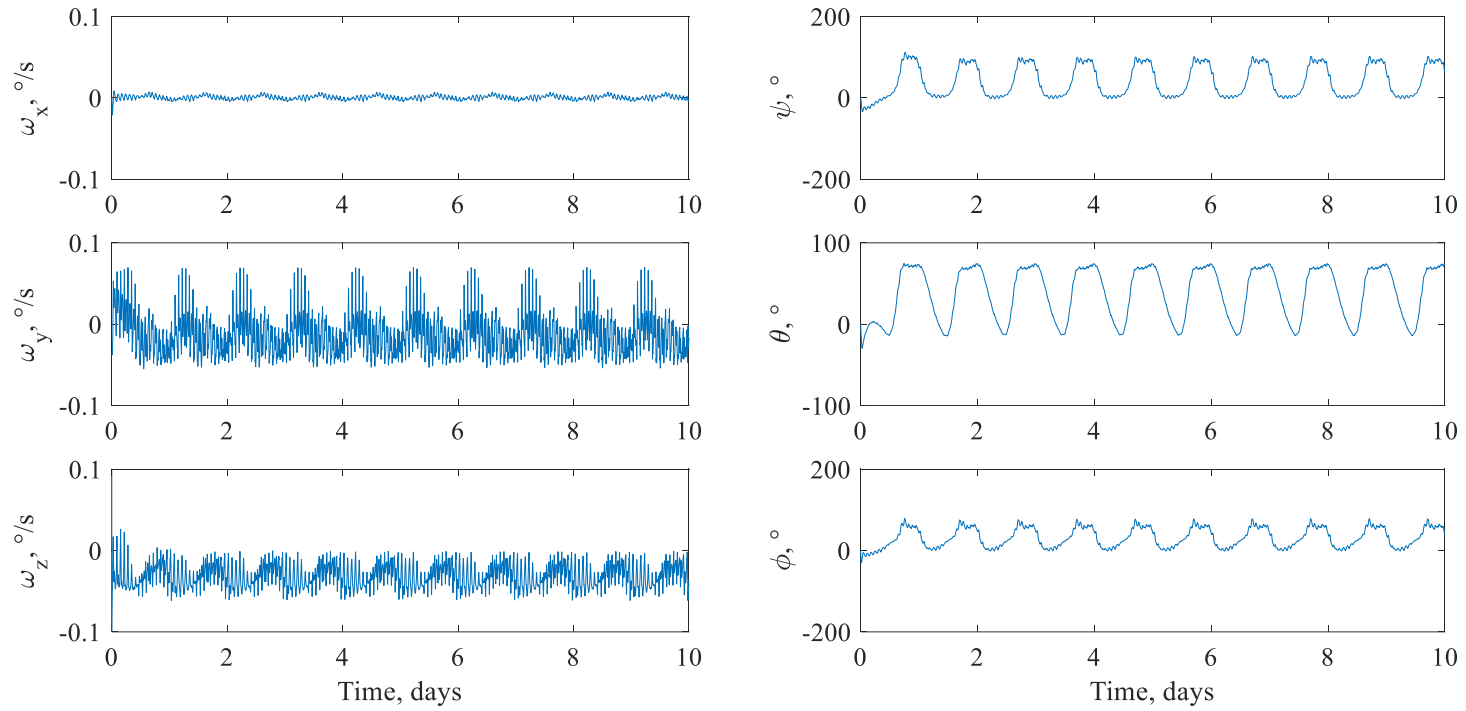


Figure 42 Hybrid switching PD controller simulation results at 50 Hz. The hybrid controller fails in stabilizing attitude due to large residual torque.

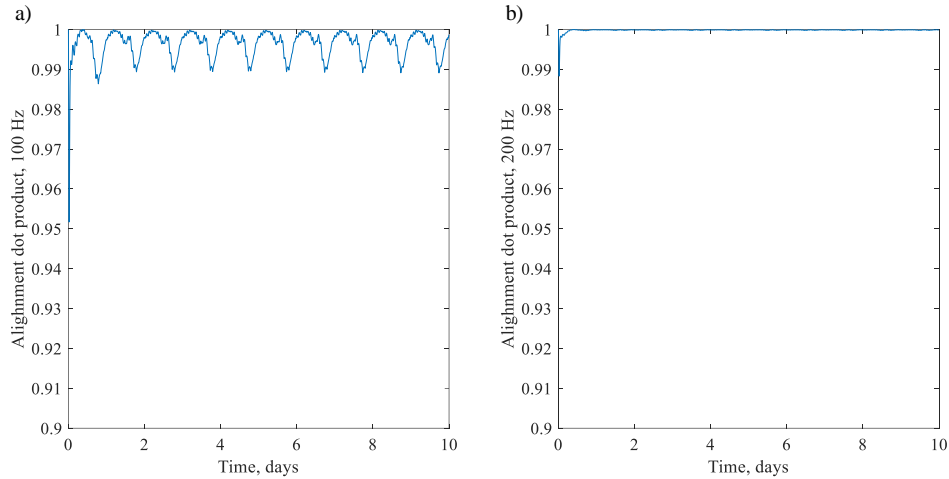


Figure 43 Dot product value of primary magnetic torquer vector and ram vector for hybrid switching PD controller.

According to Figure 43b, the misalignment of ram vector at 200 Hz switching frequency is 1.2 degree. The performance loss due to ram vector misalignment is about 0.2 %, and performance loss due to the transition characteristics is 15.4 %. Coupling the ram vector misalignment and transition characteristics give over a 15.6 % performance loss. Comparing the performance loss with 100 Hz switching frequency, it can be seen that the switching characteristics has the most significant effect on performance loss in case of the hybrid PD controller. Therefore, in case of the hybrid PD controller, plasma drag constellation performance loss can be minimized by finding the optimal switching frequency.

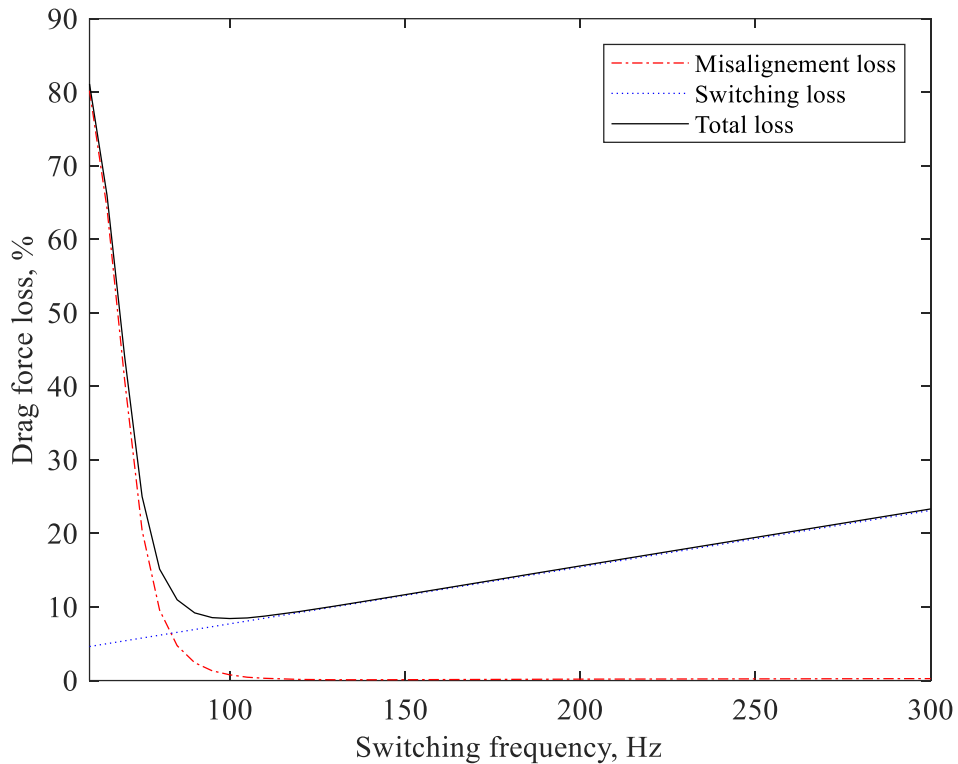


Figure 44 Evaluation of the loss function at different switching frequencies. An optimal switching frequency considering the overall loss can be seen at 100 Hz.

Attitude simulation on high-frequency polarity switching controller was performed on switching frequencies ranging from 60 Hz to 300 Hz, as shown in Figure 44. According to the results, it can be seen that an optimal switching frequency exists near 100 Hz. However, an overall loss of about 8% exist, which is dominated by the switching loss. The overall loss can be minimized by designing an optimal controller by minimizing the switching while regulating residual torque.

6.3. Practical Consideration on High-Frequency Switching

This chapter considered high-frequency polarity switching as the geomagnetic torque cancellation solution. However, Figure 37 shows that high-frequency polarity switching will generate a periodic acceleration profile. If the acceleration period matches with the resonance frequency of the CubeSat, high-frequency polarity switching could result structural failure. Figure 45 shows an example of modal survey result of a 2U CubeSat SNUSAT-1/1b.

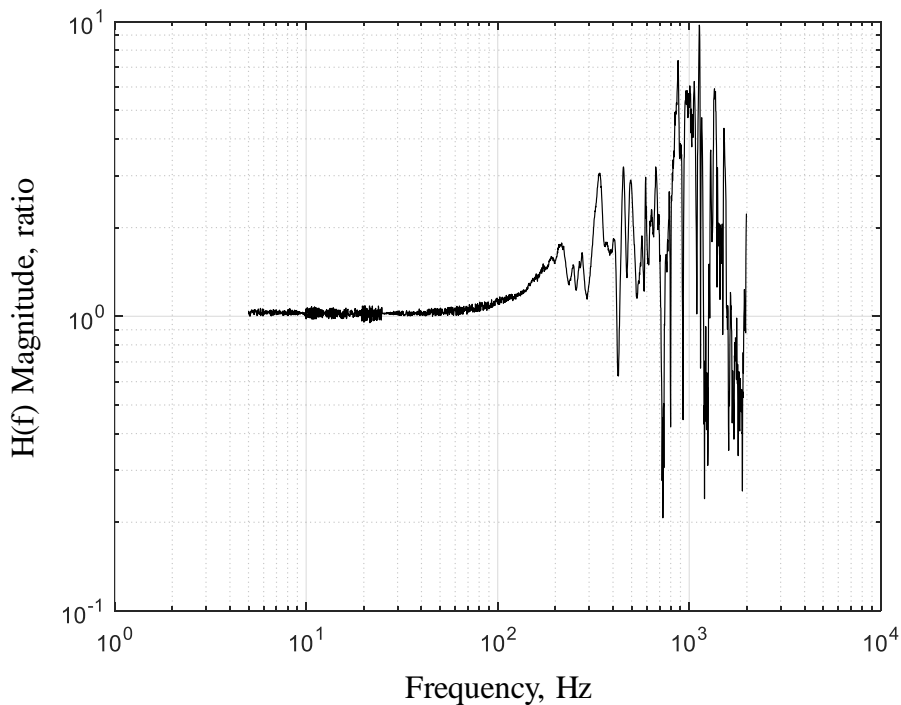


Figure 45 Modal survey result of a 2U CubeSat, SNUSAT-1/1b. Peaks at high frequency region can be spotted.

Although peaks in high-frequency region can be seen, it does not overlap with the optimal switching frequency from the previous section. However, if a CubeSat boards deployable parts such as booms with lower natural frequencies, resonance could become a problem. Therefore, high-frequency polarity switching PD controller must carefully be designed considering other aspects such as resonance.

Chapter 7

Conclusions

In the thesis, a novel CubeSat constellation deployment method is using the interaction between magnetic actuator and space environment. Spacecraft attitude is controlled using the torque generated due to the interaction between magnetic actuator and the geomagnetic field, whereas the orbit is controlled using the force generated due to the interaction between the magnetic actuator and the space plasma. Elementary analysis was performed as proof-of-concept, while numerical simulations were performed for concept validation and as part of a parametric study. System feasibility was investigated on CubeSat system regarding mass, power, and mission lifetime. Practical aspects of attitude disturbance due to large magnetic moment of the primary magnetic torquer was considered. A high-frequency polarity switching PD controller is proposed as attitude disturbance mitigation.

4.1. Summary

The main contributions and results of the dissertation is as follows:

- A novel propellant-less CubeSat constellation deployment method using plasma drag is proposed. Due to the fact that the proposed constellation deployment method uses onboard magnetic torquers, no additional actuators are required. Plasma drag constellation covers the disadvantages of conventional constellation deployment methods. The superior characteristics of plasma drag constellation deployment over other methods include no additional actuator

requirement, no deployment requirement, no propellant requirement, and the drag force can be controlled without attitude maneuver requirements.

- Elementary analysis on plasma drag constellation deployment was derived from orbital parameter investigation. Results from elementary analysis revealed the plasma drag constellation deployment property. The deployment time using plasma drag constellation was found to be proportional to square root of desired phase angle, proportional to square root of mass, and inversely proportional to square root of magnetic moment.
- Numerical simulations on plasma drag constellation deployment is performed in order to carry out parametric study. Effect of magnetic moment of magnetic torquer, desired phase angle, satellite mass, and orbit altitude on deployment time is investigated. A linear quadratic regulator (LQR) with weighing matrices for critically damped case is used in order to compare the numerical simulation results with elementary analysis results. The numerical simulation results and elementary analysis results show same trends. Furthermore, it was able to characterize an approximate linear relationship between orbit altitude and deployment time in low Earth orbit between 500 km and 1000 km.
- Feasibility analysis on CubeSat system using plasma drag constellation was performed. Upper and lower bound limitations on plasma drag constellation parameter were derived based on CubeSat resource allocation and mission lifetime. A specific example of mission lifetime due to variation in RAAN due to perturbation was examined. An example scenario with four CubeSats in a constellation using plasma drag was simulated. The simulation results showed successful deployment within the success criteria.
- Practical problem concerning attitude disturbance due to interaction between magnetic field surrounding the spacecraft and the geomagnetic field is

considered. Due to the large magnetic moment of the magnetic torquer, relatively large torque is produced when the magnetic torquer vector and geomagnetic field vector is misaligned. Combined attitude numerical simulations showed the accumulated disturbance torque drives the satellite attitude to be unstable. As a mitigation, high frequency magnetic torquer polarity switching is proposed to cancel out the magnetic disturbance torque. Numerical simulation results of high frequency polarity switching showed significant improvement in angular velocity stabilization, failed in stabilizing attitude due to accumulated residual torque. Finally, a hybrid switching PD controller is proposed in order to stabilize angular velocity using high frequency switching while the PD controller regulates the residual torque.

Table 16 Recommended TRL definitions by NASA TRA Study Team (Hirshorn and Jefferies, 2016).

TRL	Definition	Description	Exit Criteria
1	Basic principles observed and reported.	Scientific knowledge generated underpinning hardware technology concepts/applications.	Peer reviewed documentation of research underlying the proposed concept/application
2	Technology Concept and/or application formulated.	Invention begins, practical applications are identified, but are speculative. Neither an experimental proof nor detailed analysis is available to support the conjecture.	Documented description of the application/concept that addresses feasibility and benefit.
3	Analytical and experimental proof-of-concept of critical function and/or characteristic.	Research and development is initiated, including analytical and laboratory studies to validate predictions regarding the technology.	Documented analytical/ experimental results validating predictions of key parameters.
4	Component and/or breadboard validation in laboratory environment.	A low-fidelity system/component breadboard is built and operated to demonstrate basic functionality in a laboratory environment.	Documented test performance demonstrating agreement with analytical predictions. Documented definition of potential relevant environment.
5	Component and/or brassboard validation in relevant environment.	A medium-fidelity component brassboard, with realistic support elements, is build and operated for validation in a relevant environment so as to demonstrate overall performance in critical areas.	Documented test performance demonstrating agreement with analytical predictions. Documented definition of scaling requirements. Performance predictions are made for subsequent development phases.

6	System/subsystem model or prototype demonstration in a relevant environment.	A high-fidelity prototype of the system/subsystem that adequately addresses all critical scaling issues is built and tested in a relevant environment to demonstrate operational performance under critical environment conditions.	Documented test performance demonstrating agreement with analytical predictions.
7	System prototype demonstration in an operational environment.	A high-fidelity prototype or engineering unit that adequately addresses all critical scaling issues is build and functions in the actual operational environment and platform (ground, airborne, or space).	Documented test performance demonstrating agreement with analytical predictions.
8	Actual system completed and “flight qualified” through test and demonstration.	The final product in its final configuration is successfully demonstrated through test and analysis for its intended operational environment and platform (ground, airborne, or space). If necessary, life testing has been completed.	Documented test performance verifying analytical predictions.
9	Actual system flight proven through successful mission operations.	The final product is successfully operated in an actual mission.	Documented mission operational results.

4.2. Future work

Throughout the study, a novel propellant-less CubeSat constellation deployment method has been proposed and the analysis results showed that the proposed method is feasible. The current status of maturity of the proposed research can be considered to be at a technology readiness level (TRL) of 2 (Hirshorn and Jefferies, 2016). The definition of TRL recommended by the NASA TRA Study Team is provided in Table 16. This section discusses on the future work in order to advance to higher TRL levels.

4.2.1. In-depth study of disturbance torque cancellation

Disturbance torque mitigation was proposed in Section 3.2, using hybrid switching PD controller. Disturbance torque from the primary magnetic torquer was minimized by high frequency magnetic torquer polarity switching and the momentum accumulated by the residual torque was dumped by a PD controller using secondary magnetic torquers.

In the numerical simulations, external disturbance torque due to gravity gradient, solar radiation pressure, or aerodynamic drag was not considered, therefore additional investigation must be performed in order to verify the feasibility of disturbance torque cancellation.

Furthermore, polarity switching characteristics of the magnetic torquer is not taken into account, which may affect the physics. Numerical and/or experimental study on the magnetic field surrounding a satellite effected by polarity switching must be conducted in order to further verify the feasibility of disturbance torque cancellation using high frequency polarity switching.

In the hybrid switching PD controller, the polarity is switched at a constant frequency without considering the residual torque due to switching. As the geomagnetic field model is predictive, switching can be optimized to minimize the switching effort, which will result minimal magnetic moment loss during polarity transition. An optimal control method must be further studied in order to minimize performance degradation from attitude disturbance mitigation.

4.2.2. Advanced simple-IRI model development

In the presented study, a simplified IRI model is used, due to heavy computation when using the IRI2012 model. However, in order to be able to use plasma drag constellation in space, the plasma number density model must use an adequate model that well represents the actual environment.

4.2.3. Large MTQ interface development

Conventional CubeSat magnetic torquers typically are designed to a magnetic moment of 0.2 Am^2 . In the presented study, larger magnetic torquers with an order larger magnetic moment is used. As large magnetic torquers require large mass and volume, study on methods utilizing CubeSat structure as core of magnetic torquer must be carried out. Adding a metallic core to a magnetic torquer will increase the magnetic moment of the magnetic torquer, which also saves mass and volume. As CubeSats are typically made in a skeletal frame, clustering multiple skeletal frame as a large magnetic torquer must be further investigated.

Appendix

Analytical solution of magnetic plasma drag

According to Equation (6), ion density number at each epoch is required in evaluating the magnetic plasma drag force. However, using the IRI model introduced in Section 2.1.2 requires heavy computation while the simplified IRI model requires phase matching. In order to avoid these issues, an analytical solution is used in order to evaluate the magnetic plasma drag force (Matsuzawa, 2017). This section provides necessary information of derivation of the analytical solution for the change in semi-major axis.

The analytical solution is derived by integrating the change rate of the semi-major axis with respect to true anomaly of an orbit, given in Equation (A1).

$$\frac{da}{dv} = -\frac{F}{m} \frac{2a^3(1-e^2)\sqrt{1+2e\cos v+e^2}}{\mu(1+e\cos v)^2} \quad (\text{A1})$$

Then using Equation (1) and (6) in evaluating F , the change of semi-major axis about an orbit can be acquired by integrating true anomaly over one revolution as Equation (A2). The values of A_0 and G_0 can be obtained using Table 4 and the reference values given in Section 2.1.2.

$$\Delta a_{\text{plasma}} = -2ka^2 \int_0^{2\pi} \frac{(1+2e\cos v+e^2)^{\frac{3}{2}}}{(1+e\cos v)^2} \exp\left\{A_0 \cos(v+\omega) - \frac{a(1-e^2)}{G_0(1+e\cos v)}\right\} dv \quad (\text{A2})$$

where k is given in Equation (A3).

Appendix: Analytical solution of magnetic plasma drag

$$k = \frac{M_d F_s}{m M_{ds} \rho_s V_s^2} \rho_0 \exp\left(\frac{r_0}{G_0}\right) \quad (\text{A3})$$

Assuming small eccentricity ($e < 0.02$) such that the e^2 terms can be neglected, the Maclaurin series is used in order to simplify Equation (A2) as Equation (A4).

$$\Delta a_{\text{plasma}} = -2ka^2 \int_0^{2\pi} \left(1 + e \cos \nu\right) \exp\left\{A_0 \cos(\nu + \omega) - \frac{a}{G_0} (1 - e \cos \nu)\right\} d\nu \quad (\text{A4})$$

Rearranging the exponent term of Equation (A4) for $\cos \nu$ and rewriting the function in the form of the sum of two harmonic functions, Equation (A4) can be written as Equation (A5).

$$\Delta a_{\text{plasma}} = -2ka^2 \exp\left(-\frac{a}{G_0}\right) \int_0^{2\pi} (1 + e \cos \nu) \exp\{\gamma \cos(\nu - \phi)\} d\nu \quad (\text{A5})$$

where γ , $\sin \phi$, and $\cos \phi$ used in the sum of harmonic functions of Equation (A5) are given in Equation (A6).

$$\begin{aligned} \gamma &= \sqrt{A_0^2 \sin^2 \omega + \left(A_0 \cos \omega + \frac{ae}{G_0}\right)^2} \\ \cos \phi &= \frac{A_0 \cos \omega + \frac{ae}{G_0}}{\gamma} \\ \sin \phi &= -\frac{A_0 \sin \omega}{\gamma} \end{aligned} \quad (\text{A6})$$

Appendix: Analytical solution of magnetic plasma drag

For a circular orbit, e and ϕ terms in Equation (A6) are neglected, and the equation can be further simplified by using the modified Bessel function of the first kind of n as shown in Equation (A7).

$$I_n(x) = \frac{1}{2\pi} \int_0^{2\pi} \exp(x \cos \theta) \cos(n\theta) d\theta \quad (\text{A7})$$

Then, the simplified analytical solution of change in semi-major axis due to magnetic plasma drag around a revolution of circular orbit is given as Equation (A8).

$$\Delta a_{\text{plasma}} = -4\pi k a^2 \exp\left(-\frac{a}{G_0}\right) I_0(A_0) \quad (\text{A8})$$

Bibliography

- [1] Andrews, D., and Zubrin, M., 1990. Magnetic Sails and Interstellar Travel. *Journal of The British Interplanetary Society* 43, 265 – 272.
- [2] Asakawa, J., Koizumi, H., Nishi, K., et al., 2017. Development of the Water Resistojet Propulsion System for Deep Space Exploration by the CubeSat: EQUULEUS. In: 31st Annual AIAA/USU Conference on Small Satellites, SSC17-VII-04.
- [3] Ashida, Y., Yamakawa, H., Funaki, I., Usui, H., Kajimura, Y., Kojima, H., 2014. Thrust evaluation of small-scale magnetic sail spacecraft by three-dimensional particle-in-cell simulation. *Journal of Propulsion and Power* 30 (1), 186 – 196. <https://doi.org/10.2514/1.B35026>
- [4] Bae, J., Kim, Y., 2013. Revisiting the general periodic relative motion in elliptic reference orbits. *Acta Astronautica* 85, 100 – 112. <https://doi.org/10.1016/j.actaastro.2012.12.016>
- [5] Bandyopadhyay, S., Foust, R., Subramanian, G. P., Chung, S.-J., and Hadaegh, F. Y., 2016. Review of Formation Flying and Constellation Missions Using Nanosatellites. *Journal of Spacecraft and Rockets* 53 (3), 567 – 578.
- [6] Bate, R., Mueller, D., White, J., 1971. Perturbations. In: *Fundamentals of Astrodynamics*. Dover Publications, New York, NY, 398 – 399.
- [7] Barth, J. L., 2004. Space and Atmospheric Environments: from Low Earth Orbits to Deep Space. In: Kleiman J.I., Iskanderova Z. (eds) *Protection of Materials and Structures from Space Environment*. *Space Technology Proceedings* 5, Springer, Dordrecht.

- [8] Belehaki, A., Stanislawska, I., and Lilensten, J., 2009. An Overview of Ionosphere – Thermosphere Models Available for Space Weather Purposes. *Space Science Reviews* 147 (3 – 4), 271 – 313. <https://doi.org/10.1007/s11214-009-9510-0>
- [9] Bevilacqua, R., and Romano, R., 2008. Rendezvous Maneuvers of Multiple Spacecraft using Differential Drag Under J2 Perturbation. *Journal of Guidance, Control, and Dynamics* 31 (6), 1595 – 1607.
- [10] Bock, D., and Tajmar, M., 2018. Highly miniaturized FEEP propulsion system (NanoFEEP) for attitude and orbit controls of CubeSats. *Acta Astronautica* 144, 422 – 428.
- [11] Bouwmeester, J., Brouwer, G. F., Gill, E., et al., 2010. Design status of DELFINEXT nanosatellite project. In: *International Astronautical Congress, IAC-10-B4.6B.3*.
- [12] Bidy, C., Svitek, T., 2012. LightSail-1 solar sail design and qualification. In: *Proceedings of the 41st Aerospace Mechanisms Symposium*, pp. 451 – 463.
- [13] Boshuizen, C.R., Mason, J., Klupar, P., Spanhake, S., 2014. Results from the planet labs flock constellation. In: *28th Annual AIAA/USU Conference on Small Satellites, SSC14-I-1*.
- [14] Bilitza, D., Altadill, D., Zhang, Y., Mertens, C., Truhlik, V., Richards, P., Reinisch, B., 2014. The international reference ionosphere 2012 – a model of international collaboration. *Journal of Space Weather and Space Climate* 4, A07. <https://doi.org/10.1051/swsc/2014004>
- [15] Capó-Lugo, P.A., Bainum, P.M., 2009. Digital LQR control scheme to maintain the separation distance of the NASA benchmark tetrahedron constellation. *Acta Astronautica* 65 (7–8), 1058–1067. <https://doi.org/10.1016/j.actaastro.2009.03.040>

- [16] Corbin, B. A., 2015. The Value Proposition of Distributed Satellite Systems for Space Science Missions (Doctoral dissertation). Retrieved from DSpace@MIT (<https://dspace.mit.edu/handle/1721.1/103442>).
- [17] Envall, J., Janhunen, P., Toivanen, P., Pajusalu, M., Ilbis, E., Kalde, J., Koivisto, H., 2014. E-sail test payload of the ESTCube-1 nanosatellite. *Proc. Est. Acad. Sci.* 63 (2S), 210. <https://doi.org/10.3176/proc.2014.2S.02>
- [18] Mehrjardi, M. F., and Mirshams, M., 2010. Design and Manufacturing of a Research Magnetic Torquer Rod. *Proc. SPIE 7522, Fourth International Conference on Experimental Mechanics, 75221W*. <https://doi.org/10.1117/12.851652>
- [19] Felicetti, L., Palmerini, G.B., 2016. Analytical and numerical investigations on spacecraft formation control by using electrostatic forces. *Acta Astronautica* 123, 455 – 469. <https://doi.org/10.1016/j.actaastro.2015.12.056>
- [20] Flechtner, F., Morton P., Watkins M., and Webb F., 2014. Status of the GRACE Follow-on Mission. In: Marti U. (eds) *Gravity, Geoid and Height Systems*. International Association of Geodesy Symposia 141, Springer, Cham, 117 – 121.
- [21] Foster, C., Hallam, H., Mason, J., 2016. Orbit determination and differential-drag control of Planet Labs cubesat constellations. *Adv. Astronaut. Sci.* 156, 645–657.
- [22] Funaki, I., Kojima, H., Yamakawa, H., Nakayama, Y., and Shimizu, Y., 2007a. Laboratory Experiment of Plasma Flow Around Magnetic Sail. *Astrophys. Space Sci.* 307, 63 – 68. <https://doi.org/10.1007/s10509-006-9251-4>

- [23] Funaki, I., Kimura, T., Ueno, K., Ayabe, T., Horisawa, H., Yamakawa, H., Kajimura, Y., and Nakashima, H., 2007b. Laboratory Experiment of Magnetoplasma Sail, Part 2: Magnetic Field Inflation. In: The 30th International Electric Propulsion Conference, IEPC-2007-94, Florence, Italy.
- [24] Foster, C., Hallam, H., Mason, J., 2016. Orbit determination and differential-drag control of Planet Labs cubesat constellations. *Adv. Astronaut. Sci.* 156, 645–657.
- [25] Guglielmo, D., and Bevilacqua, R., 2014. Propellant-less Atmospheric Differential Drag LEO Spacecraft (PADDLES) Mission. In: 27th Annual AIAA/USU Conference on Small Satellites.
- [26] Gill, E., Sundaramoorthy, P., Bouwmeester, J., Zandbergen, B., Reinhard, R., 2013. Formation flying within a constellation of nano-satellites: the QB50 mission. *Acta Astronautica* 82 (1), 110 – 117. <https://doi.org/10.1016/j.actaastro.2012.04.029>
- [27] Heidt, H., Puig-Suari, J., Moore, A. S., et al., 2000. CubeSat: A new Generation of Picosatellite for Education and Industry Low-Cost Space Experimentation. In: 14th Annual AIAA/USU Conference on Small Satellites, SSC00-V-5, Logan, Utah, USA.
- [28] Hirshorn, S., Jefferies, S., 2016. Final Report of the NASA Technology Readiness Assessment (TRA) Study Team. HQ-E-DAA-TN43005, National Aeronautics and Space Administration.

- [29] Inamori, T., Kawashima, R., Saisutjarit, P., Sako, N., Ohsaki, H., 2015a. Magnetic plasma deorbit system for nano- and micro-satellites using magnetic torquer interference with space plasma in low Earth orbit. *Acta Astronautica* 112, 192 – 199. <https://doi.org/10.1016/j.actaastro.2015.02.025>
- [30] Inamori, T., Kawashima, R., Sako, N., Saisutjarit, P., Funase, R., Nakasuka, S., 2015b. Magnetic plasma de-orbit system for nano- and micro-satellites using a large magnetic torquer. In: *Joint Conference: 30th ISTS, 34th IEPC & 6th NSAT, 2015-d-63*.
- [31] Kawashima, R., Inamori, T., Matsuguma, T., 2015. Particle simulation of interactions between plasma and magnetic field surrounding nanosatellite magnetic torquers. In: *Joint Conference: 30th ISTS, 34th IEPC & 6th NSAT, 2015-f-87p*.
- [32] Kawashima, R., Bak, J., Matsuzawa, S., and Inamori, T., 2018. Particle simulation of Plasma Drag Force Generation in the Magnetic Plasma Deorbit. *J Spacecraft Rockets*, Article in Publish.
- [33] Kılıc, C., Scholtz, T., Asma, C., 2013. Deployment Strategy Study of QB50 Network of CubeSats. In: *2013 6th International Conference on Recent Advances in Space Technologies (RAST)*. <http://doi.org/10.1109/RAST.2013.6581349>
- [34] King, L.B., Parker, G.G., Deshmukh, S., Chong, J.-H., 2003. Study of interspacecraft coulomb forces and implications for formation flying. *J. Propul. Power* 19 (3), 497 – 505. <https://doi.org/10.2514/2.6133>

- [35] Lätt, S., Slavinskis, A., Ilbis, E., Kvell, U., Voormansik, K., Kulu, E., Noorma, M., 2014. ESTCube-1 nanosatellite for electric solar wind sail in-orbit technology demonstration. *Proceedings of the Estonian Academy of Sciences* 63 (2S), 200 – 209. <https://doi.org/10.3176/proc.2014.2S.01>
- [36] Lee, S.-H., Seo, H.-H., and Rhee, S.-W., 2005. Performance Analysis of Magnetic Torquer for Spacecraft Control. In: *International Conference on Control, Automation and Systems*, Gyeonggi-Do, Korea.
- [37] Mason, C., Tilton, G., Vazirani, N., et al., 2013. Origami-based Drag Sail for CubeSat Propellant-free Maneuvering. In: *The 5th Nano-Satellite Symposium*.
- [38] Matsuzawa, S., 2017. Orbit control for nano-satellites using plasma drag force. In: *Joint Conference: 31st ISTS, 26th ISSFD & 8th NSAT, 2017-s-11-f*.
- [39] Mueller, J., Hofer, R., and Ziemer, J., 2010. Survey of Propulsion Technologies Applicable to CubeSats. In: *Joint Army-Navy-NASA-Air Force (JANNAF)*, Colorado Springs, Colorado.
- [40] Nishida, H., Ogawa, H., Funaki, I., Fujita, K., Yamakawa, H., and Inatani, Y., 2005. Verification of Momentum Transfer Process on Magnetic Sail Using MHD Model. In: *41st AIAA/ASME/SAE/ASEE Joint Propulsion Conference & Exhibit*, AIAA 2005-4463, Tuscan, Arizona.
- [41] Nishida, H., Ogawa, H., Funaki, I., Fujita, K., Yamakawa, H., & Nakayama, Y. (2006). Two-dimensional magnetohydrodynamic simulation of a magnetic sail. *Journal of Spacecraft and Rockets*, 43(3), 667 – 672. <https://doi.org/10.2514/1.15717>

- [42] Northway, P. E., Aubuchon, C. A., Mellema, H. P., and Winglee, R. M., 2017. Pulsed Plasma Thruster Gains in Specific Thrust for CubeSat Propulsion. In: 53rd AIAA/SAE/ASEE Joint Propulsion Conference, AIAA Propulsion and Energy Forum, AIAA 2017-5040.
- [43] Örgör, N. C., Kim, S., Ling, A. W. A., et al., 2016. Overview of Aoba VELOX-IV Missions; Pulsed Plasma Thruster Attitude and Orbit Control and Earth-rim Night Image Capture for A Future Lunar Mission. In: The Fourth UNISEC-Global Meeting, NSS-07-0401.
- [44] Park, J. H., Lim, J., Kang, C. W., Kim, M., et al., 2014. Technical aspects of the SNUSAT-1 operation simulator. In: 6th European CubeSat Symposium.
- [45] Park, J. H., Maskey, A., and Jeung, I.-S., 2015. Early Point-Of-Interest Scanning mission. In: 8th Pico and Nano Satellite Workshop, Wurzburg, Germany.
- [46] Park, J. H., Matsuzawa, S., Inamori, T., and Jeung, I.-S., 2018. Nanosatellite constellation deployment using on-board magnetic torquer interaction with space plasma. *Advances in Space Research* 61 (8), 2010 – 2021.
- [47] Pastorelli, M., Bevilacqua, R., and Pastorelli, S., 2015. Differential-drag-based roto-transitional control for propellant-less spacecraft. *Acta Astronautica* 114, 6 – 21.
- [48] Pisacane, V. L., 2008. Plasma Interactions. In: *The Space Environment and Its Effects on Space Systems*. American Institute of Aeronautics and Astronautics, Inc., Reston, Virginia, pp. 207-242.
- [49] Poghosyan, A., Lluch, I., Matevosyan, H., et al., 2016. Unified Classification for Distributed Satellite Systems. In: 4th International Federated and Fractionated Satellite Systems Workshop, Rome, Italy.

- [50] Poghosyan, A., and Golkar, A., 2017. CubeSat evolution: Analyzing CubeSat capabilities for conducting science missions. *Progress in Aerospace Sciences* 88, 39 – 83.
- [51] Polat, H. C., Virgili-Llop, J., Romano, M., 2016. Survey, Statistical Analysis and Classification of Launched CubeSat Missions with Emphasis on the Attitude Control Method. *Journal of Small Satellites* 5 (3), 513 – 530.
- [52] Puig-Suari, J., Turner, C., Ahlgren, W., 2001. Development of the Standard CubeSat Deployer and a CubeSat Class PicoSatellite. In: *IEEE Aerospace Conference Proceedings*, Big Sky, MT, USA, 347 – 353.
- [53] Rafalskyi, D., and Aanesland, A., 2017. A Neutralizer-Free Gridded Ion Thruster Embedded Into A 1U Cubesat Module. In: *The 35th International Electric Propulsion Conference*, IEPC-2017-94.
- [54] Schmuland, D. T., Masse, R. K., and Sota, C. G., 2011. Hydrazine Propulsion Module for CubeSats. In: *25th Annual AIAA/USU Conference on Small Satellites*, SSC11-X-4.
- [55] Stephans, G. L., Vane, D. G., Boain, R. J., et al., 2002. The Cloudsat Mission and the A-Train: A New Dimension of Space-Based Observation of Clouds and Precipitation. *Bulletin of the American Meteorological Society* 83 (12), 1771 – 1790.
- [56] Swartwout, M., 2013. The First One Hundred CubeSats: A Statistical Look. *Journal of Small Satellites* 2 (2), 213 – 233.
- [57] Swartwout, M., 2018. CubeSat Database [Online]. Available at: <https://sites.google.com/a/slu.edu/swartwout/home/cubesat-database> (Accessed: 12 May 2018).

- [58] Thébault, E., Finlay, C. C., Beggan, C. D., et al., 2015. International Geomagnetic Reference Field: the 12th generation, *Earth, Planes and Space* 67. DOI 10.1186/s40623-015-0228-90
- [59] The CubeSat Program, 2015. CubeSat Design Specification Rev. 13. [Online] California Polytechnic State University. Available at: http://www.cubesat.org/s/cds_rev13_final2.pdf (Accessed 30 May 2018).
- [60] The CubeSat Program, 2016. 6U CubeSat Design Specification PROVISIONAL. [Online] California Polytechnic State University. Available at: http://www.cubesat.org/s/6U_CDS_2016_05_19_Provisional.pdf (Accessed 24 June 2018).
- [61] Varma, S., and Kumar, K. D., 2012. Multiple Satellite Formation Flying Using Differential Aerodynamic Drag. *Journal of Spacecraft and Rockets* 49 (2), 325 – 336.
- [62] Wie, B., Weiss, H., and Arapostathis, A., 1989. Quaternion Feedback Regulator for Spacecraft Eigenaxis Rotations. *J. Guidance* 12 (3), 375 – 380.
- [63] Winglee, R. M., Slough, J., Ziemba, T., and Goodson, A., 2000. Mini-Magnetospheric Plasma Propulsion: Tapping the energy of the solar wind for spacecraft propulsion. *Journal of Geophysical Research* 105 (A9), 21,067 – 21,077.
- [64] White, J. S., Shigemoto, F. H., and Bourquin, K., 1961. Satellite Attitude Control Utilizing the Earth's Magnetic Field. NASA-TN-D-1068, Washington: National Aeronautics and Space Administration.
- [65] Zubrin, R., and Andrews, D., 1991. Magnetic Sails and Interplanetary Travel. *J. Spacecraft* 28 (2), 197 – 203.

초 록

본 논문에서 자기구동기-우주환경의 상호작용을 사용한 큐브위성 자세 및 궤도 동시 제어 기법을 서술한다. 최근 큐브위성의 군집운영이 폭발적으로 증가하고 있지만, 큐브위성에 사용할 수 있는 궤도배치 기법은 큐브위성 특성상 많은 제약에 의해 한계가 있다. 본 논문에서는 큐브위성의 궤도배치 한계를 극복하기 위해 자기구동기-우주플라즈마 상호작용을 사용한 궤도 배치 기법을 제안한다. 자기구동기-우주플라즈마의 상호작용에 의한 플라즈마 항력과 자기구동기-지구자기장의 상호작용에 의한 토크를 활용하여 단일 구동기로 자세 및 궤도를 동시에 제어 하는 점에서 기존 기법과 차별 점을 갖는다. 자기구동기-우주환경의 상호작용을 사용하는 기법은 기존 기법과 비교할 때 다음의 장점을 갖는다: (1) 추가 구동기의 불필요성; (2) 전개 불필요성; (3) 추진제의 불필요성; (4) 자세변경 불필요성; (5) 항력 프로파일의 연속성. 플라즈마 항력을 이용한 군집궤도 배치는 큐브위성의 군집운영 능력을 부여하여 큐브위성 고유의 장점을 부각시킨다.

플라즈마 항력을 이용한 군집궤도 배치 분석을 위해 1 차원 해석을 통해 궤도배치 소요시간의 일반해를 구하고, 수치해석을 통해 1 차원 해석 해의 타당성을 증명한다. 1 차원 해석 결과 및 수치해석 결과로부터 우주플라즈마 궤도배치 기법의 소요시간은 궤도 배치간격의 제곱근과

큐브위성 무게의 제공근에 비례 관계이며 자기구동기의 자기모멘트의 제공근과 반비례 관계인 것을 도출 한다. 큐브위성 플라즈마항력 궤도배치 기법의 실현성을 분석하기 위해 외력에 의한 군집궤도면 붕괴 및 큐브위성의 유효자원을 고려하여 각 변수에 대한 유효 범위를 설정한다. 설정 된 변수 유효범위 내에서 큐브위성의 플라즈마 항력을 이용한 군집궤도 배치 실현 가능성을 보인다.

플라즈마항력을 사용하기 위한 자기구동기 구동에 따른 인공위성 자세교란 문제를 발견하고 해당 문제의 해결책으로 자기구동기의 고속 극성 전환 제어기법을 제시한다. 고속 극성 전환 제어기법을 통해 자세교란을 상쇄 시킬 수 있었으며, 극성 전환 주기에 따른 플라즈마 항력의 손실을 분석한다. 비교적 저속 극성 전환은 토크 상쇄가 충분하지 않아 자세제어 성능이 낮게 나타나 플라즈마항력 손실이 발생하며, 반면 고속 극성 전환은 플라즈마항력 전이 과정에서 플라즈마항력 손실이 발생한다. 최적 극성 전환 주기를 구하기 위해 수치해석을 수행하고 이에 따라 약 100 Hz 극성 전환에서 최적점이 존재하는 것을 보인다.

.....

주요어 : 자기구동기, 우주환경, 큐브위성, 자세제어, 궤도제어, 동시제어

학 번 : 2013-30199